

**Exploring the tumour microenvironment with  
non-invasive Magnetic Resonance Imaging techniques**

by

Firas Moosvi

MSc, University of Toronto, 2012

BSc, University of British Columbia, 2009

A THESIS SUBMITTED IN PARTIAL FULFILLMENT  
OF THE REQUIREMENTS FOR THE DEGREE OF

**Doctor of Philosophy**

in

THE FACULTY OF GRADUATE AND POSTDOCTORAL  
STUDIES  
(Physics)

The University of British Columbia  
(Vancouver)

February 2020

© Firas Moosvi, 2020

The following individuals certify that they have read, and recommend to the Faculty of Graduate and Postdoctoral Studies for acceptance, the thesis entitled:

**Exploring the tumour microenvironment with non-invasive Magnetic Resonance Imaging techniques**

submitted by **Firas Moosvi** in partial fulfillment of the requirements for the degree of **Doctor of Philosophy** in **Physics**.

**Examining Committee:**

Stefan Reinsberg, Physics & Astronomy  
*Supervisor*

Piotr Kozlowski, Physics & Astronomy  
*Supervisory Committee Member*

Vesna Sossi, Physics & Astronomy  
*University Examiner*

Robert Rohling, Electrical and Computer Engineering  
*University Examiner*

**Additional Supervisory Committee Members:**

Corree Laule, Department of Pathology & Laboratory Medicine  
*Supervisory Committee Member*

Andrew Minchinton, Department of Integrative Oncology  
*Supervisory Committee Member*

# Abstract

This thesis comprises development and application of several MRI techniques to improve our understanding of tumour growth, drug distribution, and drug effect using pre-clinical tumour models in mice. In the first part of the thesis, a novel high molecular weight contrast agent, HPG-GdF is introduced. This molecule is a hyperbranched polyglycerol labeled with an MRI contrast agent (Gd-DOTA) as well as a fluorescent tag. After injecting the agent into mice within an MRI scanner, contrast-agent kinetics were quantified using a two-parameter linear model and validated with quantitative immunohistochemistry via direct fluorescence imaging of HPG-GdF.

HPG-GdF was used to assess whether vascular function plays a role in how a chemotherapy (Herceptin) distributes within a tumour. Tumour vessel permeability and fractional plasma volume were quantified using the HPG-GdF and no relationship was found between vascular function and presence of drug. HPG-GdF was then applied to show that Avastin (an antiangiogenic agent) decreased vessel permeability in tumours. Using histological methods, a dramatic reduction in hypoxia (oxygen deficiency in tissues) was observed in treated tumours. Unfortunately, existing MRI methods to evaluate oxygenation were time-intensive and lacked sensitivity. In the second part of this thesis, we introduce, develop, validate, and apply a new method to assess tumour oxygenation using MRI.

Oxygen ( $O_2$ ) is a paramagnetic molecule that shortens the longitudinal relaxation time ( $T_1$ ) of protons in MRI. This subtle effect has been widely reported in the literature but its applications in cancer have been limited. Our technique - dynamic oxygen-enhanced MRI (dOE-MRI) - uses  $T_1W$  signal intensity images acquired during a cycling gas challenge (air or oxygen) and independent component analysis

(ICA). Hypoxia staining with pimonidazole correlated strongly with dOE-MRI values in a murine tumour model (SCCVII) and only weakly in a colorectal xenograft model (HCT-116). Finally, we provide compelling evidence that treatment with Avastin improves tumour oxygenation in subcutaneous tumours. With dOE-MRI, the sensitivity and speed of existing techniques was greatly improved. Since our technique requires no injectable contrast agent, special sequences or hardware, we anticipate that this technique can be quickly translated into the clinic.

# Lay Summary

In this thesis we have described the development and application of several magnetic resonance imaging (MRI) techniques to improve our understanding of tumour in mice. In the first part of the thesis, a new analysis method was outlined to characterize tumour blood vessels with a novel bio-compatible contrast agent. In the second part of this thesis, we introduced, developed, validated, and applied a new method to assess tumour oxygenation using MRI. Our technique is a significant improvement over other available methods as it uses a statistical technique to extract very small changes in MRI signal just by inhaling 100% oxygen gas. We used this technique to show that treatment with a cancer drug that prunes malformed and abnormal blood vessels in tumour improves oxygenation levels. Since our technique requires no injectable contrast agent, special sequences or hardware, we anticipate that this technique can be quickly translated into the clinic.

# Preface

The work presented in this thesis relies on development of MRI sequences, pre-clinical animal experiments, immunohistological staining and analysis, as well as post-acquisition MRI data analyses in collaboration with multiple researchers. Since different researchers played a part in different aspects of the works, the preface is divided by chapter to ensure adequate credit is provided to the people responsible. In general, Dr. Jennifer Baker working in the lab of Dr. Andrew Minchinton at the BC Cancer Research centre provided all of the tumour xenograft bearing mice used in experiments, and contributed extensive biological expertise and knowledge to the works presented in this thesis. All animal experimental procedures in this thesis were carried out in compliance with the guidelines of the Canadian Council for Animal Care and were approved by the institutional Animal Care Committee (A17-0042, A16-0105, A13-0053).

## **Chapter 2 - MRI and histology of vascular function in xenografts using HPG-GdF**

Work presented in chapter 2 has been published in its entirety in *Contrast Media & Molecular Imaging* with the manuscript titled “Multi-modal magnetic resonance imaging and histology of vascular function in xenografts using macromolecular contrast agent hyperbranched polyglycerol (HPG-GdF)” [1]. The author of this thesis is listed as the 3<sup>rd</sup> author on this manuscript.

Drs. Baker and Reinsberg initiated a collaboration with Drs. Katayoun Saatchi and Urs Hafeli from the Faculty of Pharmaceutical Sciences. Drs. Saatchi and Hafeli had synthesized a new hyper-branched poly-glycerol molecule (HPG-GdF) that was biocompatible and could be used as a high molecular weight MRI contrast

agent. During her masters degree at UBC, Dr. Kelly McPhee began work on this project to characterize the molecule. She performed all pilot and phantom experiments to test and measure its relaxivity, as well as initial pilot testing, QA to assess the viability of the molecule as an MRI contrast agent, as well as acquisition and analysis of pilot animal data. The work described above is not a part of this thesis, but the development and validation was essential and provided a springboard for this author's work.

Following initial characterization of the molecule, in collaboration with Dr. Baker and Dr. Reinsberg, Dr. McPhee also acquired and analysed animal data from 10 mice. Raw and some processed MRI data (notably the calculated concentration-time curves) from this experiment were used in this manuscript by this author. The raw data was used to develop and present a new method to quantify HPG-GdF concentration-time curves using a two-parameter linear model. To develop this method, several follow-up experiments with a new MRI sequence and improved analysis methods was done in collaboration with Drs. Baker and Reinsberg - this data is not part of this chapter but is instead presented in Chapters 3 and 4. Dr. Reinsberg provided much guidance and support in the design of the experiment, development of the sequence, and in troubleshooting the myriad problems that arose during sequence development.

Initial draft of the manuscript was prepared primarily by Dr. Baker based on the final chapter of Dr. McPhee's MSc. thesis, with this author contributing to the new MRI methods, followed by the MRI analysis, as well as the results and discussion sections. In developing this manuscript, all analysis code was written by this author and all parameteric maps were generated using custom code written in Python. Code to read in generic MRI data was developed by Dr. Reinsberg with some assistance from Andrew Yung, a scientific engineer at the 7T MRI. All histology data presented in this paper was collected and processed by Dr. McPhee under the supervision of Dr. Baker, and all final figure preparation including manuscript submission was done by Dr. Baker. Reviewer comments were addressed collaboratively with Dr. McPhee, Dr. Baker, Dr. Reinsberg, and this author equally.

In this chapter, this author's novel contributions include:

- Development of the two-parameter model to extract aPS and fPV

- Interpreting model parameters (in collaboration with Drs. Reinsberg and Baker)
- Implementing pharmacokinetic modelling of DCE-MRI data using the Tofts, Extended Tofts, and 2 compartment exchange model in python

### **Chapter 3 - Applications of HPG-GdF: Investigating distribution of trastuzumab in the tumour microenvironment**

Work presented in chapter 3 has been published in its entirety in *Clinical & Experimental Metastasis* with the manuscript titled “Heterogeneous distribution of trastuzumab in HER2-positive xenografts and metastases: role of the tumour microenvironment” [2].

The author of this thesis is listed as the 4<sup>th</sup> author on this manuscript. As this manuscript was part of a much larger study led by Dr. Baker, only the sections that pertain to MRI data and analysis have been reproduced here. This author contributed to the experimental design of the study, collected and analyzed all MRI data presented in this study, and assisted with figure preparation. Dr. Baker wrote the first draft of this manuscript excluding the MRI methods and results, with Dr. Reinsberg and this author assisting with editing and writing of the methods, results, and discussion sections that pertained to MRI.

In this chapter, this author’s novel contributions include:

- Application of previously developed methods and models to an experiment with a biological question

### **Chapter 4 - Applications of HPG-GdF: Assessing vascular normalization using an antiangiogenic chemotherapy**

Dr. Baker had the initial idea to use HPG-GdF as a macromolecular contrast agent to assess response of anti-angiogenic agents, designed the experiments, prepared the tumours, and conducted the interventions. Dr. Baker performed all the histological analysis including sectioning, staining, imaging, and cropping of the tumours. This author contributed to the experimental design of the study, collected and analysed all MRI data presented in this study, generated all the figures, and wrote all

of the text. Dr. Baker and Dr. Reinsberg were present during the imaging data collection. Interpretation of results - particularly of histological images - was done collaboratively by this author, Dr. Reinsberg, and Dr. Baker.

In this chapter, this author's novel contributions include:

- Application of previously developed methods and models to an experiment with a biological question

### **Chapter 5 - Oxygen-enhanced MRI**

With the exception of Sections 8.3, 5.5.8, and 5.5.6 material presented in this chapter was published in the *Journal of Magnetic Resonance in Medicine* [3].

This author was the lead investigator, responsible for all major areas of MRI data collection, analysis, manuscript composition. Dr. Baker initially approached us with the biological need to assess tumour hypoxia non-invasively using MRI and completed the immunohistochemistry staining and analysis for this project. Dr. Reinsberg was the supervisory author on this project and was involved throughout the project in concept formation and manuscript composition; he also came up with the initial idea to apply un-supervised machine learning techniques to our data. Dr. Martin McKeown provided assistance in understanding the utility of ICA in the given context.

In this chapter, this author's novel contributions include:

- Development and optimization of the dOE-MRI imaging sequence
- Development of the cycling gas delivery method
- Implementation of ICA applied to 4-dimensional spatial and temporal data
- Interpretation of the dOE-MRI maps
- Development of a metric for assessing ICA-extracted components
- Comparison of dOE-MRI maps to standard correlation maps
- Development of a method to compare dOE-MRI between experiments

## **Chapter 6 - Validation of oxygen-enhanced MRI in animals**

Sections 6.3.1, 6.3.3 have also been published as part of the first OE-MRI manuscript [3].

Sections 6.1.1, 6.2.5, and 6.3.2 pertain to work that was completed after the first publication and will be combined with the work in Chapter 7 for a new manuscript.

In this chapter, this author's novel contributions include:

- modelling the oxygen response using a lognormal velocity distribution in a vasculature network
- fitting, extracting, and interpreting model parameters
- quantitatively validating the the MRI- and histo-derived oxygenation metrics
- exploring the limits of dOE-MRI applicability by deploying across multiple tumour models

## **Chapter 7 - Applications of oxygen-enhanced MRI**

This work was done in collaboration with Dr. Baker. This author responsible for all aspects of MRI data collection, analysis, interpretation, manuscript composition. Dr. Baker's initially expressed the need to assess tumour oxygenation after modulating it with an anti-angiogenic compound. Dr. Baker also processed the immunohistochemistry staining, produced the images, proposed the drug, and we collaboratively designed the experiments. Dr. Reinsberg was the supervisory author on this project and was involved throughout the project in concept formation and manuscript composition. Both Drs. Baker and Reinsberg were instrumental in editing of the manuscript and providing guidance on data presentation, visualization. A version of this chapter will be submitted as a manuscript as a stand-alone MRI intervention paper. Portions of this chapter are also being prepared as part of a larger body of work on increasing radiation sensitivity of tumours using anti-angiogenic agents with Dr. Baker as principal author.

In this chapter, this author's novel contributions include:

- applying a VEGF-inhibitor to improve tumour oxygenation and characterizing this change using dOE-MRI

- exploring the differences in oxygenation between tumours implanted subcutaneously and intramuscularly

## **Chapter 8 - Future Work**

All analysis presented in this chapter was conducted solely by this author and contributions for the data collected has already been reported in previous chapters.

In this chapter, this author's novel contributions include:

- Implementation of independent vector analysis
- Implementation of Group ICA
- Analysis of sequential air/O<sub>2</sub> switches
- Plan to incorporate T<sub>2</sub><sup>\*</sup> in a multi-gradient echo dOE-MRI sequence

# Table of Contents

<b>Abstract</b> . . . . .	<b>iii</b>
<b>Lay Summary</b> . . . . .	<b>v</b>
<b>Preface</b> . . . . .	<b>vi</b>
<b>Table of Contents</b> . . . . .	<b>xii</b>
<b>List of Tables</b> . . . . .	<b>xviii</b>
<b>List of Figures</b> . . . . .	<b>xix</b>
<b>Glossary</b> . . . . .	<b>xxxii</b>
<b>Acknowledgments</b> . . . . .	<b>xxxv</b>
<b>1 Introduction</b> . . . . .	<b>1</b>
1.1 Cancer biomarkers and targets . . . . .	1
1.2 Animal models of cancer . . . . .	4
1.3 Need for non-invasive imaging . . . . .	5
1.4 Principles of Magnetic Resonance Imaging . . . . .	6
1.4.1 MRI sequences . . . . .	9
1.4.2 Paramagnetic contrast agents . . . . .	11
1.4.3 Dynamic contrast-enhanced MRI (DCE-MRI) . . . . .	13
1.5 Thesis structure . . . . .	14

<b>2 MRI and histology of vascular function in xenografts using HPG-GdF</b>	<b>16</b>
2.1 Introduction . . . . .	16
2.2 Methods . . . . .	19
2.2.1 Mice and tumours . . . . .	19
2.2.2 Contrast agents and dosage . . . . .	20
2.2.3 MRI acquisition . . . . .	20
2.2.4 MRI data analysis . . . . .	22
2.2.5 Histology . . . . .	25
2.3 Results . . . . .	26
2.3.1 HPG-GdF accumulates in tumour tissue in the extravascular space but does not distribute far from vasculature . . . . .	26
2.3.2 Bolus arrival time (BAT) for HPG-GdF as a screen for viable tissue . . . . .	26
2.3.3 Fractional plasma volume (fPV) and apparent permeability-surface area product (aPS) as measures of vascular function	28
2.3.4 Variable vascular function in HCT116 and HT29 human colorectal xenografts . . . . .	28
2.3.5 MRI analysis of HPG-GdF in HCT116 and HT29 xenografts: BAT, fPV and aPS . . . . .	32
2.4 Discussion . . . . .	34
2.5 Conclusion . . . . .	39
<b>3 Applications of HPG-GdF: Investigating distribution of trastuzumab in the tumour microenvironment</b>	<b>40</b>
3.1 Introduction . . . . .	40
3.2 Methods . . . . .	42
3.2.1 Reagents . . . . .	42
3.2.2 Mice and tumours . . . . .	42
3.2.3 MRI . . . . .	42
3.2.4 Immunohistochemistry . . . . .	43
3.2.5 Image acquisition and analysis . . . . .	43
3.3 Results . . . . .	44

3.3.1	Measures of vascular density, architecture and function do not consistently correlate with heterogeneous patterns of trastuzumab distribution . . . . .	44
3.3.2	Dynamic vascular permeability and blood volume measurements do not consistently relate to patterns of trastuzumab distribution . . . . .	45
3.4	Discussion . . . . .	48
3.5	Conclusions . . . . .	49
<b>4</b>	<b>Applications of HPG-GdF: Assessing vascular normalization using an antiangiogenic chemotherapy . . . . .</b>	<b>51</b>
4.1	Introduction . . . . .	51
4.2	Methods . . . . .	53
4.2.1	Mice tumours, and treatment groups . . . . .	53
4.2.2	MRI . . . . .	53
4.2.3	Immunohistochemistry . . . . .	54
4.2.4	Image acquisition and analysis . . . . .	54
4.3	Results . . . . .	55
4.3.1	Treatment with B20 reduces tumour hypoxia and HPG-GdF 72 hours after treatment . . . . .	55
4.3.2	Blood vessel permeability (aPS) and HPG-GdF accumulation (fluorescence intensity) decreases in tumours treated with B20 . . . . .	56
4.3.3	HPG-GdF enhancement curves and $AUC_{60}$ are altered after treatment, but fPV does not change . . . . .	58
4.4	Discussion . . . . .	58
4.5	Conclusion . . . . .	63
<b>5</b>	<b>Oxygen-enhanced MRI . . . . .</b>	<b>65</b>
5.1	Introduction . . . . .	65
5.2	Theory . . . . .	66
5.2.1	Physiology . . . . .	66
5.2.2	Origin of the OE-MRI signal . . . . .	67

5.3	Motivation . . . . .	69
5.4	Methods . . . . .	71
5.4.1	Mice and tumours . . . . .	71
5.4.2	MRI data acquisition . . . . .	72
5.4.3	MRI data analysis . . . . .	72
5.4.4	Quality Scores . . . . .	74
5.5	Results . . . . .	75
5.5.1	ICA isolates small changes in T <sub>1</sub> W signal intensity . . . . .	75
5.5.2	Extracting periodicity of the signal intensity change using a Fourier transform based approach is less sensitive than using ICA . . . . .	75
5.5.3	dOE-MRI with ICA does not require assumption of a response function . . . . .	77
5.5.4	Variability of response in individual oxygen cycles . . . . .	78
5.5.5	Quality of extracted component . . . . .	80
5.5.6	dOE-MRI can be extended by interleaving other scans between each repetition . . . . .	80
5.5.7	Exploring other independent components extracted using ICA . . . . .	81
5.5.8	Comparing oxygen responsiveness with dOE-MRI across experiments . . . . .	82
5.6	Discussion . . . . .	85
5.7	Conclusions . . . . .	87
<b>6</b>	<b>Validation of oxygen-enhanced MRI in animals . . . . .</b>	<b>89</b>
6.1	Introduction . . . . .	89
6.1.1	Theory: Modelling oxygen response . . . . .	89
6.2	Methods . . . . .	92
6.2.1	Animals . . . . .	92
6.2.2	Immunohistochemistry . . . . .	92
6.2.3	MR Imaging . . . . .	93
6.2.4	dOE-MRI Analysis . . . . .	93
6.2.5	Model Fitting . . . . .	93

6.3	Results . . . . .	94
6.3.1	ICA enabled dOE-MRI detects variable oxygenation in a range of tumour models . . . . .	94
6.3.2	Vascular area $A$ and mean velocity $v_f$ do not vary across tumour models, but $\sigma_f$ differentiates between tumours . . . . .	95
6.3.3	dOE-MRI maps correspond to matched histology sections . . . . .	96
6.4	Discussion . . . . .	97
6.5	Conclusions . . . . .	104
<b>7</b>	<b>Applications of oxygen-enhanced MRI . . . . .</b>	<b>105</b>
7.1	Preface . . . . .	105
7.2	Introduction . . . . .	105
7.2.1	VEGF inhibition and bevacizumab . . . . .	106
7.3	Methods . . . . .	107
7.3.1	Animals . . . . .	107
7.3.2	Immunohistochemistry . . . . .	107
7.3.3	MR Imaging . . . . .	107
7.3.4	dynamic oxygen-enhanced MRI (dOE-MRI) analysis . . . . .	108
7.3.5	Experiment Summaries . . . . .	108
7.4	Results . . . . .	109
7.4.1	Subcutaneously implanted SCCVII tumours treated with B20 are more responsive to oxygen than controls . . . . .	109
7.4.2	IM tumours have a higher baseline oxygenation level than SC tumours from the same cell line . . . . .	110
7.4.3	Effects of B20 are dependent on the tumour microenvironment and baseline oxygenation . . . . .	110
7.5	Discussion . . . . .	112
7.6	Conclusions . . . . .	117
<b>8</b>	<b>Future Work . . . . .</b>	<b>119</b>
8.1	Introduction . . . . .	119
8.2	Group ICA . . . . .	119
8.3	Further investigation of the characteristic oxygen response curve . . . . .	121

8.4	dOE-MRI maps of 10 consecutive air/O <sub>2</sub> switches are stable . . . . .	122
8.5	Exploring the link between perfusion and oxygenation . . . . .	124
8.6	Expanding dOE-MRI to include T <sub>2</sub> <sup>*</sup> . . . . .	126
8.6.1	Independent vector analysis . . . . .	127
8.7	Conclusions . . . . .	128
<b>Bibliography</b>	. . . . .	<b>130</b>

# List of Tables

Table 2.1	Summary of the quantitative histological histological data for the HCT116 and HT29 tumours. . . . .	31
Table 2.2	Summary of MRI parameters derived from pharmacokinetic modelling of the Gadovist contrast agent for both the HCT116 and HT29 tumours. . . . .	32
Table 2.3	Summary of MRI parameters derived from applying a linear model to the HPG-GdF contrast kinetics for both the HCT116 and HT29 tumours. . . . .	32
Table 7.1	Summary of scan parameters for the experiments used in this study. . . . .	109

# List of Figures

Figure 1.1	Graphical illustration of the hallmarks of cancer as presented by Hanahan and Weinberg [4]. Many of the targets described are inaccessible to non-invasive imaging and in this thesis, we focus on angiogenesis as the target of our imaging methods. Figure used with permission from Elsevier Inc.	2
Figure 1.2	Schematic of the normal tissue (left) and tumour (right) vasculature network. Note the hierarchical structure of oxygenated blood (red) passing through the arteries, arterioles, and deoxygenated blood leaving via the venules, veins. In tumours, this structure is severely compromised and often, no clear flow patterns can be distinguished with many vessels ending in dead ends or looping back onto feeding vessels.	3
Figure 1.3	A) a collection of protons with magnetic moments are represented by arrows pointing in the direction of the magnetic moment, starting from a common starting point (centre). B) After switching on a main magnetic field $\vec{B}_0$ , the net magnetic moment $\vec{M}$ slightly aligns with $\vec{B}_0$ ) because a larger fraction of spins point in the direction of the main magnetic field (in the rotating frame). C) The net magnetization moment is tipped to the transverse axis with an RF pulse $\vec{B}_1$ so the signal can be measured. Annotations were added to the simulated images produced by Hanson et al.([5]), used with permission from Wiley and Sons.	8

Figure 1.4	Dependence of flip angle on the signal from an SPGR sequence for two tissues with $T_1$ of 2200 and 1760 ms respectively. The Ernst angles for each tissue is marked with dotted lines, and the flip angle that would result in the maximum contrast difference is marked with a solid black line. . . . .	11
Figure 1.5	On the left, the contrast ( $\Delta SI$ ) for two tissues with $T_1$ s of 2200ms and 2090ms for three $T_R$ s are plotted along with the Ernst angles for each $T_R$ . As the $T_R$ increases, the total available signal also increases because the magnetization has longer to recover. On the right, the curves are normalized by the $T_R$ which is more useful in optimizing sequence parameters. The three chosen repetition times (240ms in black, 120ms in red, and 60ms in grey) represent the range of $T_R$ s used in the work presented in this thesis. . . . .	12
Figure 1.6	Extended Tofts Model . . . . .	14
Figure 2.1	HPG-GdF. The 583 kDa globular Hyperbranched PolyGlycerol (HPG) molecules are derivatized with p-NH <sub>2</sub> -benzyl-DOTA (Macrocyclics) at 20 $\mu$ g Gd per mg HPG (approximately 300 chelates per molecule) and tagged with Alexa Fluor 647 dye, as previously described [6]. Figure reused with permission from Wiley and Sons. . . . .	21



Figure 2.4	Individual HT29 tumour (T01-05) slice maps are presented for parameters derived using Gadovist (BAT, AUGC <sub>60</sub> , K <sup>trans</sup> ), HPG-GdF (BAT, fPV, aPS, AUGC <sub>60</sub> ) and histological imaging of necrosis. Figure reused with permission from Wiley and Sons. . . . .	29
Figure 2.5	fPV and aPS parameter maps for an HT29 tumour (T01) are shown with corresponding histological image depicting CD31-stained vessels (blue) and HPG-GdF native fluorescence (red). The high fPV region has notably greater vascular density, and HPG-GdF is clearly seen overlapping with vessels (black) or accumulating in the extravascular space. A region with high aPS that does not correspond to high fPV is magnified (A) and compared with a high fPV region that does not correspond to high aPS (B). Figure reused with permission from Wiley and Sons. . . . .	30
Figure 2.6	HPG-GdF distribution in HCT116 and HT29 colorectal tumour xenografts at 60-min: histological analysis. (A) The whole-slice average fluorescence intensity shows that HPG-GdF accumulates to a greater degree and distributes further away from vasculature in HT29 tumours. (B) Sample images show HPG-GdF (red) overlaid on CD31 (blue); insets also display nuclear density (grey). A greater degree of HPG-GdF accumulation can easily be appreciated in the HT29 tumours. Figure reused with permission from Wiley and Sons. . . . .	33
Figure 2.7	Vascular function in HCT116 xenografts. Whole-slice maps are presented for individual HCT116 tumours (T01-T05, vertical columns) for parameters derived from MR imaging of Gadovist (BAT, AUGC <sub>60</sub> , K <sup>trans</sup> ), MR imaging of HPG-GdF (BAT, fPV, aPS, AUGC <sub>60</sub> ) and histological imaging (necrosis). Figure reused with permission from Wiley and Sons. . . . .	37

Figure 3.1	A) Magnified region of a BT474 xenograft treated with 10 mg/kg trastuzumab for 24 h. Carbocyanine fluorescent dye (cyan) around CD31 stained vessels (blue) indicates patency; non-patent vessels are indicated as red arrows. Trastuzumab extravasates from vessels heterogeneously, with many patent vessels showing no extravascular bound trastuzumab (green arrows) even when adjacent patent vessels do have perivascular trastuzumab. B) An anatomical RARE MR image with the tumour is shown alongside an AUC <sub>60</sub> map using Gadovist in MDA-MB-361 tumours. The AUC <sub>60</sub> map is compared with slice-matched histology sections of bound trastuzumab (purple), vascular architectural markers $\alpha$ SMA and CIV (both shown in red). . . . .	46
Figure 3.2	fPV and aPS parameter maps are compared to matched histology sections stained for bound trastuzumab (magenta), and for HER2 (grey), carbocyanine marker of perfusion (cyan) and for CD31 vasculature (blue). Areas of vascular function (MRI) and trastuzumab (histology) correlation are indicated (orange arrows) in both modalities; example areas of poor matching are also shown (purple arrows). Stars indicate location of fiducial markers for multi-modal slice comparison. . . . .	47
Figure 4.1	Histological sections of a control (left) and treated tumour (right) are shown to illustrate the dramatic decreases both in pimonidazole staining and in accumulation of HPG-GdF in the treatment group. . . . .	55
Figure 4.2	Median pimonidazole staining is markedly reduced for the B20-treated group ( $I_{pimo} = 17.2$ ) compared to the controls ( $I_{pimo} = 21.7$ ). Median HPG-GdF staining intensity is also reduced for the treated tumours ( $I_{hpg} = 12.7$ ) compared to the controls ( $I_{hpg} = 11.0$ ). P-values from the Mann-Whitney $U$ test were $p = 5 \times 10^{-5}$ (pimo, left) and $p = 8 \times 10^{-6}$ (HPG-GdF fluorescence, right). . . . .	56

Figure 4.3	Histological sections shown for 6 control and 6 treated tumours, with four slices per tumour. All sections are stained for pimonidazole (green) and HPG-GdF (red). . . . .	57
Figure 4.4	Summary of group differences for all three DCE-MRI parameters: $AUC_{60}$ , aPS, and fPV. There is a statistically significant reduction in $AUC_{60}$ and aPS for the treated tumours, but no difference measured for fPV. P-values from the Mann-Whitney $U$ test for the comparisons were $p = 0.03$ ( $AUC_{60}$ ), $p = 0.01$ (aPS), and $p = 0.15$ (fPV). . . . .	59
Figure 4.5	Histological stains of HPG-GdF shown alongside approximate slice matched DCE-MRI parameter map of aPS and the group-averaged contrast enhancement curves of control and treated tumours. There is an overall reduction in aPS for the treated tumours. The mean contrast enhancement curves (group means in dark blue and red lines; shaded region is the 95% confidence interval determined by bootstrapping) also show that the treated tumours have a higher enhancement slope after contrast agent injection. . . . .	60
Figure 5.1	Sigmoidal curve illustrating the relationship between the haemoglobin saturation (y-axis) and the oxygen tension (x-axis). When the oxygen tension is low, the Hb easily binds $O_2$ and there is a rapid rise in oxygen saturation (green arrow). Note that it takes a large increase in oxygen tension to bind the last $O_2$ and similarly, a large decrease in oxygen tension to release the last $O_2$ (purple arrow) [7]. . . . .	67

Figure 5.2 A schematic of the change in the partial pressures of oxygen and carbon dioxide at various points in the body. The $p_{O_2}$ of inhaled ambient air is 160 mmHg, and this is breathed in to the lungs. Oxygen diffuses out of the alveoli into the surrounding capillaries and binds to Hb due to the pressure gradient (capillary $p_{O_2}$ is 40 mmHg). This oxygenated blood ( $p_{O_2} = 100\text{mmHg}$ ) now enters the heart and is pumped through the body, with the Hb releasing oxygen through capillaries due again to the pressure gradient (tissue $p_{O_2}$ is $< 40$ mmHg) [8]. Textbook content produced by OpenStax Biology is licensed under a CC-BY 4.0 license. . . . .	68
Figure 5.3 A schematic representation of our current understanding of the origin of the OEMRI effect. In normoxic tissue, Hb is almost fully saturated and any excess breathed O <sub>2</sub> cannot bind to the Hb molecule. Consequently, O <sub>2</sub> dissolves in the blood plasma and as the excess oxygen diffuses out into the tissue, it also dissolves in the interstitial tissue fluid resulting in a net T <sub>1</sub> decrease. It is hypothesized that in the hypoxic tissue, Hb is not fully saturated with oxygen due to increased tissue demands and/or a poorly organized vascular network. The excess breathed oxygen in this case binds to the Hb molecule and does <b>not</b> dissolve in the plasma leading to no change in T <sub>1</sub> . . . . .	70
Figure 5.4 (A) T <sub>2</sub> W MRI of a tumour xenograft at 7T and (B) the corresponding T <sub>1</sub> W signal-time traces of a single voxel (solid yellow) and whole-tumour slice ROI (dotted black) during gas cycling at two-minute intervals of air (x axis; blue) and O <sub>2</sub> (x axis; yellow). (C) Plot of the four extracted ICA components from the entire tumour ROI, component $c_4$ (purple) exhibits the same temporal features as the oxygen cycling time course shown along the bottom. All components are normalized, no vertical scale is shown. Figure reused with permission from Wiley and Sons. . . . .	76

Figure 5.5	Histogram of all the normalized intensities at the frequency of interest in all the tumour voxels. The intensities were normalized to the value at the frequency of interest extracted from the ICA component (5.67), plotted on the x-axis. . . . .	77
Figure 5.6	The normalized intensities at the frequency of interest as a spatial map. Higher values in the spatial map are represented as green and low intensity values are dark. . . . .	77
Figure 5.7	(A) dOE-MRI map of an SCCVII tumour where purple voxels contribute strongly to the extracted component using ICA in the T <sub>1</sub> W signal timecourses. Green voxels in the dOE-MRI map have a strong contribution of the inverse extracted component. Pearson's r-maps are shown correlating the raw time-signal voxel by voxel with a square wave (B), and an exponential convoluted with a square wave called the hemodynamic response function (HDRF) (C). Panels B and C are correlation maps whereas A is the dOE-MRI map from ICA. Note the low correlation coefficients (on the order of 10 <sup>-3</sup> ) are characteristic of the extremely low amplitude of the oxygen cycling compared to other competing effects. Figure reused with permission from Wiley and Sons. . . . .	78
Figure 5.8	The first row shows the extracted ICA component of a whole tumour. The second row shows the magnitude of the Fourier-transformed signal plotted against frequency in Hz. The highest frequency is kept and all other values are set to 0. This filtered data is inverse Fourier transformed to produce the Fourier-filtered response curve. This response curve is plotted in the third plot. A correlation map (colour bar ranging from -0.01 to +0.01) of the Fourier-filtered response curve with the mean-normalized signal intensity is shown alongside the dOE-MRI map (colour bar ranging from -0.15 to +0.15) for comparison.	79

Figure 5.9	The dOE-MRI map including the full dataset of all three cycles (A) is compared to each of the three gas cycles separately (B,C,D), and to a map that temporally undersamples by selecting every third datapoint from the full dataset (E). Voxel-wise plots of each map are correlated to the full dataset and a linear regression with Pearson's r is shown. Figure reused with permission from Wiley and Sons. . . . .	80
Figure 5.10	All ninety-one dOE-MRI extractions shown with the quality scores (1=unusable to 5=ideal) and the number of tumours shown in parentheses. Colours represent the different scores with 1 in dark green, 2 in orange 3 in blue, 4 in purple, and 5 in lime green. . . . .	81
Figure 5.11	dOE-MRI maps and associated component traces of differently sampled data. To achieve different levels of subsampling, the raw data was spliced and then ICA was applied. The oxygenation maps look very similar between different subsample factors. Temporal resolution and number of points were 4.3 s and 200 points (subsample 1), 8.5 s and 100 points (subsample 2), 12.8 s and 67 points (subsample 3), 17.1 s and 50 points (subsample 4), 21.3 s and 40 points (subsample 5), and 25.12 s and 34 points (subsample 6). . . . .	82
Figure 5.12	Plots of the four components extracted from ICA are shown ( $(  c_i   = 1, \forall i)$ ) along with the corresponding weighting factor maps (normalized to mean voxel wise mean signal intensity). Corrupting influences such as temperature drifts are often present and produce slowly increasing or decreasing trends (for e.g., $c_1$ ) and breathing artefacts corresponding to short-lived spikes ( $c_3$ ). No explanation could be found for $c_2$ . Figure reused with permission from Wiley and Sons. . . . .	83

Figure 6.1	Schematic representation of the complex vascular network (left) with multiple velocity profiles (arrows) and its equivalent representation as a single vessel with a distribution of flow profiles (right). The distribution of velocity profiles of the representative single vessel is the lognormal distribution. Schematic representation re-created from Hudson et al. [9]. . . . .	90
Figure 6.2	Fit of equation 6.6 to an oxygen response curve with the residuals plotted along the x-axis for each point. For this fit, $A = 0.18$ , $v_f = 0.66\text{mm}/\text{s}$ , and $\sigma_f = 0.58\text{mm}/\text{s}$ . . . . .	94
Figure 6.3	Top: dOE-MRI maps for four tumour models HCT-116, BT-474, SCCVII, and SKOV3 are shown. Chosen slices are representative of the mean percent negative dOE-MRI fraction for the respective tumour model. Bottom: The box-whisker plot shows the quartiles of percent negative dOE-MRI voxels for all imaged tumours. Figure reused with permission from Wiley and Sons. . . . .	95
Figure 6.4	Top: Individual fits to the oxygen response curve for each animal and tumour type. Bottom: Box plots showing the median value and quartiles for $A$ , $v_f$ , and $\sigma_f$ across the three tumour models. . . . .	96
Figure 6.5	The proportion of negative dOE-MRI voxels is plotted against the histological hypoxic fractions with Pearson's $r = 0.76$ for SCCVII tumours ( $r = 0.14$ after excluding tumour with high hypoxic fraction) and $r = 0.037$ for HCT-116 tumours. Each point is a slice average. Figure reused with permission from Wiley and Sons. . . . .	97
Figure 6.6	SCCVII murine tumours with slice-matched histological images depicting pimonidazole-labeled hypoxia (green) and CD31-stained vasculature (purple) are shown next to the dOE-MRI parameter maps similarly colored with $O_2$ -positive (purple) and $O_2$ -negative (green) areas. Corresponding ICA extracted components are also shown. Figure reused with permission from Wiley and Sons. . . . .	98

- Figure 6.7 HCT-116 human colorectal xenografts with slice-matched histological images depicting pimonidazole-labeled hypoxia (green) and CD31-stained vasculature (purple) are shown next to the dOE-MRI parameter maps similarly colored with O<sub>2</sub>-positive (purple) and O<sub>2</sub>-negative (green) areas. Corresponding ICA extracted components are also shown. Figure reused with permission from Wiley and Sons. . . . . 99
- Figure 7.1 A) NCWF maps obtained from Independent Component Analysis (ICA) (dOE-MRI maps) are shown for control tumours as well as those treated with 5mg/kg B20 and imaged 48 hours later. Of the 10-16 slices for each animal, a representative slice was chosen. As indicated by the distribution of purple voxels, control tumours show considerably less response to oxygen than the treated tumours. Additionally, regions marked in green are considered to be hypoxic; these regions were not prevalent in the treated tumours. B) A representative histology slice from a control and a treated tumour is shown stained with pimonidazole (green) and CD31 (purple). . . . . 111
- Figure 7.2 A) Group differences of the normalized mean NCWF are shown in a boxplot. Each dot represents the mean value of a mouse with the controls in blue and treated in green. The differences are statistically significant ( $p=0.0092$ ) with a large effect size (Hedge's  $g = 1.08$ ). B) Density distributions of all voxels shows treated tumours shifting towards increased responsiveness to delivered oxygen (higher NCWF). . . . . 112
- Figure 7.3 Calculated tumour volumes from each of the four groups is shown. There were no statistically significant differences in tumour volumes amongst any of the groups. . . . . 113

Figure 7.4	<b>A)</b> Boxplot with four groups, 5mg/kg B20 treated and control mice with both SC and IM tumours. Differences between control SC and IM tumours, as well as control SC and treated SC tumours are statistically significant (Mann-Whitney U test; $p < 0.005$ , marked as **). There was no significantly difference in treated and control IM tumours. <b>B)</b> Voxel density distributions of NCWF for SC (top) and IM (bottom) treated and control tumours. Density distribution (i.e. normalized histograms) are shown rather than voxel counts due to uneven group size. Note the shift of the IM control tumours towards a higher NCWF value. . . . .	114
Figure 7.5	Representative histological sections from 16 total tumours of all four groups: 5mg/kg B20 treated and control mice with SC and IM tumours. Hypoxia marker pimonidazole staining is shown in green, and purple indicates the presence of blood vessels stained by CD31. . . . .	114
Figure 8.1	Comparison of the standard ICA technique and Group ICA. The main difference is in the pre-processing of the MRI data comprising spatial coordinates ( $x, y, z$ ) and temporal information ( $t$ ). Group ICA datasets are prepared by spatially concatenating all animals together ( $n$ ). The output of the ICA techniques also differs: in standard ICA each application produces a set of independent components whereas in Group ICA only a single set of independent components is produced. . . . .	120
Figure 8.2	Extracted oxygen enhancing component from ICA applied to the spatially concatenated cohort data. . . . .	121

Figure 8.3	Two animals were selected to explore the effect of the number of components ( $m$ ) on the dOE-MRI maps. The two animals presented here were selected to exhibit the full range of variability in extracted components. The low variability example shows no discernible difference in the extracted component anywhere from $m = 3$ to $m = 12$ . The high variability example shows considerably more noise in the extracted component, but the same overall trend. The corresponding dOE-MRI maps for both the low variability and high variability examples show almost no difference in the oxygenation maps. . . . .	122
Figure 8.4	Results of a dOE-MRI-based analysis to sequentially analyze ten consecutive air-oxygen switches (D). The averaged dOE-MRI map (A) across all 10 cycles reveals some hyperintense regions corresponding to oxygen-responsive areas. The voxel-wise standard deviation (B) and coefficient of variation (C) of the ten dOE-MRI maps shows some variability at the top of the tumour as well as on the mid-right of the tumour. . . . .	125
Figure 8.5	dOE-MRI maps and DCE-MRI AUC <sub>60</sub> maps and slice-matched histology sections of SCCVII and HCT-116 tumours. Large regions marked as purple in the dOE-MRI maps are O <sub>2</sub> -positive and also correspond to regions that have high AUC <sub>60</sub> values (yellow). Green or O <sub>2</sub> -negative regions from the dOE-MRI map are often consistent with unperfused regions in the AUC <sub>60</sub> (black), but there are regions of mismatch. Histology images stained with pimonidazole (green) and CD31 (purple) are shown for corresponding sections. . . . .	126
Figure 8.6	Schematic of the current and proposed acquisition and analysis for dOE-MRI with combined R <sub>1</sub> and R <sub>2</sub> <sup>*</sup> imaging. . . . .	128

# Glossary

**AIF** Arterial input function

**aPS** Apparent permeability surface area product

**$\alpha$ SMA** alpha smooth muscle actin - a vascular architectural marker

**AUC** Area under the Curve

**AUGC<sub>60</sub>** Area under the gadolinium-concentration curve 60 seconds after injection

**BAT** Bolus arrival time

**BBB** Blood brain barrier

**BOLD** Blood oxygen level dependent MRI

**BT474** Cell line derived from a human mammary gland (breast/duct) cancer

**CA** Contrast agent

**CD31** cluster of differentiation 31

**CIV** Collagen IV - a marker of basal lamina collagen, a vascular architectural marker

**Da** Dalton, a unit of measurement for molecular weight

**DCE-MRI** dynamic contrast-enhanced MRI

**DCE-US** dynamic contrast-enhanced ultrasound

**dOE-MRI** dynamic oxygen-enhanced MRI

**DOTA** A chemical compound - also known as tetraxetan - that serves as a chelating agent to prevent toxicity of gadolinium ions.

**EPR** Enhanced permeability and retention

**FastICA** An ICA algorithm implemented in the `scipy.sklearn v0.17.1` python package.

**FLASH** Fast low angle shot magnetic resonance imaging.

**fMRI** functional magnetic resonance imaging.

**fPV** Fractional plasma volume - a DCE-MRI parameter extracted using a high molecular weight agent

**Gd-DTPA** Gadolinium ion chelated to Diethylenetriamine Pentaacetic Acid (DTPA), an organic chelating molecule

**Hb** Haemoglobin

**HER2** Human epidermal growth factor receptor 2

**HPG-GdF** Hyperbranched polyglycerol (HPG)

**i.p.** Intraperitoneal, injections take place in the body cavity of an animal

**i.v.** Intravenous, injections are administered through a vein of an animal

**ICA** Independent Component Analysis

**IM** Intramuscular, injections are administered in the muscle of an animal

**IVA** Independent vector analysis

**K<sup>trans</sup>** Volume transfer constant

**kDa** kilo dalton, or 1000 daltons

**MAb** Monoclonal antibody

**MCA** Macromolecular contrast agents.

**MDA-MB-361** Cell line derived from a breast cancer that metastasized to the brain

**MGE** Multi gradient echo

**MW** Molecular weight

**NCWF** Normalized component weighting factor value

**OE-MRI** Oxygen-enhanced magnetic resonance imaging

**PF** Perfused fraction

**PS** Permeability surface area product

**RARE** RARE sequence is a rapid acquisition with refocused echoes. This sequence is also known known as fast spin echo (FSE) or turbo spin echo (TSE)

**ROI** Region of interest

**SC** Subcutaneous

**SNR** Signal to noise ratio

**USPIO** Ultrasmall super-paramagnetic iron oxide

**VEGF** Vascular endothelial growth factor

$v_e$  Volume of extravascular extracellular space per unit volume of tissue

$v_p$  Blood plasma volume per unit volume of tissue

# Acknowledgments

This work would not be possible without the tireless commitment and mentoring by my friend and supervisor, Dr. Stefan Reinsberg. Stefan, I could not have done this without you - you made my journey everything that it was. Dr. Baker was also instrumental in helping run, plan, and provide support for all of the work presented here - thank you Jenn! Members of my supervisory committee, Drs. Kozlowski, Laule, and Minchinton were all excellent sources of advice, feedback, guidance, and general project direction. Particular thanks to Dr. Kozlowski for supporting and organizing weekly lab meetings giving me and other trainees to give and get honest feedback on preliminary work - I learned a tonne through these meetings.

I am fortunate enough to have some truly excellent mentors that have guided me through my PhD program and introduced me to the world of educational leadership. Special kudos to Dr. Simon Bates who has been, and continues to be an invaluable mentor and supporter of my pursuits in teaching and learning. Everything I know about teaching large classes has come from Simon - truly, thank you. Both he and Dr. Ido Roll were instrumental in my initial dabbling in physics education research and Ido took me under his wing and set me up with a solid foundation in the scholarship of teaching and learning (SoTL). I then met a community of like-minded individuals that I truly connected with on a deep and foundational level - SoTL specialists, thank you for the debates, conversations, and most importantly, your friendship.

My first big SoTL project was with Drs. James Charbonneau and Chris Addison and it dealt with the idea of measuring interdisciplinarity in undergraduate students, particularly in the Science One program. All together we learned so much in this project and I will forever be thankful for the opportunity to work on such a

fun project! Dr. Georg Rieger gave me my first taste of teaching a class, and I will never forget the immense amount of trust and faith you placed in me. Many former graduate students were instrumental in my growth and development, and I owe a lot to Natasha Holmes, Ellen Schelew, Amanda Parker, Mike Sitwell, Emily Altieri, Jonathan Massey, and Jared Stang - you folks were amazing and I truly look up to you! Past, current, and former members of PHASER, thank you for giving me a place to feel at home discussing everything related to physics education.

Finally, last but certainly not least, a huge note of gratitude goes to my parents, brothers, family, and of course my wife Hira, who has supported and humoured me through my meanderings over the course of my PhD. *I love you all.*

# **Chapter 1**

## **Introduction**

Cancer is a disease that can occur at any age but mostly affects Canadians fifty years and older. Based on estimates from 2010, 49% of men and 45% of women are expected to develop a type of cancer during their lifetimes and one in four Canadians are expected to die from cancer-related diseases [10]. One approach to achieving better patient outcomes and reducing toxicity in cancer patients is to improve our understanding of tumour progression and treatment in preclinical tumour models using biological markers, also called biomarkers. In 2001, the National Institutes of Health commissioned a working group to create standards and definitions for what would constitute an effective biomarker. A biomarker is “a characteristic that is objectively measured and evaluated as an indicator of normal biological processes, pathogenic processes, or pharmacologic responses to a therapeutic intervention” [11]. There is an urgent need for the development of new imaging biomarkers to aid in the development of more targeted tumour therapies [12]. There has been considerable interest in the potential of predictive biomarkers for early assessment of tumour therapies. In this thesis, we aim to develop imaging-based biomarkers to explore the tumour microenvironment.

### **1.1 Cancer biomarkers and targets**

Hanahan and Weinberg catalogued a vast array of factors that contribute to tumour growth and provided a framework for understanding of diseases that result in ab-

normal cell growth [4, 13]. These “hallmarks of cancer” are “essential alterations in cell physiology that collectively dictate malignant growth in tumours” [13]. These hallmarks are summarized in Figure 1.1 and the work presented in this thesis focuses on the 5th hallmark, angiogenesis - the process by which new blood vessels form.

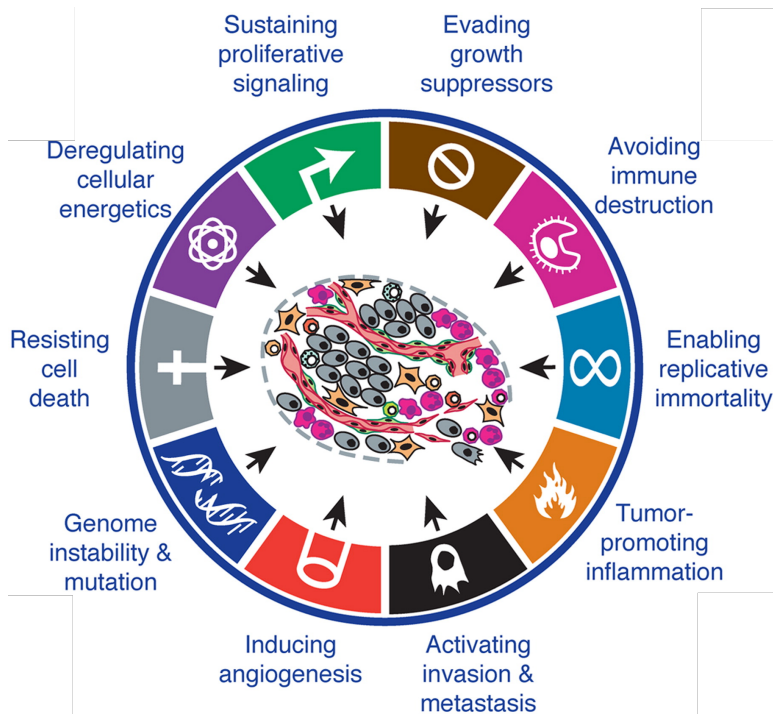


**Figure 1.1:** Graphical illustration of the hallmarks of cancer as presented by Hanahan and Weinberg [4]. Many of the targets described are inaccessible to non-invasive imaging and in this thesis, we focus on angiogenesis as the target of our imaging methods. Figure used with permission from Elsevier Inc.

Angiogenesis is the formation of new blood vessels from pre-existing ones is a normal and vital process in the body tightly regulated by various cell signalling pathways and growth factors. In tumours, angiogenesis is a critical step in the growth and spread of tumours as new blood vessels are recruited from the existing vascular network to promote rapidly accelerated and abnormal tumour growth [14].

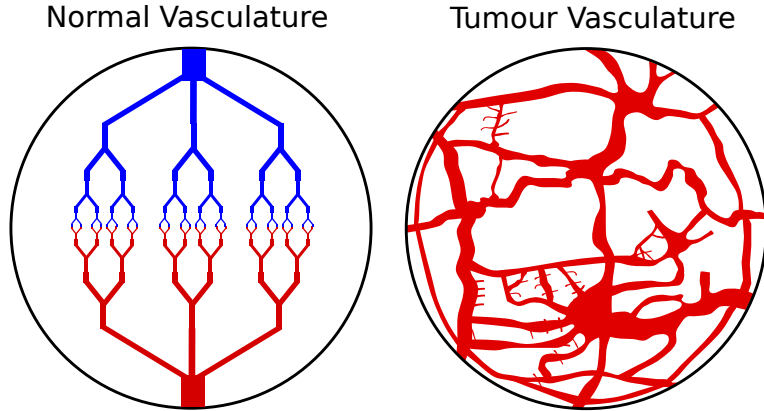


**Figure 1.2:** Schematic of the normal tissue (left) and tumour (right) vasculature network. Note the hierarchical structure of oxygenated blood (red) passing through the arteries, arterioles, and deoxygenated blood leaving via the venules, veins. In tumours, this structure is severely compromised and often, no clear flow patterns can be distinguished with many vessels ending in dead ends or looping back onto feeding vessels.

Normally, this process is regulated by several angiogenic and antiangiogenic factors such as  $\alpha\beta$  integrin, vascular endothelial growth factor (VEGF) and fibroblast growth factor [15]. In tumours however, this process is deregulated (Figure 1.2) and excess production of growth factors from rapidly proliferating tumour cells leads to a drastic increase in angiogenesis. These newly formed vessels are unstable growth patterns of blood vessels in tumours are often described as abnormal with a defective and leaky endothelium [16]. Irregular diameters of tumour vessels, abnormal branching patterns and leaky vessel walls all contribute to an increase in vessel permeability. It is estimated that a single hole larger than  $0.5\mu\text{m}$  in diameter would alter the permeability of that vessel significantly enough to result in solute extravasation to be limited by blood flow [16]. Disorganized and inefficient blood flow also limits the delivery of macromolecules, such as chemotherapeutic agents via the blood. Poor perfusion in the tumour due to a disorganized vascular network impairs the delivery of systemic drugs to the whole tumour and ultimately, reduces efficacy.

Tumour angiogenesis is extremely important in tumour growth, progression

and metastasis and is a promising target for novel therapies [17]. For instance, measuring tumour angiogenesis has the potential to serve as a highly predictive prognostic marker for disease outcome and treatment. Measurement of microvessel density using histology is generally considered an independent prognostic factor in several cancers [18] but has several limitations. Histology requires biopsy samples and patient comfort aside, biopsies only sample a small fraction of the affected organ. The lack of functional information from biopsies as well as the practical challenges of obtaining longitudinal biopsy samples make non-invasive imaging a promising technique to complement and potentially reduce unneeded biopsies. Angiogenesis is especially suitable for analysis with MRI due to its exquisite soft-tissue contrast, ability to image deep into the body, and finally its utility in assessing vascular function using injectable contrast agents.

## 1.2 Animal models of cancer

Developing models of human cancers in mice that predict clinical outcomes is beneficial as failure of novel chemotherapy drugs is often not determined until significant investments of time and money have been made designing and implementing phase I, II and III clinical trials [? ]. Animal models of cancer are essential for drug development, investigating mechanisms of action of physical phenomena, identifying gene targets, and protocol development prior to translating to human patients. According to Céspedes et al., an ideal cancer model should have the following characteristics [? ]:

1. Share histopathological features with the human tumour,
2. Progress through the same stages and result in the same physiological and systemic effects,
3. Share the same genes and biochemical pathways in both tumour initiation and tumour progression,
4. Reflect the response of the human tumour to a particular therapy and
5. Predict therapeutic efficacy in human clinical assays.

Despite this, it is widely acknowledged that the translation potential of subcutaneous tumour xenograft models is limited particularly for translating chemotherapies to humans that have been shown effective in mice [? ? ]. Naturally arising tumours often take years to months or years to grow but mouse xenograft models are selected so that experiments can be completed in days or weeks [? ]. The tumour vasculature that forms from injected tumour cells is fundamentally different from tumours that arise *in vivo* as it lack the architectural and cellular complexity often seen in real tumours [? ]. Vessels in xenograft models typically grow much faster, are more chaotic in structure, have a leakier endothelium, and do not have much smooth muscle to regulate blood flow [? ? ].

The heterogeneity of tumours also makes translation to humans difficult as within a specific tumour, several cell subpopulations exist that differ in their morphology, growth rate, receptor status and sensitivity to therapeutic potential [? ? ]. There are also regional differences in pH, degree of oxygenation, nutrient concentration that result in scattered pockets of hypoxia, apoptosis and necrosis throughout the tumour [? ? ? ]. Vascular reorganization, particularly following treatment[? ? ], leads to an irregular and shifting tumour microenvironment, a moving target for imaging modalities [15]. However, measuring these changes functionally, longitudinally, and non-invasively with imaging techniques has the potential to greatly improve our understanding of the tumour microenvironment. Care must be taken not to over-interpret and generalize results from preclinical cancer studies. Significantly more work needs to be done to obtain clinically relevant animal cancer models, but in the interim, animals models provide researchers with a valuable platform for developing novel agents of potential targets.

### 1.3 Need for non-invasive imaging

Non-invasive imaging methods are proving indispensable for studying angiogenesis *in vivo* as they provide researchers with quantitative information about blood flow, vascular permeability, vessel density, vessel function and blood volume [19]. Imaging modalities such as computed tomography (CT), magnetic resonance imaging (MRI), positron emission tomography (PET), single photon emission computed tomography (SPECT) and ultrasound (US), have all been proposed for studying

angiogenesis [15]. Each modality is optimal for probing a particular aspect of biomarkers. To study angiogenesis and its effects on tumour growth and treatment response, the tumour environment needs to be probed using minimally invasive imaging techniques. Nuclear medicine techniques such as PET and SPECT employ radiotracers that can be measured at picomolar concentrations but at a significantly lower spatial resolution. DCE-MRI and DCE-CT offer similar perfusion measurements (rate of leakage and leakage space) as both rely on the administration of a contrast agent that diffuses from the vasculature. DCE-CT is advantageous as it has a direct linear relationship between the contrast agent concentration and the image intensity (attenuation numbers, given by Houndsfield Units) [20]. The disadvantage of CT however is that it requires ionizing radiation and iodinated contrast agents used in CT have been shown to have worse safety profiles compared to MR contrast agents [21]. MRI can also be used to measure additional information such as diffusion, tissue oxygenation, spectroscopy, chemical exchange and magnetization transfer. In this thesis, several MRI techniques will be explored in a bid to improve our understanding of the tumour microenvironment. We begin with some basic principles of MRI.

## 1.4 Principles of Magnetic Resonance Imaging

In biological specimens, water is by far the most abundant molecule in the body and the hydrogen atoms ( $^1\text{H}$ ) in water are central to MR imaging. Other MR-active nuclei include  $^{13}\text{C}$ ,  $^{19}\text{F}$ ,  $^{23}\text{Na}$  and  $^{31}\text{P}$ , but these are rare and not often used. The molecular mass of a water molecule ( $\text{H}_2\text{O}$ ) is approximately 18 g/mol and its density is 1 g/mL so in 1L, there are approximately  $3 \times 10^{25}$  molecules of water. At the atomic level, each molecule of water consists of one oxygen atom (eight protons, neutrons, and electrons) as well as two hydrogen nuclei (a neutron and proton). An intrinsic quantum mechanical property of fundamental particles such as the proton, neutron, and electron is that they possess angular momentum. There are two types of angular momenta, spin and orbital angular momentum. The proton and neutron possess only spin angular momentum but electrons also possess orbital angular momentum. For electrons the two angular momenta nearly always cancel out in the lowest energy state of a chemically stable molecule such as water [22].

The hydrogen nucleus has an odd number of protons ( $n=1$ ) so there is a net spin angular momentum. In fact, the only sources of angular momentum in the ground state are the molecular rotation and the nuclear spins associated with the proton and neutrons [22]. Nearly all of the MR signal being measured in the body is derived from the hydrogen nuclei in water.

To summarize, each proton in the hydrogen nucleus has spin angular momentum, is charged and thus has a net magnetic moment. Though there is no analogy to this from a classical physics perspective, one can imagine the net magnetic moment of a proton as a close cousin to the classical situation of the magnetic field generated by a loop of current in a wire. We will model the hydrogen atom with a net magnetic moment as a small bar magnet spinning on its own axis (with an arrow vector representing the direction and strength of the magnetic moment) and rely on classical physics to describe the principle of magnetic resonance imaging. If a spinning bar magnet is placed in an external magnetic field, the magnetic moment vector of the bar magnet will precess, or rotate about the new magnetic field with a frequency known as the Larmor frequency:

$$\vec{\omega} = \gamma \vec{B}_0 \quad (1.1)$$

The proportionality factor  $\gamma$  is the gyromagnetic ratio and is nuclei-dependent and for protons,  $\gamma = 42\text{MHz}/T$ . For convenience it is useful to change our reference frame to a rotating reference frame so the the magnetic moment vector is stationary on a (rotating) cartesian axis.

The quantity of interest in MRI is the net magnetic moment  $\vec{M}$ , and this is the summation of all individual magnetic moments present in the hydrogen nuclei.  $\vec{M}$  is the quantity that is measured and ultimately leads to the images produced. Figure 1.3A shows a schematic of the situation; for visualization, individual magnetic moments from the protons are localized to originate from the same central point. Since the water molecules are tumbling around due to thermal motion, the proton magnetic moments are oriented randomly they are pointed in nearly every direction and there is no net magnetic moment (Figure 1.3A). If we now put these water molecules into an MRI scanner and switch on a main magnetic field of strength  $\vec{B}_0 = 7$  Tesla, there is a slight tendency of protons to align with the main magnetic

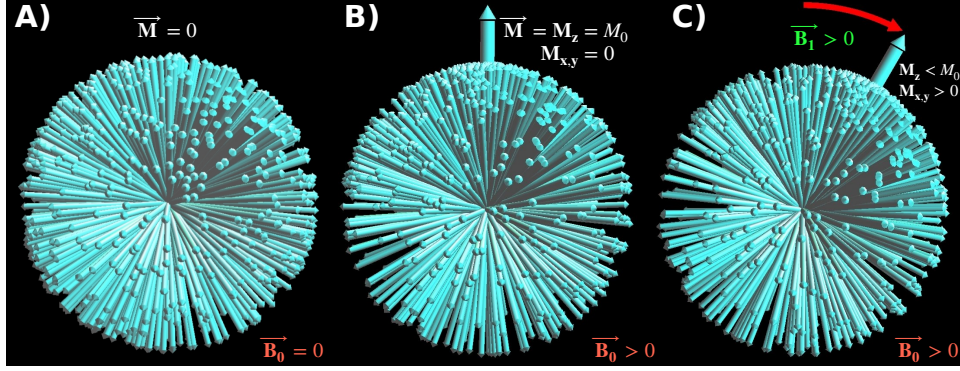


**Figure 1.3:** A) a collection of protons with magnetic moments are represented by arrows pointing in the direction of the magnetic moment, starting from a common starting point (centre). B) After switching on a main magnetic field  $\vec{B}_0$ , the net magnetic moment  $\vec{M}$  slightly aligns with  $\vec{B}_0$  because a larger fraction of spins point in the direction of the main magnetic field (in the rotating frame). C) The net magnetization moment is tipped to the transverse axis with an RF pulse  $\vec{B}_1$  so the signal can be measured. Annotations were added to the simulated images produced by Hanson et al.([5]), used with permission from Wiley and Sons.

field  $\vec{B}$  (along z axis, see Figure 1.3B), and a net magnetization vector  $\vec{M}$  is present.  $\vec{M}$  aligns with  $\vec{B}_0$  and the longitudinal component  $M_z = M_0$  while the transverse component  $M_{x,y} = 0$  (in the x-y plane).  $\vec{M}$  is many orders of magnitude smaller than the external magnetic field so the MR signal cannot be measured when it is aligned with the external main magnetic field  $\vec{B}_0$ . Applying a radiofrequency (RF) pulse  $\vec{B}_1$  at the Larmor frequency results in a torque applied to  $\vec{M}$ , causing it to ‘tip’ down into the transverse (x-y) plane (Figure 1.3C).

Interacting nuclei exchange energy with both the surrounding environment (spin-lattice interaction) as well as neighbouring nuclei (spin-spin interaction), and  $\vec{M}$  relaxes back to its equilibrium value. The time constant of the recovery of  $M_z$  to its equilibrium value  $M_0$  is characterized by the time  $T_1$ ,

$$M_z = M_0(1 - e^{-t/T_1}) \quad (1.2)$$

$T_1$  s after the RF pulse, the magnetization value has recovered to  $\approx 63\%$  (1-

$e^{-1}$ ) of its equilibrium value. Prior to the  $\vec{B}_1$  pulse, the transverse component of the initial magnetization  $\mathbf{M}_{x,y}$  was 0. Following the  $\vec{B}_1$  pulse,  $\mathbf{M}_{x,y}$  decays from its maximum value of  $M_0$  to 0 through the interactions between nuclei and is characterized by the time constant  $T_2$  (also called spin-spin relaxation).

$$M_{xy} = M_0 e^{-t/T_2} \quad (1.3)$$

Although  $T_1$  and  $T_2$  values are affected by various factors including field-strength, and local environmental factors such as temperature, proton concentration, and molecular mobility. Differences in  $T_1$  and  $T_2$  values are used to generate contrast between different tissues. For example, in a study conducted with ten volunteers at 1.5T, the spleen ( $T_1 = 919$  ms), liver ( $T_1 = 616$  ms), muscle ( $T_1 = 785$  ms), fat ( $T_1 = 239$  ms), and renal cortex ( $T_1 = 919$  ms) all had measurably different  $T_1$  values [23]. Contrast between tissues can be generated by weighting images to highlight differences between  $T_1$ ,  $T_2$ , and proton density. In the next section, the sequence of choice for  $T_1$ -weighted images is described.

#### 1.4.1 MRI sequences

$T_1$ -weighted images can be produced using both a spin echo pulse sequence as well as a gradient echo. In a spin echo sequence, the magnetization is first flipped down to the transverse plane with a  $90^\circ$  RF pulse. Then the magnetization in the transverse plane is allowed to gradually de-phase and subsequently, a  $180^\circ$  RF pulse is applied causing the spins to re-phase. Once the spins re-phase, an echo is produced and the time from the initial  $90^\circ$  to the eventual echo is the echo time,  $T_E$ . The  $180^\circ$  refocusing pulse is applied  $T_E/2$  after the initial  $90^\circ$  pulse. Specifying the  $T_E$  allows control of image weighting - either  $T_1$ ,  $T_2$  or mixed weighted. The repetition time  $T_R$  is another important sequence parameter that controls how much magnetization, or signal is available to be flipped down to the transverse axis. The repetition time is the time between subsequent  $90^\circ$  RF pulses - the longer the  $T_R$ , the more the longitudinal magnetization recovers and is available to be tipped down to the transverse plane at the next  $90^\circ$  RF pulse.

In a gradient echo sequence, only one RF pulse is needed to flip the magnetization to the transverse plane, and unlike the spin echo sequences, gradients are used

to de-phase and re-phase the transverse magnetization. The interpretation of  $T_E$  is similar in a gradient echo and also measures the time between the 90° pulse and the echo produced after gradient re-phasing. Compared to the spin echo sequence, the use of gradients permits significantly shorter echo times and repetition times -  $T_E$  and  $T_R$  respectively. This is why, in typical DCE-MRI experiments, gradient echoes are preferred because signal acquisition is significantly faster allowing rapid and dynamic imaging. To ensure there is no transverse magnetization after each repetition of the gradient echo sequence, spoiling is needed to suppress creation of spin and stimulated echoes. The signal from a spoiled gradient echo (SPGR) sequence with spoiling and after steady state has been achieved is given by [? ]:

$$S = k \frac{\sin \alpha (1 - e^{-T_R/T_1})}{(1 - (\cos \alpha)e^{-T_R/T_1})} e^{-T_E/T_2^*} \quad (1.4)$$

where  $k$  is a proportionality constant that also includes the proton density. In practice, if  $T_E$  is small and close to  $T_2^*$ , this term (as it often is in SPGR sequences) approaches unity and is negligible. The signal characteristics of a spoiled gradient echo (SPGR) sequence is also shown in Figure 1.4 with a specific  $T_1$  of 2200 ms (typical  $T_1$  values in tumours studied in this thesis) and with a  $T_R$  of 120 ms.

The maximum signal intensity under these conditions is given by the Ernst angle, obtained by setting the derivative  $dS/d\alpha = 0$ :

$$\alpha = \arccos(e^{-T_R/T_1}) \quad (1.5)$$

It is important to note that the Ernst angle maximizes the signal at a particular flip angle given a specific intrinsic  $T_1$  but often it is necessary to optimize the signal difference between two (or more) species with different  $T_1$  values. The difference in signal intensities is the contrast ( $\Delta SI$ ) between two tissue types. The maximum contrast difference for two tissues with  $T_1$  values of 2200 and 1760 ms is marked with a solid black line in Figure 1.4. In Figure 1.5, the contrast ( $\Delta SI$ ) and the  $T_R$ -normalized contrast ( $\Delta SI / \sqrt{T_R}$ ) is shown as described by Busse [? ]. From this figure - particularly the  $T_R$ -normalized contrast - we note that choice of  $T_R$  is largely independent of optimizing contrast and there exists an optimal choice of flip angle regardless of the  $T_R$ . This is important because very often, other factors

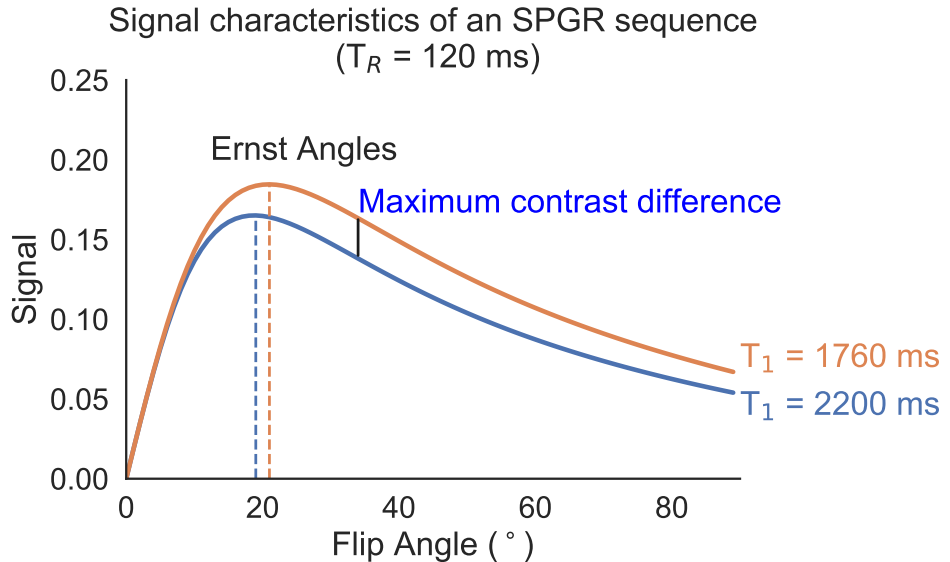


**Figure 1.4:** Dependence of flip angle on the signal from an SPGR sequence for two tissues with  $T_1$  of 2200 and 1760 ms respectively. The Ernst angles for each tissue is marked with dotted lines, and the flip angle that would result in the maximum contrast difference is marked with a solid black line.

such as SNR, temporal, and spatial resolution constrain the minimum  $T_R$ .

For the sequences used in this thesis, competing factors were considered including imaging time,  $T_1$ -weighting, image intensity, SNR, image contrast, temporal, and spatial resolutions; appropriate compromises and trade-offs were made to balance the trade-offs to produce maximum benefit. Another tool at our disposal is the paramagnetic contrast agents as they are often used to increase the  $T_1$  contrast between different species. The following sections outline how dynamic contrast-enhanced MRI or DCE-MRI is used in the imaging of cancer.

#### 1.4.2 Paramagnetic contrast agents

Paramagnetism is defined as the intrinsic tendency for a material to become magnetized when placed within a magnetic field. By far the most common element used as a contrast agent (tracer) in MRI is Gadolinium as it is strongly paramag-

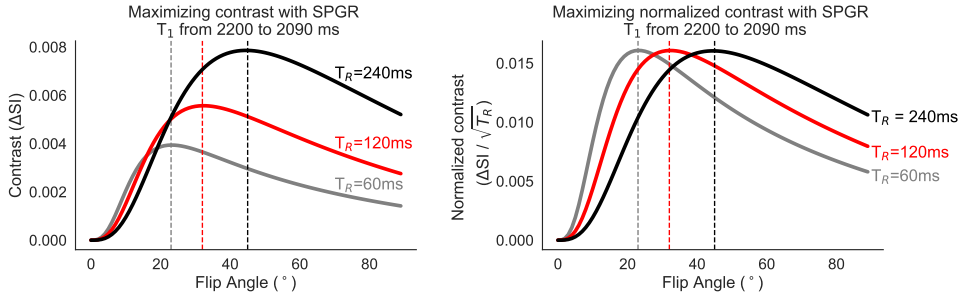


**Figure 1.5:** On the left, the contrast ( $\Delta SI$ ) for two tissues with  $T_1$ s of 2200ms and 2090ms for three  $T_R$ s are plotted along with the Ernst angles for each  $T_R$ . As the  $T_R$  increases, the total available signal also increases because the magnetization has longer to recover. On the right, the curves are normalized by the  $T_R$  which is more useful in optimizing sequence parameters. The three chosen repetition times (240ms in black, 120ms in red, and 60ms in grey) represent the range of  $T_R$ s used in the work presented in this thesis.

magnetic due to its seven unpaired electrons. Because electrons are much smaller than protons but have the spins, they have a significantly higher gyromagnetic ratio. The unbalanced electrons in the gadolinium shell or bonding orbital result in a strong net magnetic moment, which interacts with hydrogen nuclei and dramatically reduces the longitudinal relaxation time  $T_1$  (and to a lesser extent  $T_2$ ). Unfortunately, free Gadolinium ions are toxic so they need to be attached to an organic chelating agent [24].

The ability for a contrast agent to affect the  $T_1$  relaxation time is given by its relaxivity  $r_1$ , obtained from the following equation:

$$\frac{1}{T_1} = \frac{1}{T_{10}} + r_1[Gd] \quad (1.6)$$

where  $T_{10}$  is the initial  $T_1$ , prior to the influence of the paramagnetic contrast agent,  $r_1$  is the relaxivity of the contrast agent in units of  $(mM\cdot)^{-1}$ , and  $[Gd]$  is the contrast agent concentration. It is important to note that all contrast agents shorten both  $T_1$  and  $T_2$  but whether their dominant influence is on the transverse relaxation time ( $T_2$ ) or the longitudinal relaxation time ( $T_1$ ) is expressed by the relative strengths of  $r_1$  and  $r_2$ .

### 1.4.3 Dynamic contrast-enhanced MRI (DCE-MRI)

Through the use of a paramagnetic contrast agent, DCE-MRI techniques increase contrast between species whose  $T_1$  and  $T_2$  times are otherwise very similar. However the true value of DCE-MRI comes from extracting physiologically relevant information from the body. In applications of cancer imaging, DCE-MRI has been extremely successful in diagnostics, treatment monitoring, assessing severity of pathologies, distinguishing between tumour models and types, improving our understanding of tumour metastases, and development of drugs.

Health Canada has approved eight gadolinium-based contrast agents for use in humans and they have molecular weights less than 1 kDa that readily traverses the endothelium but not the cell membrane [25]. This property allows modelling of the vascular dynamics of the tumour but because the contrast agent is small, perfusion and permeability cannot be decoupled without extremely fast imaging and accurate knowledge of the arterial input function (AIF)[26]. Choosing a kinetic model to fit the data requires some prior knowledge about the organ or system in question. For instance, the blood-brain barrier in the brain dramatically alters the contrast agent kinetics. Similarly, in leaky tumours the extravascular contrast agents typically used in DCE-MRI leak out (and back in) of vasculature considerably faster than in other tissues. Sourbron et al. postulate that choice of a tracer kinetic model should provide a link between relevant physiological parameters and measured data [26].

The most widely used model in DCE-MRI is the extended Toft's model, which is valid in highly perfused tissues and weakly vascularized tissues with a well-mixed extravascular extracellular space ( $v_e$ ) [27]. Figure 1.6 provides a graphical description of this two compartment model, and its mathematical representation is:

$$C(t) = v_p \cdot AIF(t) + K^{trans} e^{-t \frac{K^{trans}}{v_e}} * AIF(t) \quad (1.7)$$

where  $v_p$  is the plasma volume,  $K^{trans}$  is the volume transfer constant, and the  $AIF(t)$  is the arterial input function which needs to be measured independently of the contrast agent kinetics in the tissue.

In this thesis, DCE-MRI modelling using a traditional small molecule agent (Gd-DTPA is used only briefly in Chapter 2 and the AIF used in that modelling was measured and published by a former lab member [28]. Nevertheless, the concepts

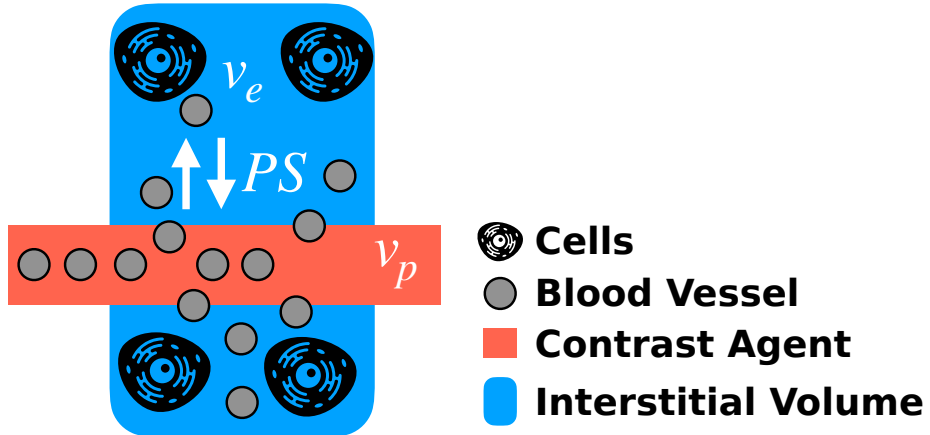


**Figure 1.6:** Graphical description of the Extended Tofts Model. An arterial input function (AIF) governs the introduction of the tracer (grey circles) in the vascular compartment (pink) via a bolus injection. Contrast agent molecules exchanges with the extravascular extracellular space ( $v_e$ , interstitial volume in blue) at a rate given by  $PS$ , the permeability-surface area product.

and introduction to DCE-MRI are relevant for several portions of the thesis.

## 1.5 Thesis structure

In **Chapter 2** a new macromolecular contrast agent is described and its value in describing the tumour microenvironment was explored. A two-parameter linear model was applied to the contrast agent enhancement curve and measures of vessel permeability and fractional plasma volume were obtained. These parameters were then used to distinguish between two tumour models. In **Chapter 3**, this technique was applied to determine whether molecule size played a role in the distribution of a high molecular weight anti-cancer drug (trastuzumab). We showed that neither vessel permeability nor fractional plasma volume corresponded to presence of bound drug (determined via histological staining), indicating other barriers limit distribution of trastuzumab *in vivo*. In **Chapter 4** we set out to determine whether our new contrast agent could assess changes in vessel permeability after treatment

with an anti-angiogenic drug. We discovered not only that vessel permeability is indeed reduced after treatment, but also that hypoxia dramatically decreased after treatment, as predicted by the vascular normalization hypothesis [29]. This led us to develop a new method for assessing tumour oxygenation *in vivo* using MRI. In **Chapter 5**, we outlined how a blind source separation technique increased the sensitivity of existing methods. The technique was validated in **Chapter 6** with histological staining, and we demonstrated utility of a new parameter to separate oxygenation replenishment in different tumour models. Finally in **Chapter 7** we showcase a typical application of the technique: detection of tumour oxygenation improvements after administering an anti-angiogenic agent. We also showed that the tumour implant site has a large bearing on the tumour microenvironment, and no oxygenation improvements are observed if the baseline oxygenation is high. In **Chapter 8**, interesting observations are presented that may be useful starting points for future work in this field.

## **Chapter 2**

# **Multi-modal magnetic resonance imaging and histology of vascular function in xenografts using macromolecular contrast agent hyperbranched polyglycerol (HPG-GdF)**

### **2.1 Introduction**

The vascular network in tumour tissue is abnormal, often resulting in vessels that have variable flow rates and high permeability relative to blood vessels in normal tissue [16]. Dynamic contrast-enhanced magnetic resonance imaging (DCE-MRI) is a useful tool for non-invasively assessing tumour vasculature by imaging and measuring concentrations of CA delivered to tumours by the vessels [30–32]. The appeal of a dynamic, non-invasive approach for measuring tumour vascular function in the clinic is clear. Such data is applicable in the field of assessing treatment response for vascular targeting therapies [30–32]. In addition to utility as a treat-

ment biomarker, vascular function data may be able to predict which tumours are likely to respond to therapy [33–35], or which regions or tumours have greater heterogeneity in their microenvironment [36, 37]. The issue of its limited access for anticancer drugs in solid tumours is significant [38], particularly given the efforts to create nanoparticle therapeutics that target the tumour via the EPR effect [39–41]. A translatable imaging protocol and suitable contrast agent that yields meaningful and reproducible biomarkers of vascular function could be widely useful in these areas of cancer research.

Low MW Gd(III)-based, chelated CAs such as Gadovist (MW = 605 Da) exhibit short half-lives and rapid renal clearance [42]. With the exception of brain tissue containing a functional blood-brain barrier, low MW Gd agents currently in clinical use diffuse across the vascular endothelium in most normal and neoplastic tissues. Therefore, a well-established shortcoming of low MW contrast agents is the difficulty of attributing local signal enhancement specifically to either vascular perfusion or vessel permeability. The ability to characterize physiologically relevant biomarkers of vascular function is desirable for studying the effects of anti-angiogenic treatments in tumours (described in a comprehensive review regarding DCE-MRI and anti-vascular therapies in cancer [30]).

Development and application of macromolecular contrast agents (MCAs) attempt to improve upon DCE-MRI assessment of vascular function by relying on the primarily intravascular nature of MCAs. High MW contrast agents and therapeutics unable to diffuse across the endothelium selectively extravasate from large pores and inter-endothelial cell gaps that characterize the abnormal vessels in the tumour microenvironment [16, 43]. MCAs commonly used in cancer research include albumin, dextran polymers, and dendrimers conjugated with DTPA/DOTA-Gd<sup>3+</sup> chelates as described by Tang et al. [44]. Size of MCAs is often reported both in molecular weight (kDa) and longest diameter (nm) where available. MCAs under development range considerably, but dextran-based agents have been proposed from 15 kDa-3820 kDa [31]. Particles less than 5 nm in size have been found to leak rapidly from tumour vasculature, whereas those in the 5-8 nm range are limited to leaking from hyperpermeable vessels; those greater than 8 nm are thought to have minimal leakage [45, 46]. The most commonly used MCAs in pre-clinical research are albumin based (90 kDa); however, these are not translatable

to the clinic due to immunogenicity concerns [47].

For intravascular MCAs, signal enhancement is linked to contrast agent concentration within the tumour blood vessels at early time points after injection. Rates of MCA leakage from hyperpermeable vessels may then be modelled to evaluate permeability, since extravascular accumulation of the agents will manifest as increased enhancement in repeat images [47, 48]. This analysis is dependent on the assumption that the MCAs have unidirectional flow and do not leak back into the plasma, and that the concentration in the plasma is constant, creating a permeability-limited environment.

In this study we investigated a multi-modal, high MW contrast agent, HPG-GdF: hyperbranched polyglycerol molecules doubly labeled with Gd-DOTA and a fluorescent marker. HPGs are soluble, globular, asymmetrical, have low immunogenicity and are highly biocompatible molecules with low polydispersity [6, 49, 50]. HPG has been previously tested as a human serum substitute [51] and as a drug delivery vehicle due to its versatility as a chemical, such that drugs, Gd chelates, fluorescent and radiolabels may all be attached to it [52]. Many other MCAs, including Gd-albumin, are highly viscous, which can limit the applicable dose [53]. The MW of HPG-GdF can be adjusted for different applications, and a biodegradable version of HPG is also available for potential use [52]. The HPG-GdF described in this study is 583 kDa and 8-10nm in diameter; synthesis of HPG-GdF has previously been described [6]. A significant advantage of HPG-GdF is that it is a multi-modal agent, with both fluorescent and Gd-chelate labels that permit histological validation of observations made using MRI, including determining the degree to which the agent extravasates from the vasculature. Previous studies have also used  $^{111}\text{In}$  as a SPECT label with utility for biodistribution studies [6]. In this work, we employed comprehensive histological methods to investigate the microregional location of HPG-GdF in two human colorectal xenograft models, and used this information to interrogate observations made non-invasively using DCE-MR imaging of the same agent in the same tumours.

## 2.2 Methods

### 2.2.1 Mice and tumours

Female NOD-SCID mice were bred and housed in institutional animal facilities; experiments in this study were approved by the Animal Care Committee of the University of British Columbia. Fiducial markers were constructed of PE-50 polyethylene tubing (inner diameter, 0.58mm) and filled with paraffin wax and saline, creating an MR-visible interface [35]. Marker tubes were implanted subcutaneously in the sacral region of mice, in a craniocaudal orientation, 2 days prior to subcutaneous implantation of tumours. Both histology and MR slices are imaged in the plane perpendicular to the marker tube to minimize angular differences between serial MR image slices obtained over multiple sessions, and for corresponding cryosections in histological processing. HCT116 or HT29 human colorectal carcinoma cells obtained from the American Type Culture Collection (ATCC) were implanted near the fiducial tubes such that the tumours grew around the tubes. Tumours were used when diameters reached 8-12 mm. Mice were anaesthetized with isoflurane for the duration of imaging sessions. Animals were positioned supine on the custom surface coil apparatus fitted with a lid lined by a temperature-controlled, water-filled heating blanket. Body temperature and respiration rate were monitored throughout imaging. Following their final scan animals were administered a 35  $\mu$ L intravenous dose of 0.6 mg/mL carbocyanine (DioC7(3); Molecular Probes, Eugene, OR, USA) in 75% dimethylsulfoxide as a fluorescent dye indicator of vessel perfusion in histological measures, and euthanized 5-min after injection. Given enough time, carbocyanine freely diffuses throughout the tumour tissue but with a limited exposure time (less than 5 minutes), it serves as a good vessel perfusion marker [80]. Some animals received HPG-GdF and tumours were collected at early time points for histological analysis only, with no MR-imaging. Tumours were embedded and frozen vertically in optimum cutting temperature medium (OCT; Tissue-TEK) using their fiducial markers for guidance.

### **2.2.2 Contrast agents and dosage**

Hyperbranched polyglycerol (Figure 2.1): 583 kDa HPG-GdF was synthesized at the University of British Columbia (D. Brook's laboratory, Department of Chemistry) with a narrow polydispersity of PDI = 1.01 by ring-opening multibranching polymerization of glycidol using dioxane as the reaction medium, according to a published procedure [49]. HPG was derivatized with p-NH<sub>2</sub>-benzyl-DOTA (Macrocyclics, Dallas, TX, USA) at 20 $\mu$ g Gd per mg HPG and tagged with Alexa Fluor 647 (Invitrogen Life Technologies, Burlington, ON, Canada) as previously described (20). The biological half-life of HPG-Gd (with no fluorescent tag) in mice has previously been examined in biodistribution studies and was reported as 32.6 h (20). HPG-GdF was administered as a 6  $\mu$ L/g bolus dose from 100 mg/mL (0.2 mM) using an intravenous (i.v.) catheter; therefore, the administered molar dose of HPG was 1.2 nmol/g and that of the chelated Gd(III) was 240–360 nmol/g (determined according to an estimated 200–300 chelates per HPG molecule (20)). Assuming a blood volume of 5% of mouse body weight, peak blood concentration of HPG-GdF is 24 $\mu$ M. This value has been used to normalize relative tissue concentrations (Figure 2.2(B)) and to calculate the fractional plasma volume (fPV; see section 2.2.4). The relaxivity of HPG-GdF has previously been measured and reported to be 1075 mM<sup>-1</sup>s<sup>-1</sup>, which is approximately 300 times greater than that of Gadovist (3.58 mM<sup>-1</sup> s<sup>-1</sup>) [6]. Gadovist (Bayer Healthcare, Toronto, ON, Canada; 607.4 Da) was administered by i.v. catheter as a 5  $\mu$ L/g bolus dose from 60 mM solution, for an administered molar dose of Gadovist of 300 nmol/g. All in-scanner i.v. injections were performed using a power injector at a rate of 1 mL/min. An extended fluid line connected to the i.v. catheter secured to the tail vein of the mice permitted remote initiation of injections outside the scanner room. Injections included a small volume (<40  $\mu$ L) of heparinized saline followed by the contrast agent, which was then followed by a 20  $\mu$ L flush of heparinized saline.

### **2.2.3 MRI acquisition**

All MRI experiments were performed at the UBC MRI Research Centre on a 7T Bruker BioSpec 70/30 scanner at room temperature with a combination of volume (transmit)/surface (receive) coil. Each imaging session began with axial RARE T<sub>2</sub>-

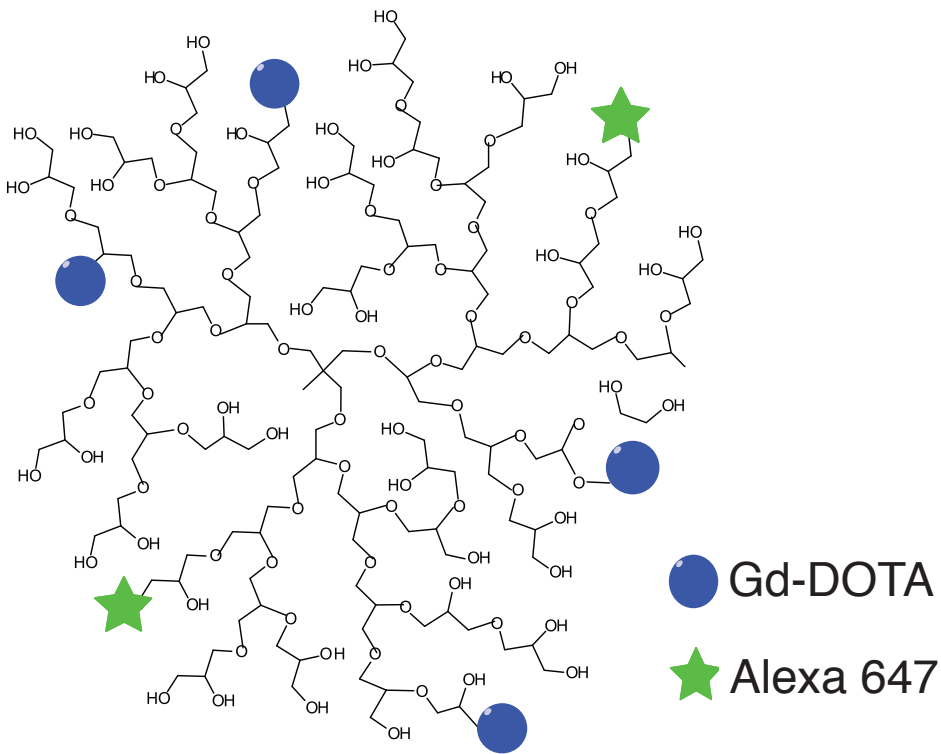


**Figure 2.1:** HPG-GdF. The 583 kDa globular Hyperbranched PolyGlycerol (HPG) molecules are derivatized with p-NH<sub>2</sub>-benzyl-DOTA (Macro cyclics) at 20 µg Gd per mg HPG (approximately 300 chelates per molecule) and tagged with Alexa Fluor 647 dye, as previously described [6]. Figure reused with permission from Wiley and Sons.

weighted images for morphological reference and precise alignment of imaging plane (RARE factor 8, effective  $T_E = 42.98$  ms,  $T_R = 4250$  ms, FA = 178°). In subsequent imaging sessions, slice location and orientation were adjusted to match previous sessions.

In the first scanning session,  $T_1$  and flip angle maps were acquired prior to the DCE-MRI experiment, followed by another  $T_1$  measurement.  $T_1$  measurements and flip angle mapping were performed using a multi-slice FLASH variable flip angle experiment (FLASH  $T_R/T_E = 500/2.75$  ms, FA = 10-200° in increments of

$10^\circ$ , and  $215^\circ$ ). Data were fit simultaneously for  $T_1$  and the  $B_1$  scaling factor map. DCE-MRI data was collected at 2.24 s time resolution (FLASH;  $T_R/T_E = 35/2.75$  ms; FA = 40; NR = 1200).  $T_1$  and DCE-MRI experiments all had identical geometry (matrix =  $128 \times 64$ ; three slices; voxel size =  $0.33 \times 0.297 \times 1.5$  mm $^3$ ; 2.5 mm slice separation). A follow-up  $T_1$  measurement was performed (FLASH;  $T_R/T_E = 35/2.75$ ; FA =  $10^\circ$ ,  $20^\circ$ ,  $30^\circ$ ,  $40^\circ$ ,  $50^\circ$ ,  $60^\circ$ ,  $80^\circ$ ,  $100^\circ$ ,  $120^\circ$ ) and the  $B_1$  scaling factor map from the baseline acquisition was used to determine post-contrast  $T_1$  (assuming that  $B_1$  scaling does not change due to contrast injection). Difference maps of relaxation rates  $\Delta R_1 = 1/T_1(\text{post-contrast}) - 1/T_1(\text{precontrast})$  were constructed for a measure of contrast agent concentration. Animals received two DCE-MRI scans 24–48h apart, with Gadovist administered and scanned at the first session and HPG-GdF administered and scanned at the subsequent session with tumours collected for histological processing at about 60-min post administration of their HPG-GdF. For qualitative assessment of contrast agent distribution  $T_1$ -weighted RARE images (RARE factor 4, effective  $T_E = 7.5$  ms,  $T_R = 1300$  ms, FA =  $180^\circ$ ) were acquired after contrast agent administration.

#### 2.2.4 MRI data analysis

Regions of interest (ROIs) were drawn on  $T_2$ -weighted RARE images to outline the tumour using ImageJ (NIH), and all other MR analysis was performed using MATLAB (MathWorks, R2009a) and Python.  $T_1$  and flip-angle maps were calculated from variable flip-angle data with a slice-profile correction based on simulations described by Parker et al. [54]. The same method was extended to provide time-dependent  $T_1$  and concentration-time in DCE data series. Areas under the curves (AUCs) were numerically integrated starting from the bolus arrival time, or, for tumour-averaged AUC, starting from the common injection time point and extended to the indicated time points (1 and 37 min). Bolus arrival time (BAT) is the time when detectable signal enhancement begins for a voxel (Figure 2.2(A)) due to contrast agent arrival. BAT maps from HPG-GdF and Gadovist obtained from the same HT29 xenograft imaged 24h apart show that HPG-GdF is slower to arrive; both CAs arrive most quickly at the tumour margins (Figure 2.2(A)). Based on the control-chart decision criterion and the Western Electric decision rules from

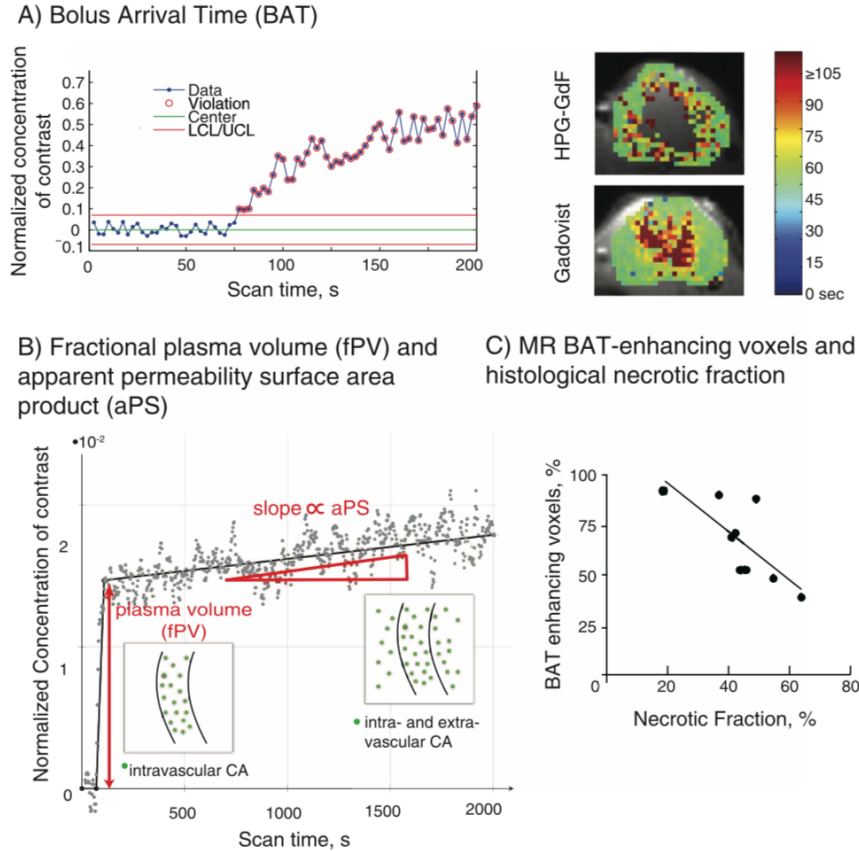


**Figure 2.2:** MR-derived parameters to measure vascular function using HPG-GdF: bolus arrival time (BAT), fractional plasma volume (fPV) and apparent permeability-surface area product (aPS). (A) Example of how the control theory procedure was applied to determine BAT on a sample enhancement curve showing change in concentration of CA as a function of scan time. The green line is the central line while the red lines indicate the upper and lower control limits (LCL and UCL). (B) HPG-GdF enhancement curve from which the fPV is derived as the concentration at the start relative to the plasma concentration. The aPS is the slope of the enhancement after the bolus arrival. The concentration curves are shown as ratio of tissue concentration to blood peak concentration ( $24 \mu\text{M}$ ). Insets within the plots are schematics of our interpretation of the situation at particular time-points and are not measured values. (C) The fraction of MR-measured HPG-GdF BAT-enhancing voxels has a negative association with the proportion of necrotic tissue determined in histological sections. Figure reused with permission from Wiley and Sons.

MATLAB's statistical toolbox [55], voxel enhancement was detected as a positive change from baseline signal for three consecutive timepoints (frames) (i) in the same direction, (ii) starting 5 s before the time of injection or later and (iii) for at least 10% of all timepoints following initial change of signal away from baseline. Therefore, voxels with a finite BAT and for which at least 10% of the following intensities were classified as enhancing by the BAT criteria were called enhancing voxels, whereas all other voxels were labeled as non-enhancing.

A former lab member developed a set of criteria based on control theory as part of their masters thesis [1]. A change from baseline was determined to have occurred when any one of the following inclusion criteria were met:

1. any point fell outside of 3 SDs from the average baseline concentration, or
2. two of three consecutive points fell outside of the 2 SD limit on the same side of the mean, or
3. four of five consecutive points fell outside of the 1 SD line, on the same side of the centre line, or
4. eight consecutive points all fell on one side of the centre line.

In the illustrated example (Figure 2.2(A)), a change from the mean was identified at Frame 31 and the two following scans by Rule (1); therefore, the BAT point was selected to be the 30<sup>th</sup> data point (t=67.2s). The centre line (mean of baseline) and upper and lower control limits ( $\pm 3$  SDs) are drawn for reference.

### **Pharmacokinetic modelling of DCE-MRI data**

*Gadovist:* The extended Tofts model was used and three parameters resulted:  $K^{trans}$ ,  $v_e$ , and  $v_p$  [26]. The arterial input function (AIF) for this model was determined previously by our laboratory using a projection-based method [28] and is a four-mouse population average.

**HPG-GdF** A two-parameter linear model was applied [56]. Two parameters were used to characterize the MCA time curves: (1) the rapid increase at the time of injection (related to the fPV) and (2) the slope of the later enhancement (aPS) (Figure 2.2(B)). The relative plasma volume could be determined from the ratio

of concentrations in the voxel of interest to the concentration in whole blood in the seconds after injection, since extra-vascular spread of the agent was negligible at this time. The slope of the concentration time curve following contrast arrival is proportional to the permeability-surface area product (PS) when the assumption of a permeability-limited environment is valid. However, in the highly variable tumour microenvironment, extravasation of contrast agent may deplete the intra-vascular concentration appreciably in conditions of high permeability, which would increase the relative contribution of perfusion to the composite measure of PS. To stress that the interpretation of this slope value depends on the assumption of a permeability-limited environment, we term the slope the apparent permeability-surface area product (aPS) [57, 58].

### 2.2.5 Histology

Cryosections of  $10\text{ }\mu\text{m}$  were obtained along the plane perpendicular to the fiducial marker at depths corresponding to MR imaged slices. Sections were imaged for DiOC7(3) and HPG-GdF native fluorescence and fixed in acetone-methanol for 10min prior to staining and re-imaging for CD31 and Hoechst 3342, labeling vascular endothelium and cell nuclei, respectively. Sections were imaged as previously described [59] using a system of tiling adjacent microscope fields of view such that images of entire tumour cryosections were captured at a resolution of  $1.5\text{ }\mu\text{m}/\text{pixel}$ . Using both fiducial and anatomical landmarks, histological sections were chosen to match the MR slices. Using ImageJ [60] and user-supplied algorithms, digital images were superimposed and manually cropped to tumour tissue boundaries; staining artifacts and necrosis were also removed for some analyses. Positive fluorescence for CD31 and DiOC7(3) images was obtained by applying a threshold, with neighbouring positive pixels grouped as “objects”. The average distance of tissue to the nearest vascular object was reported as a repeatable measure of vascular density. Perfused vessel fraction (PF) was calculated as the proportion of CD31-positive objects that had at least 20% overlap with positive DiOC7(3) or HPG-GdF pixels on the overlaid image. Data for individual tumours were displayed as mean  $\pm$  SEM values. HPG-GdF extravasation was assessed by its distance from blood vessels: pixels from the HPG-GdF fluorescence image were

sorted according to their distance from vascular objects and the average HPG-GdF fluorescence intensity was reported.

## 2.3 Results

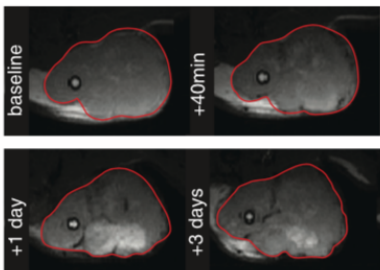
### 2.3.1 HPG-GdF accumulates in tumour tissue in the extravascular space but does not distribute far from vasculature

Averaged data from whole HT29 tumour xenograft images obtained using MRI and histology showed accumulation of HPG-GdF over time (Figure 2.3(A)), as previously described [6]. HPG-GdF fluorescence was detectable within or very near to CD31-labeled tumour vessels as early as 2-min following contrast agent injection (Figure 2.3(B), (C)). More HPG-GdF fluorescence accumulated in histological tumour sections over time, but very little agent was observed at distances farther than  $40\ \mu\text{m}$  from the vasculature, even at 7 and 15 days (Figure 2.3(B), (C)). By 60 min, there was extravascular accumulation of HPG-GdF around some vessels, but considerable inter-vessel heterogeneity was observed. Some vessels showed no HPG-GdF fluorescence (Figure 2.3(C)). Figure 2.3(C) also shows that HPG-GdF accumulates over several days but does so heterogeneously, and does not distribute through tumour tissue even after prolonged exposures.

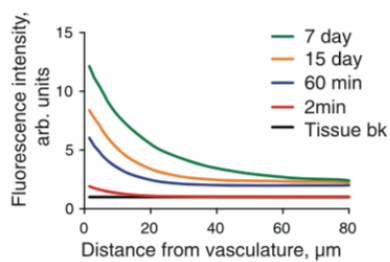
### 2.3.2 Bolus arrival time (BAT) for HPG-GdF as a screen for viable tissue

Maps of BAT overlaid on  $\text{T}_1$ -RARE images for both Gadovist and HPG-GdF are shown in Figure 2.4, rows 1 and 2. A pattern of faster contrast enhancement at the tumour margins was consistent for both contrast agents. While Gadovist eventually distributes to all the tissue, many voxels fail to enhance with HPG-GdF within the 37-min imaging period. Comparison of BAT-enhancing voxels with a histological image delineating viable versus necrotic tissue (Figure 2.4, Rows 2 and 3) shows that the non-enhancing voxels consistently corresponded to large areas of tumour necrosis. A negative association was seen between the histological necrosis fraction and the fraction of enhancing voxels for HPG-GdF (Figure 2.2(C)). For subsequent analysis of vascular function, only voxels enhancing with HPG-GdF

A) HPG-GdF accumulation in HT29 xenografts; RARE images



B) HPG-GdF distribution from vessels in HT29 xenografts



C) HPG-GdF in HT29 xenografts

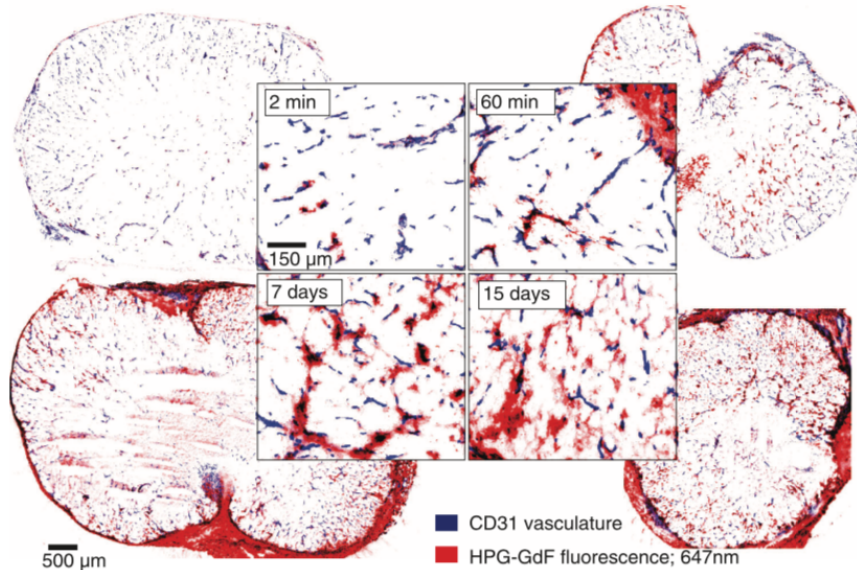


**Figure 2.3:** (A)  $T_1$ -weighted RARE images show signal enhancement at 40-min that increases with longer exposures (tumours outlined in red). (B) Quantitative histology shows HPG-GdF extravasation and distribution gradually increasing with time (2-min to 7 days). (C) Whole tumour maps of HPG-GdF (red) and vasculature (blue) show that at early (2 min) timepoints HPG-GdF is primarily overlapped with vasculature, but by 60-min there is substantial heterogeneity, where some vessels have greater amounts of perivascular HPG-GdF than others. Figure reused with permission from Wiley and Sons.

using the BAT criteria were evaluated.

### **2.3.3 Fractional plasma volume (fPV) and apparent permeability-surface area product (aPS) as measures of vascular function**

HPG-GdF-enhancing voxels were further characterized for their plasma volume (fPV) by calculating the magnitude of the rapid signal increase after injection and for their extravascular accumulation (apparent permeability-surface area product, aPS) by measuring the slope of the enhancement curve after the initial increase for the duration of the scan (0-2000 s). The patterns of high and low fPV and aPS were often similar to each other, though there are notable differences. A linear regression analysis comparing fPV with aPS for whole-slice averages yields an  $R^2$  of 0.11, suggesting they are independent of each other. As a detailed example, tumour HT01 has a region of high aPS and low fPV (Figure 2.5(A)), as well as a region exhibiting the opposite, with high fPV and low aPS (Figure 2.5(B)). The corresponding histological section seemed to validate these observations, where the region with high fPV has a greater density of CD31-stained vessels and the region with greater aPS has more HPG-GdF in the extravascular compartment. While histological data enables a detailed view of HPG-GdF accumulation, the actual rate of extravasation may only be determined by the dynamic MR data, as illustrated by the schematic enhancement curve (Figure 2.5(C)). The corresponding  $K^{trans}$  map derived from Gadovist concentrations shows high values in both the high aPS and high fPV regions of this tumour (Figure 2.4, Column 1). Therefore, both fPV and aPS played important roles contributing to overall tumour vascular function, had measurable intra-tumour heterogeneity and produced data that was distinct from and more informative than DCE-MRI derived parameters for Gadovist.

### **2.3.4 Variable vascular function in HCT116 and HT29 human colorectal xenografts**

HPG-GdF accumulated to a greater degree in HT29 colorectal xenografts relative to HCT116, and this was seen at all distances from vessels (Figure 2.6(A)). HCT116 and HT29 colorectal xenografts grow at similar rates in mouse models but exhibit distinct vascular function parameters (data summarized in Table 2.1).

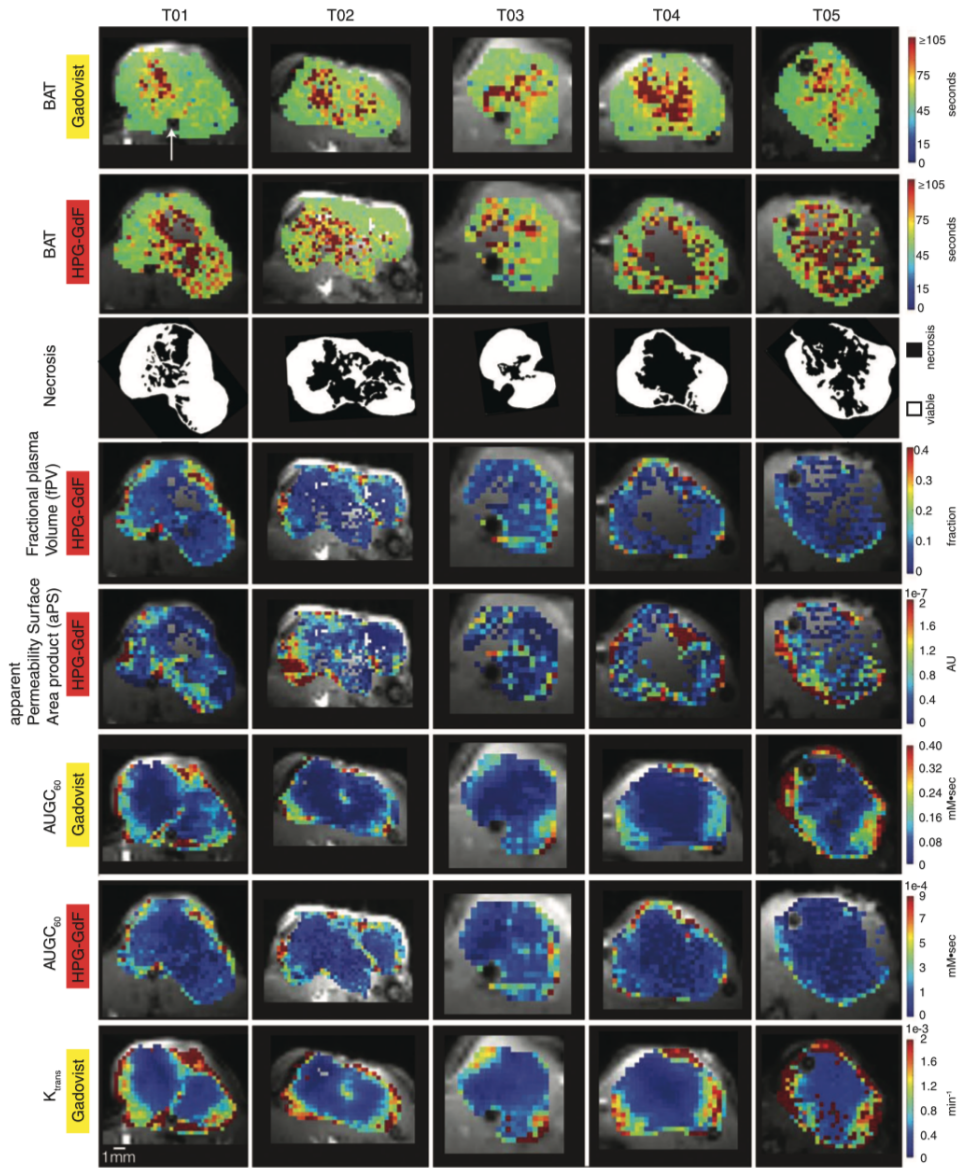


**Figure 2.4:** Individual HT29 tumour (T01-05) slice maps are presented for parameters derived using Gadovist (BAT, AUGC<sub>60</sub>, K<sup>trans</sup>), HPG-GdF (BAT, fPV, aPS, AUGC<sub>60</sub>) and histological imaging of necrosis. Figure reused with permission from Wiley and Sons.

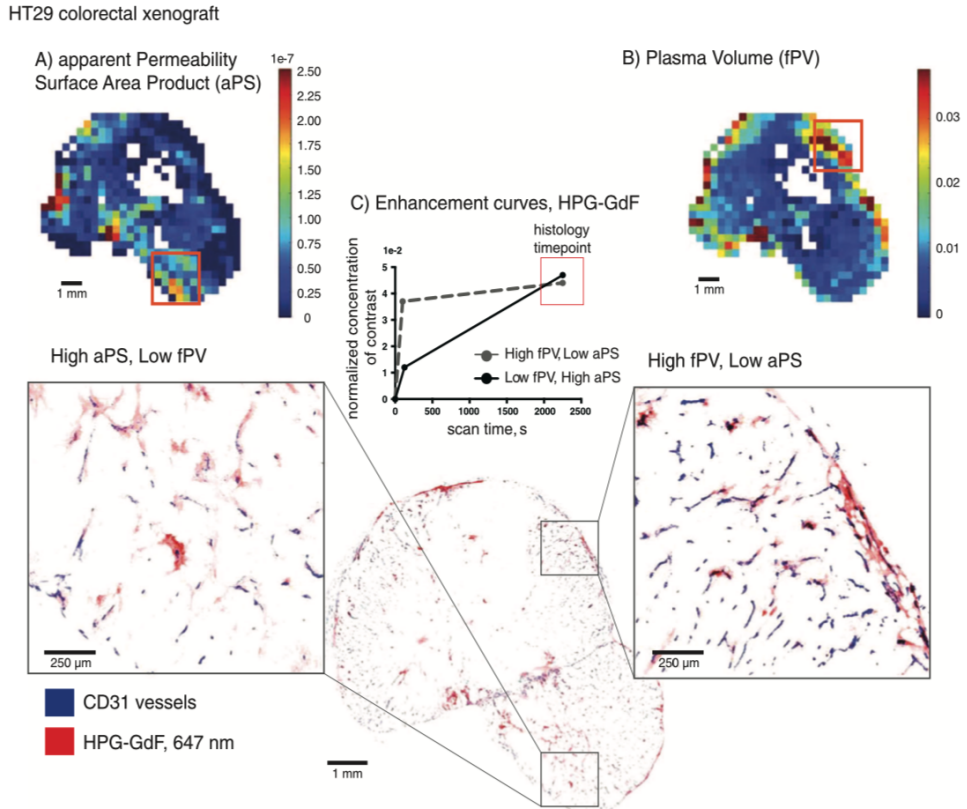


**Figure 2.5:** fPV and aPS parameter maps for an HT29 tumour (T01) are shown with corresponding histological image depicting CD31-stained vessels (blue) and HPG-GdF native fluorescence (red). The high fPV region has notably greater vascular density, and HPG-GdF is clearly seen overlapping with vessels (black) or accumulating in the extravascular space. A region with high aPS that does not correspond to high fPV is magnified (A) and compared with a high fPV region that does not correspond to high aPS (B). Figure reused with permission from Wiley and Sons.

Overall, HT29 tumours possessed a greater density of vessels (CD31 average distance was  $82.3 \pm 3.0 \mu\text{m}$  for HCT116 and  $40.5 \pm 1.5 \mu\text{m}$  for HT29,  $p < 0.05$ ). However many vessels were unlabelled for the fluorescent dye (carbocyanine) used as a histological perfusion marker; the density of perfused vessels was similar between the two xenograft models (CD31 vessels labeled for carbocyanine, PF, was  $47.8 \pm 5.4\%$  for HCT116 and  $36.0 \pm 2.1\%$  for HT29,  $p > 0.05$ ). The density of vessels labeled for HPG-GdF fluorescence was much greater in HT29 tumours (HPG-GdF+ve CD31, average distance was  $172 \pm 10 \mu\text{m}$  for HCT116 and  $88.9 \pm 6.3 \mu\text{m}$ ;  $p < 0.05$ ). In addition to a greater density of HPG-GdF-positive vessels, the high MW contrast agent was able to accumulate to a greater degree in the extra-vascular space around vessels in HT29 cells. This effect can be seen in the histological images of the compared tumour models collected 60-min post HPG-GdF administration (Figure 2.6(B)).

Histological quantity	Units	HCT116	HT29	p-value
CD31 (Average distance)	$\mu\text{m}$	$82.3 \pm 3.0$	$40.5 \pm 1.5$	0.008
Carbocyanine PF positive and CD31 (Average distance)	% $\mu\text{m}$	$47.8 \pm 5.4$ $137 \pm 13$	$36.0 \pm 2.1$ $95.0 \pm 11.5$	0.11
HPG-GdF PF HPG-GdF-positive and CD31 (Average distance)	% $\mu\text{m}$	$19.9 \pm 2.0$ $172 \pm 10$	$23.4 \pm 1.2$ $88.9 \pm 6.3$	0.31 0.008
HPG-GdF (Average intensity)	a.u.	$0.405 \pm 0.031$	$0.828 \pm 0.123$	0.008
Necrosis Fraction	%	$52.4 \pm 3.6$	$37.7 \pm 5.1$	0.032

**Table 2.1:** Summary of the quantitative histological histological data for the HCT116 and HT29 tumours.

### 2.3.5 MRI analysis of HPG-GdF in HCT116 and HT29 xenografts: BAT, fPV and aPS

Administration of neither Gadovist nor HPG-GdF was useful in detecting the difference in vascular function between HCT116 and HT29 tumours using the initial area under the gadolinium concentration curve ( $\text{AUGC}_{60}$ ). The slice-averaged means were not significantly different between tumour groups (data summarized in Tables 2.2 and 2.3). Similarity between models was also observed qualitatively in the parameter maps with  $\text{AUGC}_{60}$  or  $K^{trans}$  overlaid on  $T_1$ -RARE images shown in Figs. 2.4 and 2.7. Both tumour models show higher  $\text{AUGC}_{60}$  values in the tumour margins for both contrast agents.

Gadovist quantity	units	HCT116	HT29	p value
$\text{AUGC}_{60s}$	$\text{mM}\cdot\text{s}$	$5.09 \pm 0.83$	$7.68 \pm 1.66$	0.31
$\text{AUGC}_{37min}$	$\text{mM}\cdot\text{s}$	$317 \pm 23$	$395 \pm 70$	0.56
$v_p$	%	$9.92 \pm 1.87 \times 10^{-3}$	$9.03 \pm 3.27 \times 10^{-3}$	0.42
$v_e$	%	$0.247 \pm 0.024$	$0.246 \pm 0.013$	0.77
$K^{trans}$	$\text{min}^{-1}$	$8.41 \pm 1.56 \times 10^{-4}$	$1.16 \pm 0.039 \times 10^{-3}$	>0.99
$R^2$ (p75)	-	$0.892 \pm .017$	$0.913 \pm .018$	0.31
BAT	seconds	$69.5 \pm 4.2$	$62.7 \pm 2.3$	0.31
BAT-EV	%	$98.9 \pm 0.6$	$99.2 \pm 0.5$	0.63

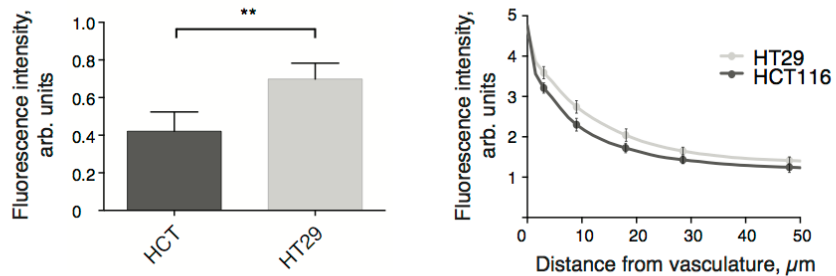
**Table 2.2:** Summary of MRI parameters derived from pharmacokinetic modelling of the Gadovist contrast agent for both the HCT116 and HT29 tumours.

HPG-GdF quantity	units	HCT116	HT29	p value
$\text{IAUC}_{60s}$	$\text{mM}\cdot\text{sec}$	$6.41 \pm 1.71E - 03$	$9.62 \pm 1.64E - 03$	0.15
$\text{AUC}_{37min}$	$\text{mM}\cdot\text{sec}$	$0.384 \pm 0.097$	$0.532 \pm 0.050$	0.31
BAT	seconds	$83.3 \pm 5.0$	$83.6 \pm 7.0$	0.53
BAT-EV	%	$52.2 \pm 4.8$	$81.8 \pm 5.0$	0.016
fPV	fraction	$1.07 \pm 0.33E - 02$	$0.864 \pm 0.27E - 02$	0.22
aPS	$\text{seconds}^{-1}$	$2.38 \pm 1.00E - 08$	$5.81 \pm 1.4E - 08$	0.06

**Table 2.3:** Summary of MRI parameters derived from applying a linear model to the HPG-GdF contrast kinetics for both the HCT116 and HT29 tumours.

However, an MR-measured difference between HCT116 and HT29 vascular

A) HPG-GdF accumulation in HCT116 vs HT29 xenografts at 60min



B) HPG-GdF in HCT116 & HT29 xenografts

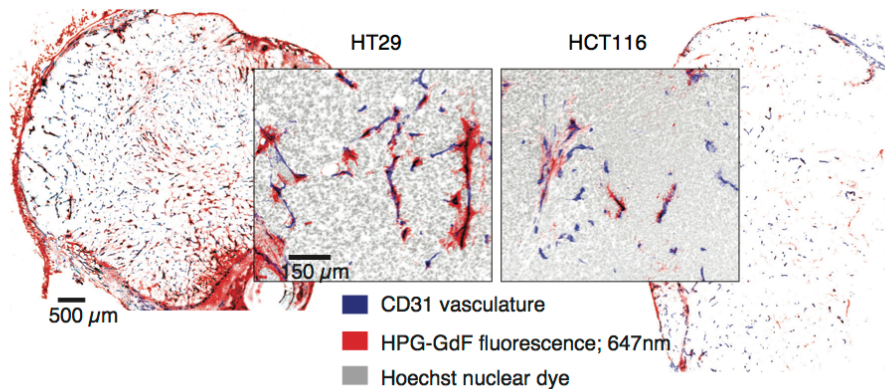


**Figure 2.6:** HPG-GdF distribution in HCT116 and HT29 colorectal tumour xenografts at 60-min: histological analysis. (A) The whole-slice average fluorescence intensity shows that HPG-GdF accumulates to a greater degree and distributes further away from vasculature in HT29 tumours. (B) Sample images show HPG-GdF (red) overlaid on CD31 (blue); insets also display nuclear density (grey). A greater degree of HPG-GdF accumulation can easily be appreciated in the HT29 tumours. Figure reused with permission from Wiley and Sons.

function was seen with the BAT data for HPG-GdF. The fraction of enhancing voxels was significantly lower in the HCT116 relative to the HT29 tumours (BAT-enhancing voxels for HPG-GdF in HCT116 was  $52.2 \pm 4.8\%$  and was  $81.8 \pm 5.0\%$  in HT29,  $p = 0.016$  ) (Table 2.3). This corresponded to the histological data, which also shows HCT116 tumours as having a greater proportion of necrotic tissue (necrosis fraction for HCT116 was  $52.4 \pm 3.6\%$  vs.  $37.7 \pm 5.1\%$  in HT29,  $p = 0.03$ ). Of the HPG-GdF BAT-enhancing voxels, the averaged fPV and aPS parameters were also determined (Table 2.3), and no difference was seen with the plasma volume between tumour models (fractional fPV for HCT116 is  $2.67 \pm 0.33 \times 10^{-4}$  and is  $2.16 \pm 0.27 \times 10^{-4}$  for HT29). aPS of HPG-GdF was the only MR-derived biomarker able to detect the significant difference in vascular function between these two tumour models. Complete data sets for HCT116 tumours are shown in Figure 2.7.

## 2.4 Discussion

The use of MCAs for imaging and describing tumour vascular function is a widely pursued area of research. Many studies have investigated a range of sizes, where smaller molecules extravasate and distribute through tissue too quickly to be considered as sensitive blood pool agents, and larger molecules often accumulate too slowly for adequate signal detection [26, 44, 59]. In this work we describe HPG-GdF as an MR-visible MCA of 583 kDa, for which we have derived useful biomarkers that have sensitivity in measuring vascular function in preclinical studies. The agent HPG-GdF is not intended to be used in patients directly primarily because of differences in human and tumour xenograft vessel morphology, as well as the unknown safety, efficacy, and biocompatibility considerations of the agent in humans. However, despite this HPG-GdF may be very useful in developing drugs and understanding the distribution of existing drugs in preclinical experiments.

While the signal-to-noise ratio (SNR) from HPG-GdF concentration-time curves is not adequate to fit a complex pharmacokinetic model to determine parameters such as  $v_p$ ,  $v_e$  and  $K^{trans}$ , enhancement was measurable in most tumour voxels. The number of Gd chelates on the HPG-GdF is approximately 300 per carrier molecule, which is high relative to many albumin chelates, the most common MCA in pre-

clinical use, which typically have about 20 chelates per carrier [47]. In addition to a greater number of Gd per carrier, the HPG-GdF accumulates in the perivascular space and fails to distribute more than a few micrometers from most vessels within a short DCE imaging timeframe (Figure 2.3). This accumulation could provide a greater concentration for detection of a local, permeable tumour vessel and avoids the risk of conflating this with the distribution and accumulation elsewhere in tumours. These attributes of HPG-GdF may make it more sensitive and more specific than a smaller MCA such as albumin-Gd-DTPA. A minimum DCE imaging time from the presented data would appear to be about 15 min for the analyses described, which is longer than the suggested 5-min ideal for practical clinical utility [48]. It is possible that greater signal could also be obtained by decreasing the time resolution from the 2.24 s used in these studies, since HPG-GdF remains largely intravascular.

HPG-GdF contains the Gd-DOTA complex, which is thermodynamically highly stable and kinetically inert. The dissociation constant for Gd-DOTA ( $\log K = 24.7$ ) is much higher than those for Ca-DOTA ( $\log K = 17.23$ ) or Mg-DOTA ( $\log K = 11.92$ ), hence neither Ca nor Mg can transmetallate Gd from the Gd-DOTA complex [61]. Biodegradation of HPG-GdF is therefore likely minimal, occurring through enzymatic attack of the end group, similar to that seen for polyethylene glycol [62]. However, the long half-life and relatively slow excretion of HPGs through the reticuloendothelial system of the liver suggest that the potential for toxicity should be investigated and monitored. A biodegradable version of HPG has recently been synthesized and might circumvent these potential concerns, and will be a focus in future DCE-MRI studies investigating the use of HPGs as MR-visible MCAs [52].

Limited distribution through the interstitium is also most probably the result of its significant size. We have observed HPG-GdF to be much more restricted in its distribution than is suggested by the diffusion coefficients ( $D_{HPG} = 3.7 \times 10^{-7} \text{ cm}^2 \text{ s}^{-1}$  and  $D_{Gadovist} = 3.6 \times 10^{-6} \text{ cm}^2 \text{ s}^{-1}$ ), as the larger agent reaches only 10-15  $\mu\text{m}$  away from vessels within an hour whereas Gadovist reaches all areas of a tumour. HPG-GdF molecules experience greater obstacles to their movement through the heterogeneous tumour microenvironment due to their size, but also possibly due to steric hindrances, non-specific binding or sequestration [38].

The large size of HPG-GdF is a significant advantage. An approximately exponential increase in sensitivity for detection of permeability has been reported with increasing MCA size (19). If extravasation of HPG-GdF only occurs in vessels that are permeable, and the agent does not distribute through the extravascular space to distances away from vessels, then MR-visible HPG-GdF enhancement suggests the presence of vasculature, and accumulation of the agent over time indicates the local presence of a hyper-permeable vessel.

A typical enhancement curve for HPG-GdF is shown in Figure 2.2. The size of the initial step-like enhancement is interpreted as the fPV, and the slope of signal change for the remaining enhancement is reported as the aPS, reflecting the extravascular accumulation of HPG-GdF (Figure 2.2). These parameters are not correlated with each other, with either value potentially significantly higher or lower than the other in the same voxels (Figure 2.5). A pattern of faster enhancement at the tumour margins is consistent for both contrast agents, and, while Gadovist eventually arrives in all the tissue, including regions of necrosis, many voxels that correspond to necrotic regions fail to enhance with HPG-GdF within the 37-min imaging session. We found that HPG-GdF BAT-enhancing voxels correspond to areas without necrosis: see Figs. 2.4 and 2.7 for parameter maps of all BAT-enhancing voxels compared with histologically validated necrotic regions. Therefore, we identified perfused regions of tumour tissue for further vascular function analysis using the straightforward approach of selecting voxels that had positive BATs for their HPG-GdF enhancement curves. Selection of viable tissue and the exclusion of necrotic tissue is a desirable approach for controlling for inter-tumour heterogeneity, since MRI data is most often described as a whole-tumour average. In the event that different tumours possess variable necrotic burdens, or if the necrotic fraction increases over time with treatment, selective analysis of viable tissue can control for this variability.

Qualitative comparisons of well-matched, whole-slice images from multiple modalities emphasize the utility of screening for BAT-enhancing voxels to select for perfused and viable tissues. Without this information, analysis may be restricted to regions of tissues at the tumour margins where hot spots of vascularization are observed histologically, and tissue is assumed to be viable in the MR image [56, 63]. In the colorectal xenografts examined here, the amount of necrosis

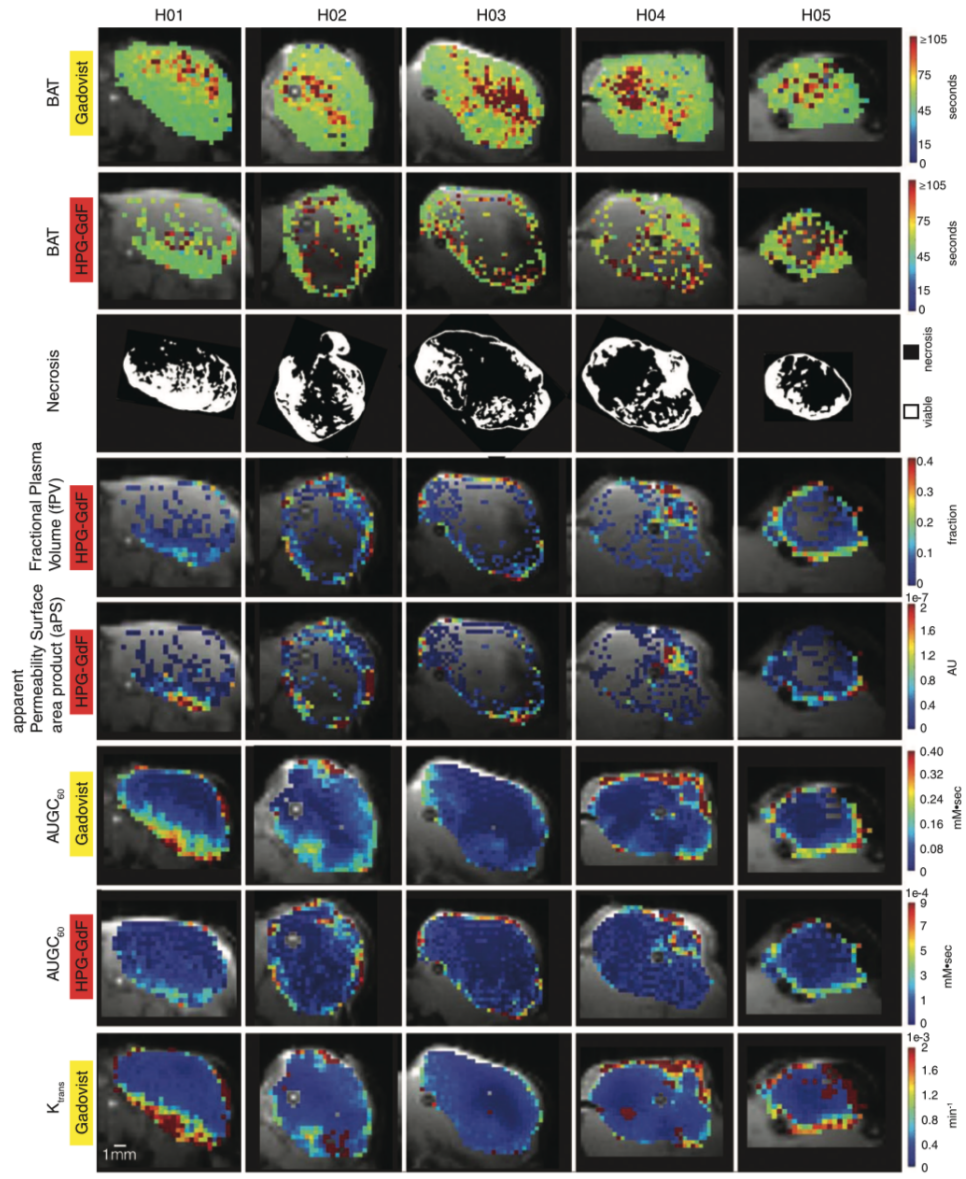


**Figure 2.7:** Vascular function in HCT116 xenografts. Whole-slice maps are presented for individual HCT116 tumours (T01-T05, vertical columns) for parameters derived from MR imaging of Gadovist (BAT, AUGC<sub>60</sub>, K<sub>trans</sub>), MR imaging of HPG-GdF (BAT, fPV, aPS, AUGC<sub>60</sub>) and histological imaging (necrosis). Figure reused with permission from Wiley and Sons.

varied considerably, and while necrosis is typically located more in the core than the tumour margins, there is substantial inter-tumour heterogeneity with respect to the amount and location of necrosis. Notably, while the values for  $K^{trans}$  using Gadovist are on average higher around the entire tumour rim, the fPV and aPS values are more heterogeneously arranged around the rim and within the interior of the tumour. Our more comprehensive approach, validated by observations of viable tissue and perfused vessels within tumour interiors in histological sections, is a significant improvement over selectively assessing limited regions or hotspots for histological or MR quantitative analysis.

Traditional DCE-derived parameters such as AUC and  $K^{trans}$  are composite measures influenced to varying degrees by vascular surface area, permeability and blood flow. Our histological data supports a significant range in the propensity for HPG-GdF to extravasate, suggesting that assumptions of perfusion or permeability-limited conditions are not applicable to all areas of the tumour microenvironment. Hence, we cannot conclude that aPS is exclusively proportional to permeability-surface area (PS) in the whole microenvironment. For example, although the amount of HPG-GdF leaking into the extravascular space is dependent on the vessel being permeable to large molecules, the amount of accumulation, and therefore the amount of signal enhancement, may still be impacted by the concentration of contrast agent within the vessel. Longitudinal gradients can occur locally in permeable vessels as the contrast agent leaks out, despite plasma concentrations remaining consistent in overall systemic circulation [64, 65]. Thus, the aPS is a measure of vascular function that has contributions from permeability as well as, when permeability is very high, perfusion. These limitations in the physiological interpretation of aPS are similar to those that apply to  $K^{trans}$  and AUC for all contrast-enhanced modelling.

Parameters that are based on the amount and proportion of contrast agent enhancement are dependent on fewer assumptions than are pharmacokinetic model-derived parameters such as  $K^{trans}$ . Biophysical signals are dependent on the many variables necessarily involved in obtaining MR images, such as the scanner, imaging sequence, RF coil and analysis techniques. Interpreting magnitudes of change in highly variable tumours may be more reliable than assuming invariable pharmacokinetic attributes or unchanging tumour microenvironments, and may make

simplified biomarkers such as fPV and aPS more applicable to clinical studies conducted across multiple centres [30].

## 2.5 Conclusion

HPG-GdF is a largely intravascular MCA that selectively extravasates from hyperpermeable tumour vessels, accumulating in the perivascular regions without distributing through the tumour interstitium. The high concentration of Gd chelates per carrier molecule in combination with its excellent solubility makes HPG-GdF detection possible despite the relatively low plasma fraction within tumours. By carefully comparing the vessel parameters of small and large molecule contrast agents in the same tumour, as well as comprehensively assessing the location of MCA within the tumour relative to vasculature and necrosis, we conclude that BAT, fPV and aPS biomarkers derived from HPG-GdF enhancement provide a sensitive and specific approach to measuring tumour vascular function. When assessing the significant differences in vascular function of two tumour models (HCT116 and HT29), HPG-GdF was useful in detecting a difference (aPS) while no change was measured with parameters derived from Gadovist. Thus we conclude that HPG-GdF and these analysis techniques are appropriate in the evaluation of tumour angiogenesis and response to treatment for preclinical research.

## **Chapter 3**

# **Applications of HPG-GdF: Investigating distribution of trastuzumab in the tumour microenvironment**

### **3.1 Introduction**

Treatment options for patients with the aggressive HER2-positive form of breast cancer continue to improve, though metastatic breast cancer remains a largely incurable disease. Brain metastases are of particular importance in HER2-positive breast cancer patients. With improved treatments and prolonged survival, the incidence of brain metastases as the first evidence of relapse has increased [66, 67]. This effect has been attributed to the the blood-brain barrier (BBB) creating a sanctuary site by preventing drug access [68, 69]. Antibody-based therapeutics such as trastuzumab are proposed to have difficulty crossing the BBB and therefore brain metastases evade drug activity [66, 70, 71]. In addition to the BBB, specific characteristics of the tumour microenvironment, beginning with a relative paucity of functional vessels, can thwart the access of drugs to their targets such that a population of under-exposed cells may survive and repopulate the tumour [38]. Our

collaborators have shown that many small molecule cytotoxics have limited tumour tissue penetration in both *in-vitro* and *in-vivo* model systems due to difficulties with drug supply, flux through tissue, consumption or sequestration by cancer cells close to blood vessels [59, 72–75].

Macromolecular compounds such as MAb face particular extravascular distribution difficulties due to their high molecular weights and target-binding affinity [41, 76]. The relatively slow distribution of MAbs has been attributed to the binding site barrier hypothesis, where in the case of high affinity binding of the MAb to antigen, MAb distribution is limited by its binding in the presence of ample antigen [77]. Data from our collaborators' lab (Dr. Andrew Minchinton) in the vector over-expressed MDA-435-LCC6 HER2 model showed that despite the ability of trastuzumab to distribute far from vessels in tumours with relatively even HER2 distribution, there persisted HER2-positive tissue with poor access to trastuzumab after peak plasma exposures [78]. Staining heterogeneity is very striking at the vessel level, as trastuzumab is able to extravasate from only a subpopulation of perfused vessels. Other groups have also demonstrated a limitation on the accumulation of trastuzumab in tumours, focusing on net tumour accumulation [41, 76, 79].

The ability of a drug to access and affect all its target cells is intuitively crucial for treatment success. The relatively slow distribution of MAbs through the interstitium in solid tumours is recognized, but the long half-life of MAbs and prolonged plasma exposure is expected to ensure adequate time to access all the tissues in most treatment scenarios. However, we have found that in addition to distributing slowly, MAbs experience additional barriers, leaving some areas of tissue with inadequate drug exposure. The aim for this study was to use HER2-positive tumour and metastases models of cancer to determine potential limits to trastuzumab access that may represent a mechanism of resistance to targeted therapies.

## **3.2 Methods**

### **3.2.1 Reagents**

Trastuzumab and bevacizumab (Roche, Genentech) were provided by the British Columbia Cancer Agency pharmacy; dilutions to 1-2 mg/ml were prepared in sterile 0.9% NaCl before intra-peritoneal (i.p.) injection. Trastuzumab antibodies for use in combination with bevacizumab were tagged with fluorescent labels according to Alexa Fluor 546 Protein Labeling Kit (ThermoFisher) instructions. Hypoxia marker pimonidazole (Hypoxyprobe) was administered at 60 mg/kg as an i.p. injection 2 h prior to tissue harvest. Fluorescent dye DiOC<sub>7</sub>(3) (Molecular Probes), 0.6 mg/ml dissolved in 75% (v/v) dimethyl sulfoxide/25% sterile H<sub>2</sub>O, was administered intravenously as a marker of vessel perfusion 5-min prior to tissue harvest [80].

### **3.2.2 Mice and tumours**

Female NOD-SCID mice weighing 20-28 g between 8 and 16 weeks of age were bred and maintained in our institutional pathogen free animal facility. Mice were implanted with 60 day 17- $\beta$ -estradiol pellets (Innovative Research of America) subcutaneously 3 days before implantation of BT474 or MDA-MB-361 tumours. Tumors were implanted as single cell suspensions ( $2-10 \times 10^6$  cells) into the subcutaneous sacral region or into the inguinal mammary fat pads. Metastases models were implanted as single cell suspensions ( $2-5 \times 10^5$  cells per implant) as i.v. or i.p. injections for SKOV3 or BT474 models, or as intra-cardiac injection for MDA-MDA-MB-231-BR-HER2 models, with animals euthanized a maximum of 23 days after implant.

### **3.2.3 MRI**

MRI experiments were performed at the UBC MRI Research Centre on a 7T Bruker Biospec 70/30 scanner at room temperature with a combination volume (transmit)/surface (receive) coil. DCE-MRI data was collected as previously described [1]. Gadovist (Bayer Healthcare) was administered by i.v. catheter as a 5  $\mu$ L/g bolus dose from 60 mM solution. Macromolecular contrast agent hyper-

branched polyglycerol (HPG-GdF, 583 kDa) was synthesized as previously described [6, 49] and administered as a  $6 \mu\text{L/g}$  bolus dose from 100 mg/mL (0.2 mM). Regions of interest (ROI) were drawn on  $T_2$ -weighted RARE images to outline the tumour using ImageJ (NIH) and all other MR analysis was performed using Python. Area Under the Curves (AUC) for Gadovist was determined from the common injection time point to 60 s. A two-parameter linear model was applied to characterize HPG-GdF signal-intensity curves for fractional plasma volume (fPV) determined by the rapid increase at time of injection and for apparent permeability surface area product (aPS) calculated as the slope of later enhancement, as described earlier in section 2.2. Both MR and histological modalities imaged slices in the plane perpendicular to an implanted fiducial marker tube to minimize angular differences between MR and histological image slices [35].

### 3.2.4 Immunohistochemistry

The general immunohistochemical procedure used has been previously reported [78]. Briefly,  $10 \mu\text{m}$  tumour cryosections were air-dried, imaged for native DiOC7(3) or Alexa 546-tagged trastuzumab fluorescence, and fixed in 50% (v/v) acetone/methanol for 10-min at room temperature. Trastuzumab was visualized in sections using Alexa 546 goat anti-human secondary antibody (Invitrogen) HER2 was subsequently stained with  $2.2 \times 10^{-3} \text{ mg/mL}$  trastuzumab as a primary detection antibody and goat anti-human Alexa 546 secondary. Additional staining was performed using antibodies to PECAM/CD31 (BD PharMingen), pimonidazole (hypoxprobe) collagen IV (CIV, Gene Tex) and  $\alpha$ SMA (Abcam). Visualization of primary detection antibodies was done using Alexa fluorescence secondary antibodies of appropriate species using 488 nm, 647 nm and 750 nm wavelengths. Nuclear density was stained using Hoechst 33342 (Thermofisher) and imaged at 380 nm.

### 3.2.5 Image acquisition and analysis

Sections were imaged as previously described [59] using a system of tiling adjacent microscope fields of view at a resolution of  $0.75 \mu\text{m}/\text{pixel}$ . Using ImageJ [60] and user-supplied algorithms, images were superimposed and manually cropped to tu-

mour tissue boundaries with staining artifacts and necrosis removed. False colour images were constructed in ImageJ by converting greyscale images to colour and overlaying selected layers: trastuzumab (magenta), HER2 (blue or grey), Hoechst 33342 (grey), CD31 (blue), carbocyanine (cyan), pimonidazole (green) and  $\alpha$ SMA or CIV (red). Positive fluorescent staining is reported as average intensity (range 1-255) for pimonidazole, trastuzumab and HER2. Perfused vascular density was determined by applying a threshold to CD31 and DiOC7(3) images, with neighboring positive pixels grouped as “objects”; CD31 objects with a minimum 20% overlap with DiOC7(3) objects were determined to be perfused vessels. All image pixels were sorted based on their nearest perfused vessel and the average distance is reported as a repeatable measure of vascular density.

### 3.3 Results

#### 3.3.1 Measures of vascular density, architecture and function do not consistently correlate with heterogeneous patterns of trastuzumab distribution

Significant inter-vessel heterogeneity in trastuzumab distribution is seen in orthotopic BT474 xenografts, with neighbouring patent vessels often showing variable amounts of trastuzumab bound to perivascular cells (Figure 3.1A), similar to previous findings in MDA-435-LCC6 vector-overexpressing HER2-positive tumours [78]. Non-patent vessels (red arrows in Figure 3.1A) never have extravascular trastuzumab, suggesting intermittent perfusion is not a significant mechanism for reduced trastuzumab access. The same inter-vessel heterogeneity is seen in MDA-MB-361 tumours where vascular function dynamics were further characterized by imaging the presence of Gadovist (Figure 3.1B). Regions with greatest vascular function (largest AUC<sub>60</sub> with Gadovist) do not consistently correspond to areas of greater trastuzumab distribution (red arrows in Figure 3.1B); this is also demonstrated quantitatively where matched slices were plotted for amount of bound trastuzumab and AUC<sub>60</sub> (Gadovist). The same sections were stained for vascular architectural markers  $\alpha$ SMA and CIV (both shown in red), neither of which exhibit a pattern of distribution similar to the presence or absence of trastuzumab

(Figure 3.1B).

Some regions are high for Gadovist uptake, reflecting high vascular function, but these do not consistently correspond with regions of high trastuzumab distribution in histology sections. No correlation was found between Gadovist AUC and trastuzumab in matched image slices obtained from multiple tumours. Similarly, neither  $\alpha$ SMA nor CIV are present to a greater degree proximal to vessels with or without trastuzumab bound to perivascular cells.

### **3.3.2 Dynamic vascular permeability and blood volume measurements do not consistently relate to patterns of trastuzumab distribution**

The histological measure of perfusion using carbocyanine is a useful indication of vessel patency, however it is static and therefore its interpretation is limited. The role of vascular function on trastuzumab distribution was further investigated using dynamic contrast-enhanced MRI (DCE-MRI) of a high molecular weight contrast agent, HPG-GdF (MW 583 kDa) (Figure 3.2). As previously described, repeat imaging of contrast agent presence in the tumours is analysed and the initial appearance of HPG-GdF reflects fPV and its accumulation over time indicates the apparent permeability surface area (aPS) [1]. Tumours were excised immediately after imaging; corresponding histological sections are compared to the DCE-MRI derived parameter maps. BT474 tumours have microregionally variable levels of both fPV and aPS, each exhibiting regions of distinction. Regions of high fPV are well matched by histological images of carbocyanine that indicate areas of very high perfusion but some of these regions do not have any significant accumulation of trastuzumab. The reverse can also be found, where regions with relatively low fPV correspond to high trastuzumab. Similarly, there are some significant trastuzumab accumulation areas that have relatively low aPS while some high aPS values correspond to areas with relatively low trastuzumab. Examples of good or bad correlation between vascular function and trastuzumab distribution are highlighted with arrows and suggest that neither of the MRI-derived parameters consistently or adequately explain microregional distribution of trastuzumab.

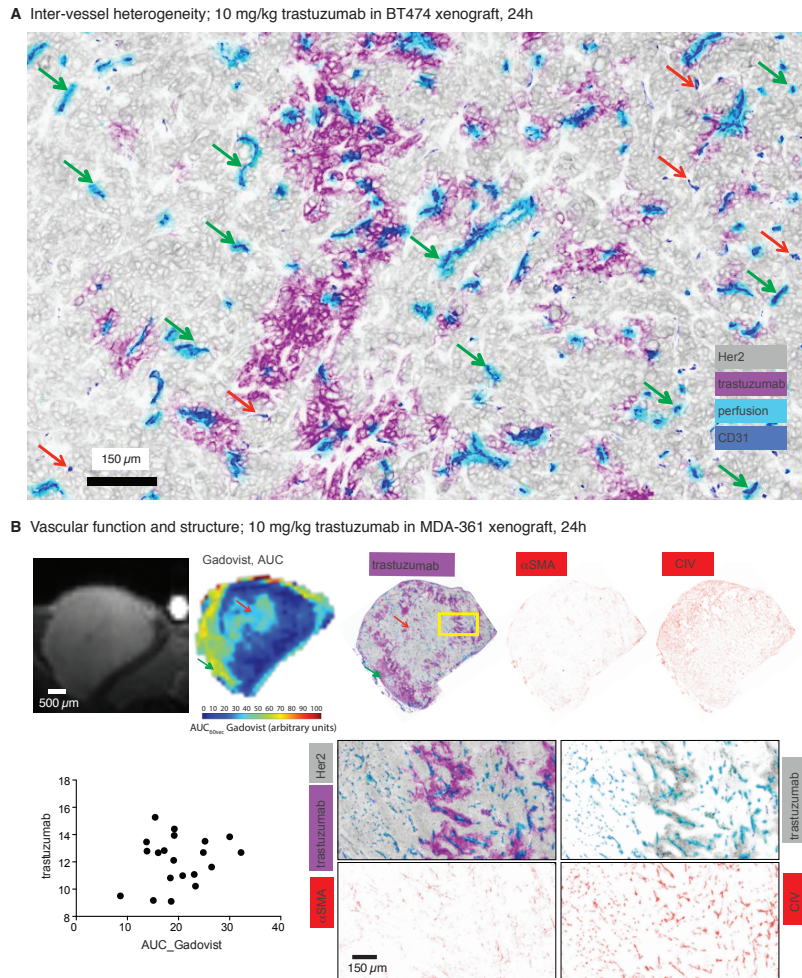


**Figure 3.1:** A) Magnified region of a BT474 xenograft treated with 10 mg/kg trastuzumab for 24 h. Carbocyanine fluorescent dye (cyan) around CD31 stained vessels (blue) indicates patency; non-patent vessels are indicated as red arrows. Trastuzumab extravasates from vessels heterogeneously, with many patent vessels showing no extravascular bound trastuzumab (green arrows) even when adjacent patent vessels do have perivascular trastuzumab. B) An anatomical RARE MR image with the tumour is shown alongside an AUC<sub>60</sub> map using Gadovist in MDA-MB-361 tumours. The AUC<sub>60</sub> map is compared with slice-matched histology sections of bound trastuzumab (purple), vascular architectural markers  $\alpha$ SMA and CIV (both shown in red).

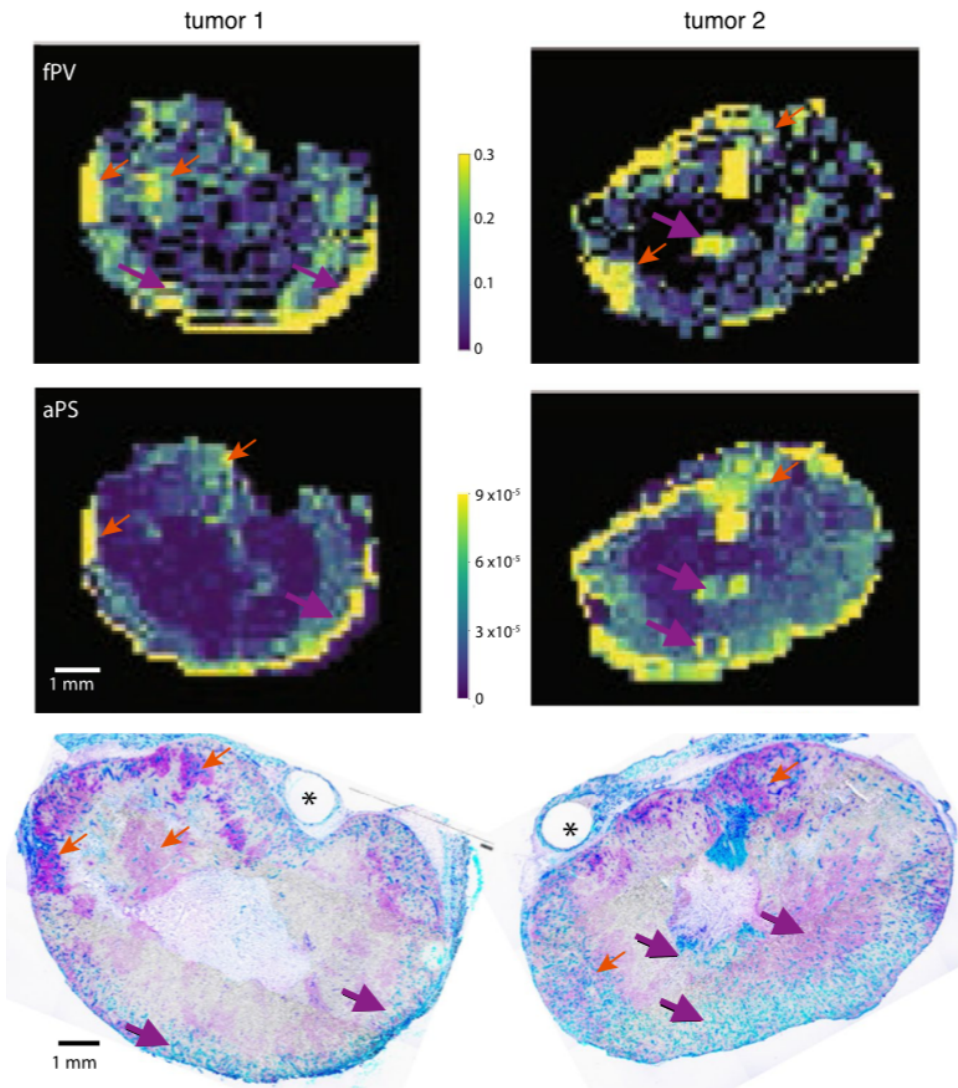


**Figure 3.2:** fPV and aPS parameter maps are compared to matched histology sections stained for bound trastuzumab (magenta), and for HER2 (grey), carbocyanine marker of perfusion (cyan) and for CD31 vasculature (blue). Areas of vascular function (MRI) and trastuzumab (histology) correlation are indicated (orange arrows) in both modalities; example areas of poor matching are also shown (purple arrows). Stars indicate location of fiducial markers for multi-modal slice comparison.

### 3.4 Discussion

Using tumour mapping analysis and DCE-MRI we examined the impacts of tumour blood vessel architecture, vascular function and the tumour microenvironment on the patterns of distribution of trastuzumab in primary and metastatic models. Our collaborators have observed that even when trastuzumab does have access to tumour tissues, the pattern of distribution is highly heterogeneous, similar to their previous work in a vector-overexpressing HER2-positive breast cancer model [78]. Other groups demonstrating a limitation on the accumulation of trastuzumab in preclinical tumours have focused on net tumour accumulation and suggest that a major limitation to MAb distribution is their difficulty distributing through the solid tumour tissue in the extravascular space [41, 76, 79]. In humans, MAbs have a long half-life and are administered for many months. The pharmacokinetic parameters of MAbs are therefore thought to likely accommodate relatively slow distribution of MAbs through the interstitium [41, 81]. However, 3D tissue-disc data from the Minchinton lab shows trastuzumab is able to diffuse relatively well through tumour tissues *in vivo* in conditions of poor convective flow similar to an environment with high interstitial fluid pressure *in vivo* [2]. Neither is trastuzumab distribution limited by tight binding to antigen proximal to vessels as suggested by the binding-site barrier hypothesis [77], as it reaches distances  $> 150\mu\text{m}$  from sources within 24h despite high HER2 expression [2]. This distance is similar to the diffusion limit for oxygen, therefore most tumour tissues are within this  $150\mu\text{m}$  range of a blood vessel and could be expected to have adequate exposure. These data suggest that neither the binding site barrier hypothesis nor high interstitial fluid pressure adequately explain microregional variation in trastuzumab binding. Given the incomplete access of trastuzumab seen in our models, other vessel- and tissue-level barriers appear to limit its distribution in the tumour microenvironment.

Vascular maturity and architecture has also been attributed to poor drug access [82], however, no correlation between markers for  $\alpha\text{SMA}$  or CIV and the relative distribution of trastuzumab has been found. Higher doses and longer exposures do lead to higher numbers of vessels with perivascular trastuzumab, suggesting that some degree of intermittent perfusion or very poorly permeable vessels impact the observed microregional heterogeneity. Non-perfused vessels have not

been observed to have trastuzumab on perivascular cells, which suggests intermittent perfusion is an unlikely mechanism for observed inter-vessel heterogeneity. Dynamic measurements of perfusion and permeability derived from DCE-MR imaging of high molecular weight contrast agent HPG-GdF (583 kDa) suggest the intuitive relationship between vascular function and drug access is important, but does not consistently explain the heterogeneous patterns of drug distribution seen. Areas of highly perfused tissue marked by carbocyanine in histological sections correspond to areas of high perfusion and/or permeability in MRI. However, these tumour areas of high vascular function described in both imaging modalities may or may not have bound trastuzumab. Similarly, regions with substantial amounts of bound trastuzumab do not necessarily correspond to areas of high perfusion or permeability measured using aPS and fPV. HPG-GdF-derived parameters fPV and aPS arise under conditions that are closer to a permeability-limited regime than standard low-molecular weight contrast agents. However, in the highly chaotic vascular environment of tumours we can still expect these MR-derived parameters of vascular function to not be completely independent of each other.

New strategies that are able to more effectively target and kill cancer cells, particularly metastatic disease, are urgently required. Efforts to vary antigen-binding affinities and the size of MAb fragments have been explored to improve their distribution through the extravascular compartment [41, 76]. Our data highlight the importance of also considering access of antibodies to target tumour tissues and whether microregional distribution of MAb therapeutics may be affected when combined with vascular damaging agents or when targeting occult metastases. Improvements to MAb anti-cancer activity could be made in selection of combination therapies and the design of treatment schedules, as well as in the design of novel targeted drugs. Efforts to examine these phenomena in the clinic would be of significant interest.

### 3.5 Conclusions

In this chapter we showed evidence for poor distribution and access of trastuzumab in preclinical tumours through direct visualization of bound drug, with particular implications for metastatic tumours. DCE-MRI imaging parameters such

as vascular permeability and fractional plasma volume do not relate to patterns of trastuzumab distribution. Similarly, no correlations were found between trastuzumab distribution and histological metrics such as vascular density and function or vascular architectural markers  $\alpha$ SMA and CIV. This suggests that the tumour microenvironment and tissue- and vessel-level barriers to drug distribution could effectively limit access of the drug to all its target cells. These effects appear to be more important than slow interstitial distribution resulting from high interstitial fluid pressures or high binding affinity to HER2. The non-invasive imaging techniques to probe the tumour microenvironment described here could also be applied to investigate the distribution of other drugs.

## **Chapter 4**

# **Applications of HPG-GdF: Assessing vascular normalization using an antiangiogenic chemotherapy**

### **4.1 Introduction**

In the previous chapter we used HPG-GdF to help shed some light on the distribution of Trastuzumab within a tumour. Though we were unable to use measures of vascular function to explain its distribution, we did show that vessel permeability and plasma volume did not consistently relate to drug distribution. In this chapter we aim to use parameters from DCE-MRI using HPG-GdF to probe vascular function after treatment of SCCVII tumour xenografts with bevacizumab, an antiangiogenic drug that normalizes the tumour vasculature by inhibiting VEGF.

Through various signalling pathways, cancerous cells within tumours co-opt host vessels to obtain nutrients for rapid growth and creation of new blood vessels (angiogenesis) [29]. As the tumour expands a new vascular network is formed but is structurally and functionally abnormal on account of leaky and tortuous blood vessels [16], absent or loosely attached pericytes that provide structural sup-

port for cells, and abnormal morphology of the endothelial cells lining the vessels. Aberrant angiogenesis, poor blood perfusion, and a chaotic vascular network all play a role to limit oxygen delivery to cells, contribute to acidosis and formation of hypoxic regions in tumours [29]. Hypoxic regions within tumours are extremely problematic as those cells are resistant to both radiation and many cytotoxic chemotherapies. Additionally, the resulting tumour microenvironment poses strong barriers to effective drug delivery and consequently, efficacy.

A strategy to mitigate such adverse conditions of drug delivery is to attempt to normalize the vascular network by pruning away newly formed vessels, limiting creation of new vessels, and ultimately, spreading out the same amount of nutrients over fewer vessels. As the structural components of the vasculature improve through reduced vessel leakiness and increased network organization, delivery of chemotherapies is more efficient [39]. This effect has been termed ‘Vascular Normalization’ and does not just rely upon increased uptake of drugs and oxygen but also on improving the delivery of the drugs to a larger population of the tumour [29]. Considerable evidence has been presented in the literature in support of the vascular normalization window [29, 83, 84]. MRI techniques such as dynamic susceptibility contrast MRI, arterial spin labeling, and DCE-MRI have all been used to obtain surrogate parameters of the effects of vascular normalization. Unfortunately, modelling of the kinetics of low molecular gadolinium-based agents often makes it difficult to separate blood vessel permeability and capillary surface area without resorting to more complex models such as the two compartment exchange model, extremely fast temporal resolution, and accurate knowledge of the arterial input function. This limitation motivated this work to determine whether a high molecular weight agent such as HPG-GdF could be used for measuring vessel permeability without the confounding effects of blood flow.

The binding of vascular endothelial growth factors (VEGF) to the VEGF receptor is a key driver of angiogenesis. Bevacizumab - marketed clinically as ‘Avastin<sup>®</sup>’ - is a monoclonal antibody that binds VEGF extracellularly, preventing the interaction of the VEGF molecule with its receptors and inhibits angiogenesis. Amongst others, bevacizumab has been used clinically to treat breast, colon, colorectal, lung, brain, ovarian and cervical cancers [85]. VEGF ablation has been shown to at least temporarily reduce vascular permeability and increase tumour

oxygenation in some models [30]. We hypothesized that treatment with a VEGF inhibitor will result in a decrease of vessel permeability measured with DCE-MRI using HPG-GdF.

## 4.2 Methods

### 4.2.1 Mice tumours, and treatment groups

Twelve female NOD-SCID mice were implanted with murine squamous cell carcinoma SCCVII tumours ( $5 \times 10^5$  cells in 50  $\mu\text{l}$  serum-free media; cells provided by Dr. J Evans). Mice were imaged when the largest tumour diameters reached a volume of approximately 500  $\text{mm}^3$ , positioned supine on the custom surface coil apparatus and anaesthetized with isoflurane for the duration of imaging sessions until euthanasia.

The treated group comprised six of the twelve animals and were administered 5mg/kg mouse anti-VEGF antibody (B20-4.1.1., Genentech) 72 hours prior to the imaging session. Throughout the imaging session, a small animal monitoring system (SA Instruments Inc., Stony Brook, NY, USA) was used to monitor respiration rate and body temperature. A continuous airflow heater was used to maintain temperature at  $36.5 \pm 1^\circ\text{C}$ . All animals were injected with 60 mg/kg pimonidazole hydrochloride (HypoxyProbe) i.p. 60 minutes prior to imaging to label hypoxic cells and were euthanized within 15-min of imaging completion. Tumours were embedded and frozen in optimum cutting temperature medium (OCT; Tissue-TEK).

### 4.2.2 MRI

MRI experiments were performed at the UBC MRI Research Centre on a 7T Bruker Biospec 70/30 scanner at room temperature with a combination volume (transmit)/surface (receive) coil. Macromolecular contrast agent hyperbranched polyglycerol HPG-GdF, 500 kDa) was synthesized as previously described [6, 50] and administered as a 6  $\mu\text{L/g}$  bolus dose from 100 mg/mL (0.2 mM). DCE-MRI data was collected at a time resolution of 4.27 s (FLASH; TR/TE = 66.7/2.67s; FA =  $40^\circ$ , NR = 250). The matrix size was 128 x 64 x 6 with a field-of-view of 38.4 x 19.2 x 6 mm, resulting in an in-plane spatial resolution of 0.3 x 0.3 mm and a

slice-thickness of 1 mm. Regions of interest (ROI) were drawn on T2-weighted RARE images to outline the tumour using ImageJ (NIH, Maryland, USA) and all other MR analysis was performed using Python. A two-parameter linear model was applied to characterize HPG-GdF signal-intensity curves for fPV determined by the rapid increase at time of injection and for aPS calculated as the slope of later enhancement similar to what was described in section 2.2. Area Under the Curve (AUC) for HPG-GdF was determined using the signal intensity curves from the injection time point to 60s. Non-enhancing voxels (i.e. those with an  $AUC_{60} < 0$ ) were excluded from all analyses. Both MR and histological modalities imaged slices in the plane perpendicular to an implanted fiducial marker tube to minimize angular differences between MR and histological image slices [35].

#### 4.2.3 Immunohistochemistry

Frozen and OCT-embedded tumours were cryosectioned into  $10\mu\text{m}$ -thick slices and air-dried. Sections were first imaged for native DiOC7(3) or Alexa 647nm-tagged HPG-GdF fluorescence, and fixed in 50% (v/v) acetone/methanol for 10 minutes at room temperature. Additional staining was performed using antibodies to PECAM/CD31 (BD PharMingen) and pimonidazole (hypoxprobe). Visualization of primary detection antibodies was done using Alexa fluorescence secondary antibodies of appropriate species using 488 nm and 546 nm wavelengths. Nuclear density was stained using Hoechst 33342 (Thermofisher) and imaged at 380 nm.

#### 4.2.4 Image acquisition and analysis

Sections were imaged using a system of tiling adjacent microscope fields of view at a resolution of  $0.75 \mu\text{m}/\text{pixel}$  [59]. Using ImageJ [60] and user-supplied algorithms, images were superimposed and manually cropped to tumour tissue boundaries with staining artifacts and necrosis removed. False color images were constructed in ImageJ by converting greyscale images to color and overlaying selected layers: HPG-GdF (red), Hoechst 33342 (grey), CD31 (blue), carbocyanine (cyan), pimonidazole (green). Positive fluorescent staining for each slice is reported as a mean, and the median group intensity  $I$  (range 0-255) is reported for pimonidazole ( $I_{pimo}$ ), HPG-GdF ( $I_{hpg}$ ).

## 4.3 Results

### 4.3.1 Treatment with B20 reduces tumour hypoxia and HPG-GdF 72 hours after treatment

Treatment with the VEGF inhibiting drug B20 resulted in a dramatic reduction in hypoxia in SCCVII tumour xenografts. Immunohistological staining with pimonidazole allowed for visualization of these group differences with a representative example shown in Figure 4.1. In the untreated group, large regions of the tumours are hypoxic though there is considerable heterogeneity in baseline hypoxia status between tumours and between slices of the same tumour. In the treated group, pimonidazole staining is disparate and not concentrated in local regions of poor oxygenation. Treated tumours also had relatively lower levels of bound pimonidazole and this was consistent across tumours and between slices of the same tumour. These staining patterns are representative, but there is considerably more heterogeneity in pimonidazole staining in the control tumours.

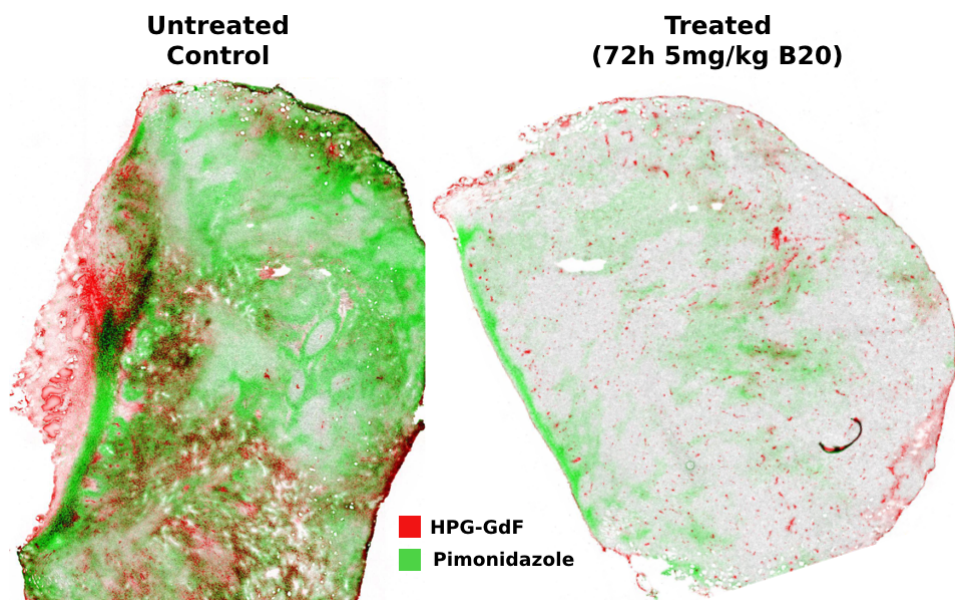


**Figure 4.1:** Histological sections of a control (left) and treated tumour (right) are shown to illustrate the dramatic decreases both in pimonidazole staining and in accumulation of HPG-GdF in the treatment group.

Quantitative analysis of the immunohistological stains in the images was conducted to assess whether these observations existed at the group level. A Mann-Whitney  $U$  test indicated that the median pimonidazole staining intensity was greater for the control group ( $I_{pimo} = 21.7$ ) than the treated group ( $I_{pimo} = 17.2$ ),  $U = 47$ ,  $p = 5 \times 10^{-5}$ . Median HPG-GdF staining intensity is also reduced for the treated tumours ( $I_{hpg} = 12.7$ ) compared to the controls ( $I_{hpg} = 11.0$ ), Mann-Whitney  $U = 52$ ,  $p = 8 \times 10^{-6}$ . Data for individual tumours as well as the group differences are shown in Figure 4.2.

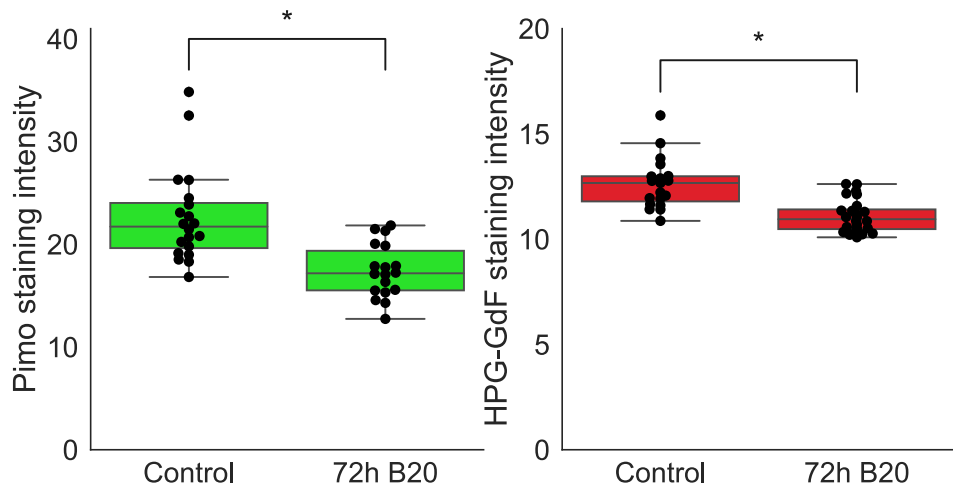


**Figure 4.2:** Median pimonidazole staining is markedly reduced for the B20-treated group ( $I_{pimo} = 17.2$ ) compared to the controls ( $I_{pimo} = 21.7$ ). Median HPG-GdF staining intensity is also reduced for the treated tumours ( $I_{hpg} = 12.7$ ) compared to the controls ( $I_{hpg} = 11.0$ ). P-values from the Mann-Whitney  $U$  test were  $p = 5 \times 10^{-5}$  (pimo, left) and  $p = 8 \times 10^{-6}$  (HPG-GdF fluorescence, right).

### 4.3.2 Blood vessel permeability (aPS) and HPG-GdF accumulation (fluorescence intensity) decreases in tumours treated with B20

Apparent permeability-surface area product (aPS) is a parameter that captures vessel leakiness with DCE-MRI using the large molecular weight contrast agent HPG-GdF. Figure 4.4 shows the group differences and the median value of the B20-treated group ( $aPS_{Md} = 1 \times 10^{-4}$ ) was significantly lower than the control

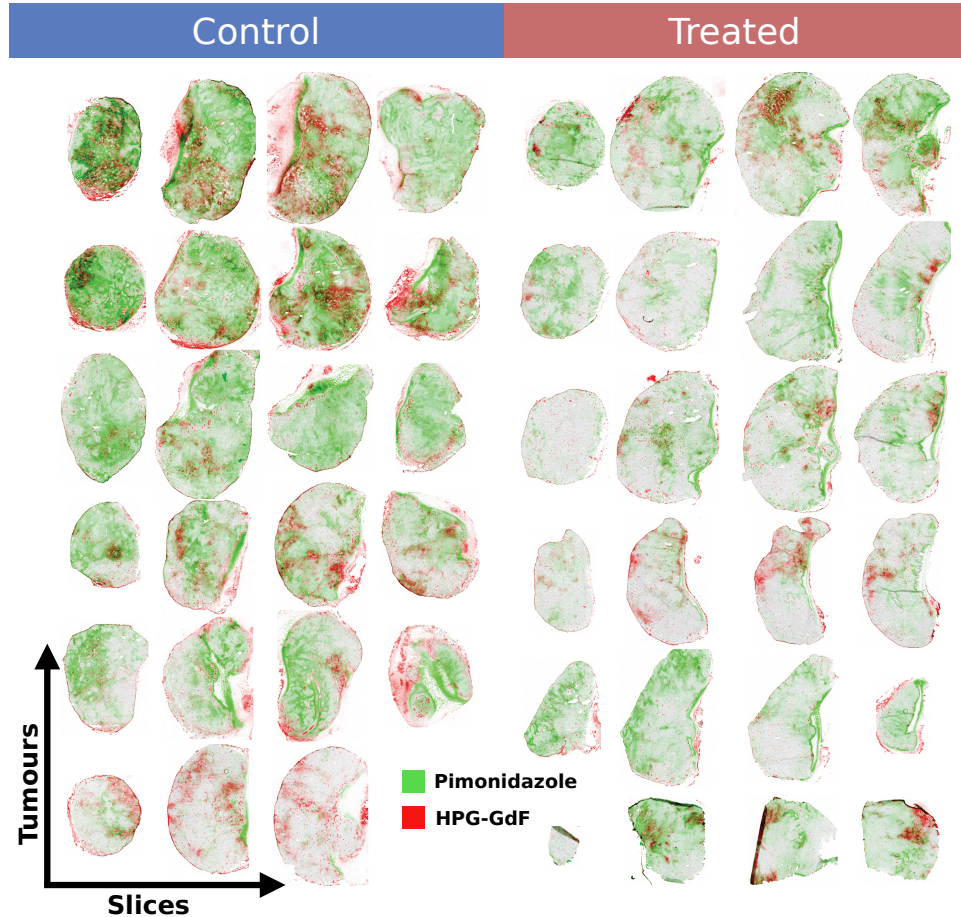


**Figure 4.3:** Histological sections shown for 6 control and 6 treated tumours, with four slices per tumour. All sections are stained for pimonidazole (green) and HPG-GdF (red).

group ( $aPS_{Md} = 6.5 \times 10^{-5}$ ); Mann-Whitney  $U = 3, p = 0.01$ .

Histological staining of HPG-GdF fluorescence matched relatively well with areas of high aPS values as shown in Figure 4.5, however there are also areas where aPS is moderate or high but HPG-GdF fluorescence is not present in high concentrations. Group differences in HPG-GdF accumulation were also present histologically as HPG-GdF fluorescence intensity was markedly decreased in the B20-treated tumours ( $I_{hpg} = 12.7$ ) compared to the controls ( $I_{hpg} = 11.0$ ); a Mann-

Whitney  $U$  test indicated the difference was significant,  $U = 52$ ,  $p = 9 \times 10^{-6}$ . Aggregate voxel distributions of aPS values in Figure 4.2 also shows a clear reduction in aPS in the treatment group. Figure 4.5 shows the aPS parametric maps from DCE-MRI alongside approximate slice matched histology sections from the same tumours. Patterns observed in the quantitative analysis of the data are also evident in MRI and histology images: following treatment with B20, there is a marked reduction in blood vessel permeability measured by aPS and a reduction in HPG-GdF accumulation histologically measured by native fluorescence of the contrast agent.

#### 4.3.3 HPG-GdF enhancement curves and $AUC_{60}$ are altered after treatment, but fPV does not change

Group HPG-GdF enhancement curves are shown in Figure 4.5 and match the results obtained from a quantitative analysis of the parameteric maps: treated tumours have a relatively flat profile and plateau whereas the control tumours show a steady increase of enhancement arising from the leakage of HPG-GdF.  $AUC_{60}$  is a parameter that captures the relative enhancement of voxels within the first 60 seconds after injection. The control tumours had a median  $AUC_{60-Md} = 5.5$  and treated tumours had a median  $AUC_{60-Md} = 4.0$  and the reduction was statistically significant (Mann-Whitney  $U = 6$ ,  $p = 0.03$ ). The fPV values for the control ( $fPV_{Md} = 0.12$ ) and treated tumours ( $fPV_{Md} = 0.09$ ) were not significantly different (Mann-Whitney  $U = 3$ ,  $p = 0.15$ ).

### 4.4 Discussion

In this study we have demonstrated that vessel permeability can be assessed using the apparent permeability-surface area product, aPS. This is consistent with similar reports of extracting permeability parameters with DCE-MRI using albumin-based macromolecular contrast agents [57, 86], dendrimer-based contrast agents [87] and others [48]. Typically, contrast agents used in DCE-MRI are less than 1 kDa in molecular weight and freely extravasate from vessels and enhance surrounding tissues. These low molecular weight agents are essential for many applications including cancer detection, evaluating vascular characteristics, and measuring tu-

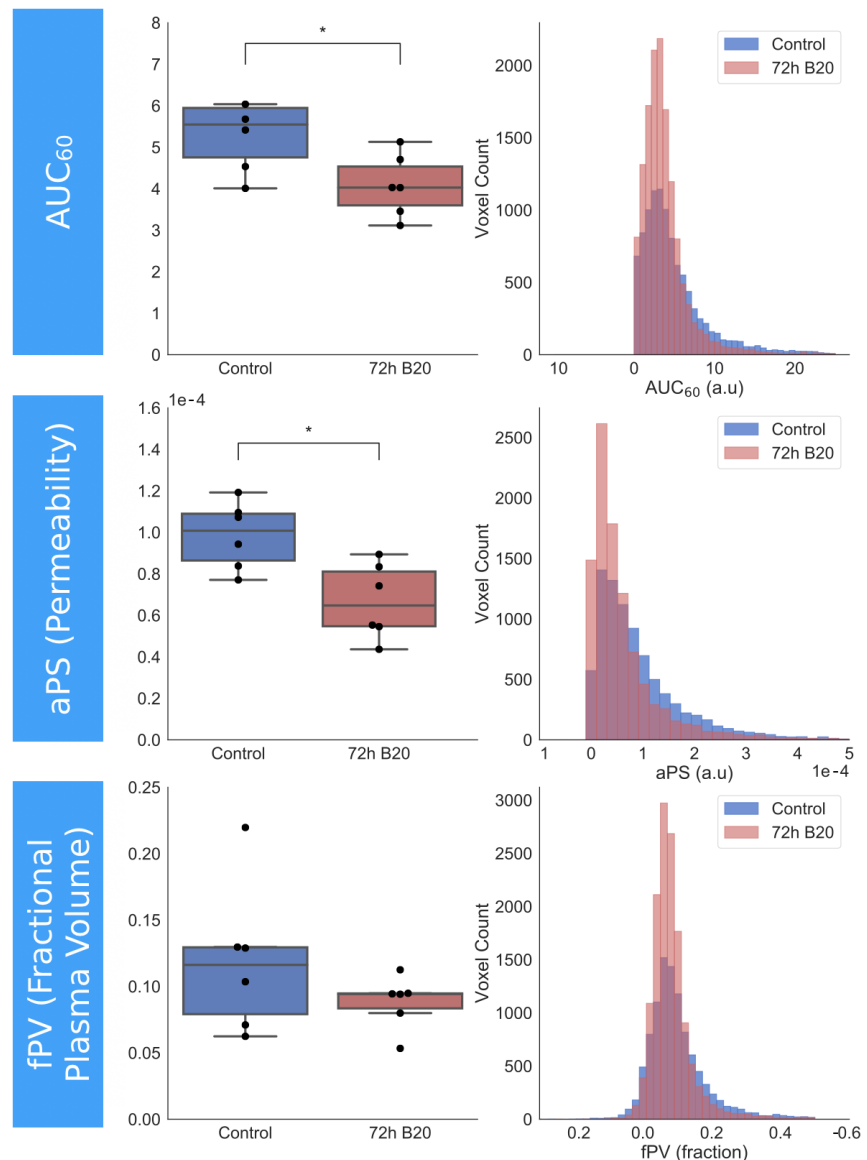


**Figure 4.4:** Summary of group differences for all three DCE-MRI parameters: AUC<sub>60</sub>, aPS, and fPV. There is a statistically significant reduction in AUC<sub>60</sub> and aPS for the treated tumours, but no difference measured for fPV. P-values from the Mann-Whitney *U* test for the comparisons were  $p = 0.03$  (AUC<sub>60</sub>),  $p = 0.01$  (aPS), and  $p = 0.15$  (fPV).

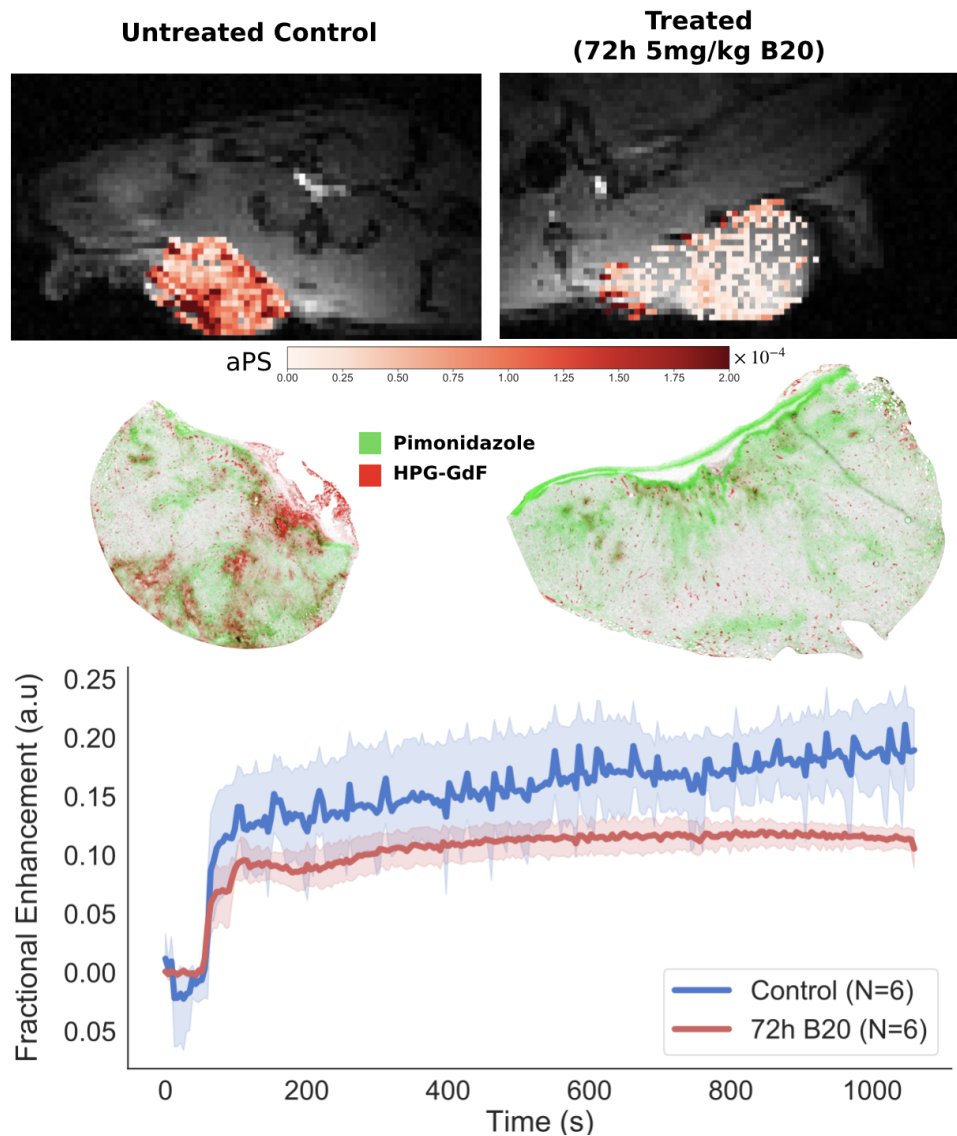


**Figure 4.5:** Histological stains of HPG-GdF shown alongside approximate slice matched DCE-MRI parameter map of aPS and the group-averaged contrast enhancement curves of control and treated tumours. There is an overall reduction in aPS for the treated tumours. The mean contrast enhancement curves (group means in dark blue and red lines; shaded region is the 95% confidence interval determined by bootstrapping) also show that the treated tumours have a higher enhancement slope after contrast agent injection.

mour microenvironment changes longitudinally [88]. However, there is a strong coupling of blood flow and vessel permeability in standard DCE-MRI models parameter interpretation varies based on the tumour microenvironment [89]. For instance, in regions of high permeability, the movement of the contrast agent is limited by blood flow so  $K^{trans}$  primarily measures blood flow. When applied in regimes of low permeability, the small molecular weight contrast agent cannot extravasate from vessels so  $K^{trans}$  primarily measures vessel permeability [90]. Contrast agent size affects measures of vascular permeability and low molecular weight agents result in underestimations of vessel permeability [87]. For applications where distinguishing between blood flow and vessel permeability is important, low molecular weight agents cannot be used unless more complex pharmacokinetic models are used.

The principal advantage of high molecular weight contrast agents is their intravascular nature so blood flow is removed as a contributing factor of the measurement. There is also an inverse relationship between size of the contrast agent and MR signal enhancement because larger molecules diffuse slower and extravasate less. The reduction in signal enhancement is partially compensated for by the increased relaxivity of the larger agent arising from more Gd-chelates attached to the molecule and a lower tumbling rate [31]. We have previously shown that the relaxivity of HPG-GdF is 300 times larger than standard DCE-MRI contrast agents but the agent extravasates only a few micrometers from nearby vessels [1], leading to an overall reduction in signal enhancement. Consequently, the larger the contrast agent, the less signal enhancement there is in the MR images. At a molecular weight of 583 kDa, HPG-GdF is considerably larger than common biocompatible high molecular weight agents that range from 20-92 kDa [31] and to our knowledge, is the largest agent with which a permeability measure has been obtained.

This study provides another application for the high molecular weight agent HPG-GdF in exploring the tumour microenvironment and the effects of vascular normalization.  $AUC_{60}$  of the signal intensity represents presence of HPG in the blood 60s after injection was also significantly lower in the treated mice which indicates the antiangiogenic treatment altered the tumour vasculature. There is considerably less variability in the enhancement curves of the treated tumours as shown in Figure 4.5, providing strong evidence for B20 normalizing the vascula-

ture. The vascular normalization hypothesis suggests that after treatment with an antiangiogenic therapy, the overall vessel permeability and the number of vessels will decrease. As summarized in Figure 4.4, our study has provided evidence for a decrease in vessel permeability (reduced aPS) as well as a decrease in accumulation of HPG-GdF (reduced AUC<sub>60</sub>). Additionally, we also showed a dramatic reduction in hypoxia (measured by pimonidazole staining) in the treated group.

A limitation of this study is that the model cell line used was a murine tumour model which may have limited potential for translation [91]. However, this tumour model is ideal for validating non-invasive MRI as it has no necrosis present due to its vascular architecture. Necrosis is a potential confounding factor in macromolecular contrast agent imaging studies as large areas of necrosis and empty space result in pooling of the agent in non-viable areas. Consequently in SCCVII tumours, any fluorescence present on cryosections has extravasated from nearby vessels and can be quantified as shown in Figure 4.2. Figure 4.3 shows low inter-tumour slice variability in average staining intensity of HPG-GdF fluorescence, but considerable heterogeneity exists between tumours and not all tumours responded consistently. On aggregate, it is evident that the treated tumours have significantly less HPG accumulation. Figure 4.3 also shows regions stained with both HPG-GdF and pimonidazole.

There is no clear explanation for why a macromolecule such as HPG-GdF accumulates in a region where oxygen is regionally distributed in such low concentrations. One possible explanation is that in longer imaging sessions tumors exhibit varying oxygenation patterns and since pimonidazole and HPG-GdF were administered over two hours apart, the tumour microenvironment had changed. Periods of oxygen-starvation and re-oxygenation cycling in tumors has been termed cycling hypoxia and can arise for intermittent periods based on temporary vessel occlusions, or may be permanent, chronic changes in hypoxia [92, 93]. However, as has been recently demonstrated, it is not as simple as classifying tumours in a binary fashion [94]. To enable a more thorough exploration of this phenomenon, more sophisticated methods are needed including a non-invasive method of assessing oxygenation status *in vivo* validated with multiple stains of hypoxia such as pimonidazole and EF5 administered sequentially with a delay to capture any changes that occur during the delay time. Additionally, slice-matched histology

sections and MR images were beyond the scope of this study and this would be needed to explore patterns of HPG-GdF staining and regions of high aPS or fPV.

An important difference in this study compared to our initial experiments with HPG-GdF [1] is that here we analyzed only the signal intensity enhancement rather than relying on an arterial input function to compute a contrast agent concentration. Largely due to constraints in available signal enhancement due to the high molecular weight contrast agent, sufficient signal was not present in all areas of the tumour for pharmacokinetic modelling or computation of contrast-agent concentration. Though this simplification is not ideal as it assumes signal intensity changes linearly with contrast-agent concentration, it is valid when contrast-agent concentrations are low [95] and relative group differences are being measured (rather than absolute changes in individual tumours). This and other challenges associated with a lack of standardization in analysis methods to use high molecular weight contrast agents poses a significant challenge for its use in the clinic as a tool to assess cancer therapies. Nevertheless, validation with histological images is a positive sign that the measurements of aPS and fPV reflect characteristics of the tumour microenvironment. Though we did not use a low molecular weight agent for comparison in this study, we have previously shown (summarized in Table 2.3) that DCE-MRI parameters from Gadovist (a low molecular weight agent) did not show a difference in vascular function between HT29 and HCT116, but a difference was measured when using HPG-GdF.

## 4.5 Conclusion

We have shown that aPS and AUC<sub>60</sub> decreases after administration of B20. Lower accumulation of HPG-GdF following treatment was confirmed by histology via direct HPG-GdF fluorescence imaging. Blood vessels of treated tumours appear to be less permeable, and tumour hypoxia was markedly reduced as a result of the anti-angiogenic drug. Unfortunately, existing MRI techniques do not permit measurement of oxygenation *in vivo* despite an unmet clinical need [96]. Our results indicate that HPG-GdF has potential applications in assessing effects of antiangiogenic agents on blood vessel permeability and function. Future work will include a panel of tumours with more diverse tumour microenvironments to evaluate its

utility in more clinically relevant tumour models. While it is unlikely that macromolecular contrast agents will become standard clinically, they are a very useful tool to improve our understanding of the tumour microenvironment and to develop novel drugs for cancer.

# **Chapter 5**

## **Oxygen-enhanced MRI**

### **5.1 Introduction**

Hypoxia is a well-established component of the tumour microenvironment, arising most often as tumour cell proliferation outpaces the growth of new vasculature. Tumour hypoxia is an indicator of poor prognosis and is responsible for tumour resistance to radiotherapy and some chemotherapies, but is also a potentially useful target for novel anti-cancer drugs [97]. Assessing tumour hypoxia in the clinical setting is challenging largely due to the invasive nature of biopsy-dependent techniques and the limited capacity and high expense of the more favoured, non-invasive PET imaging of hypoxia tracers [96]. The utility of screening patients for hypoxia was demonstrated retrospectively in trials of the hypoxic cytotoxin tirapazamine, where those patients with greater PET-imaged hypoxia experienced greater benefit [98]. However, subsequent trials of drugs targeting hypoxia, including those for evofosfamide that failed to show clinical benefit, have not used hypoxia imaging to stratify patients. A practical, widely applicable, and non-invasive imaging method is urgently required as a biomarker to monitor tumour hypoxia in many contexts, and is crucial to the development and clinical evaluation of future hypoxia-targeting drugs.

## 5.2 Theory

### 5.2.1 Physiology

The primary mode of oxygen delivery to tissue is the haemoglobin (Hb) molecule as it carries and delivers 98% of the oxygen in the body. Over 250 million Hb molecules are found in a typical red blood cell and each Hb molecule has four binding sites for oxygen molecules. The binding affinity for  $O_2$  drastically increases for subsequent oxygen molecules that bind to Hb as the conformation of the Hb molecule changes to increase binding affinity for the next oxygen, a phenomenon called cooperativity. Similarly, when the local environment of the Hb molecule changes such that  $O_2$  needs to be released, the reverse conformational changes occur; a proportionately lower drop in oxygen tension is then required to release the next  $O_2$  molecule. The dissociation of oxygen from haemoglobin molecules is well described by the oxygen-haemoglobin dissociation curve (Figure 5.1).

Upon inspiration of atmospheric air ( $p_{O_2} = 160$  mmHg), gas exchange in the pulmonary capillary beds occurs in the alveoli of the lungs (Figure 5.2). Incoming venous blood with a low oxygen tension ( $p_{O_2} = 40$  mmHg) is oxygenated as haemoglobin molecules readily bind available oxygen. As the oxygenated blood leaves the alveoli and moves through the systemic arteries, it has an oxygen tension of 100 mmHg. The oxygenated blood then travels from the arteries to the systemic capillary bed and the local oxygen tension drops from 100 to 40 mmHg. Simultaneously, while the Hb molecule undergoes a structural change releasing a molecule of  $O_2$  from its first binding site. The second release of the oxygen molecule occurs when the tension drops to 26mmHg [7]. In a population of Hb molecules fully saturated in tissue ( $S_{O_2} > 95\%$ ), the approximate  $\Delta p_{O_2}$  required to release the first  $O_2$  molecule is 60 mmHg (100-40 mmHg). The third  $O_2$  molecule is released when the  $p_{O_2}$  drops from 26 to 19 mmHg, and the final  $O_2$  molecule is released when the  $p_{O_2}$  drops to 12 mmHg [7]. Practically however, it is important to note that Hb molecules never release all four of the bound oxygen *in vivo*. This important feature of Hb (cooperativity) ensures that small changes in  $p_{O_2}$  have the appropriate effect in the appropriate place. For instance, in the lung tight binding is required so Hb can bind the  $O_2$  needed to supply all the tissues. Therefore, small changes

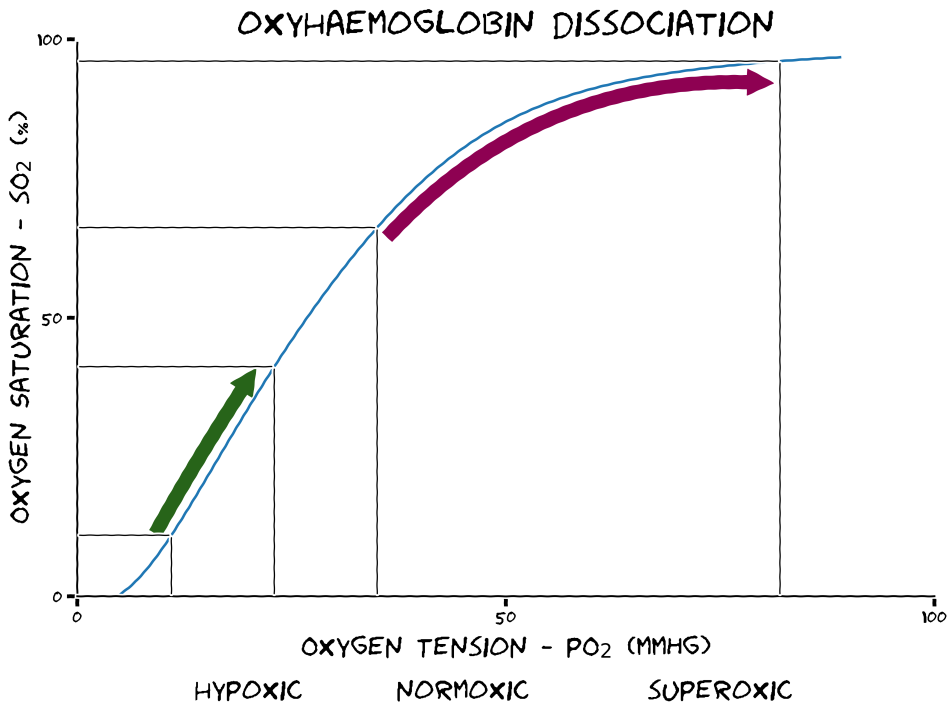


**Figure 5.1:** Sigmoidal curve illustrating the relationship between the haemoglobin saturation (y-axis) and the oxygen tension (x-axis). When the oxygen tension is low, the Hb easily binds  $O_2$  and there is a rapid rise in oxygen saturation (green arrow). Note that it takes a large increase in oxygen tension to bind the last  $O_2$  and similarly, a large decrease in oxygen tension to release the last  $O_2$  [7].

should not affect the release of  $O_2$ . Conversely, small changes in  $pO_2$  in capillary beds should result in quick release of  $O_2$  so it can easily diffuse to oxygen-starved tissues.

### 5.2.2 Origin of the OE-MRI signal

Oxygen is a paramagnetic molecule because it has two unpaired electrons and it is widely reported that the dominating effect in the OE-MRI signal is a  $T_1$  decrease after concentrated oxygen gas (100%  $O_2$ ) is breathed in [99, 100]. The excess oxygen travels through the blood stream dissolved in plasma and diffuses through the

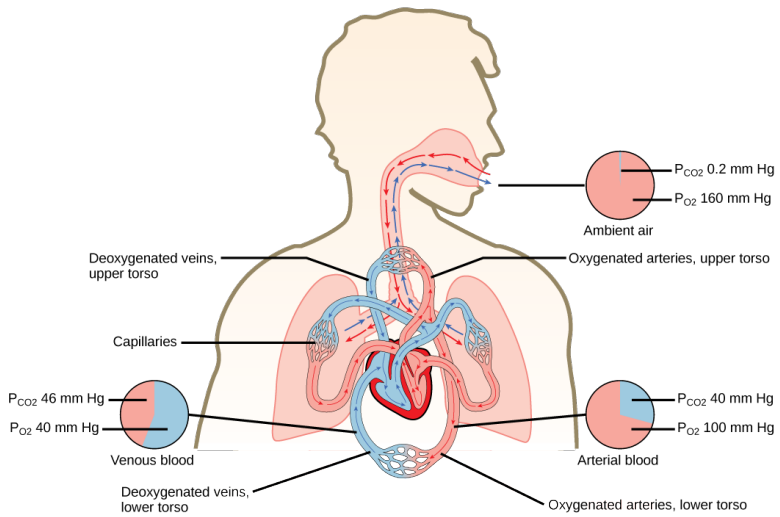


**Figure 5.2:** A schematic of the change in the partial pressures of oxygen and carbon dioxide at various points in the body. The  $p_{O_2}$  of inhaled ambient air is 160 mmHg, and this is breathed in to the lungs. Oxygen diffuses out of the alveoli into the surrounding capillaries and binds to Hb due to the pressure gradient (capillary  $p_{O_2}$  is 40 mmHg). This oxygenated blood ( $p_{O_2} = 100\text{mmHg}$ ) now enters the heart and is pumped through the body, with the Hb releasing oxygen through capillaries due again to the pressure gradient (tissue  $p_{O_2}$  is  $< 40\text{ mmHg}$ ) [8]. Textbook content produced by OpenStax Biology is licensed under a CC-BY 4.0 license.

vessel walls and dissolves in interstitial tissue fluid (Figure 5.3). The net increase in dissolved oxygen results in a dramatic and measurable decrease in  $T_1$ . This change is reversed soon after the patient is switched back to breathing atmospheric air as excess oxygen is expelled or metabolized. Perfused tumour regions (i.e regions that already have a high Hb-O<sub>2</sub> saturation) will see a measurable decrease in  $T_1$ . The perfused regions that do not show a decrease in  $T_1$  must therefore be hypoxic [99]. Importantly, OE-MRI does not yield any information about unperfused regions and in that region, there are likely to be pockets of viable (but hypoxic) tissue. Though outside the scope of this study, blood-oxygen level dependent (BOLD) imaging may provide insight into these regions by exploiting the paramagnetic properties of deoxyhaemoglobin. Dunn et al. explored the use of deoxyhaemoglobin as a contrast agent by coupling BOLD imaging with a modification to the inhaled gas

(carbogen) in intracranial rat tumours [? ]. This study [? ], and others since then [108, 109, 111? ] have established that  $T_2^*$  increases as tumour oxygenation improves using a variety of breathing gases. Section 8.6 outlines this technique in more detail and how it could be used with dOE-MRI to obtain a more complete picture of the tumour microenvironment.

The oxygen status of healthy tissue is fairly well regulated in normal tissue and every cell in the body is at most  $150\mu\text{m}$  away from a blood vessel. In tumours however, the vascular network is chaotic and the growth patterns of vessels are abnormal leading to a defective and leaky endothelium [16]. Irregular diameters of tumour vessels, abnormal branching patterns and porous vessel walls all contribute to an increase in vessel permeability and pockets of hypoxic tissue. Although  $pO_2$  and  $pCO_2$  are by far the largest factors in determining Hb saturation, related factors such as pH and temperature also play a role. Furthermore, these hypoxic regions are heterogeneous, transient, and drastically differ between tumour models. In a mammary adenocarcinoma mouse tumour model, Sorg et al. used spectral imaging with an implanted window chamber to show that upon breathing 100% oxygen, the Hb saturation in the tumour vascular network increases from 20-30% up to 70-80% while the Hb saturation in the normal vascular network does not change appreciably [101].

### 5.3 Motivation

The  $T_1$ -shortening property of oxygen dissolved in fluid has been known since 1955 [102] and pioneering work by Young et al. showed that oxygen acts as a paramagnetic contrast agent by demonstrating its ability to reduce  $T_1$  upon inhalation [103]. Inhalation of 100% oxygen has also been shown to elicit strong  $T_1$  effects in the kidney[104], spleen[105] and the poorly oxygenated retina [106]. Subsequent oxygen-enhanced MRI (OE-MRI) efforts have included either acquisition of quantitative  $T_1$  maps before and after oxygen breathing, or acquiring dynamic  $T_1$ -weighted (T1W) signal intensity images and calculating  $\Delta T_1$  during periods of oxygen inhalation. The subtle but measurable influence of tissue oxygenation on  $T_1$  in tumours has been reported by O'Connor [23, 99, 107, 108], Mason [109–111], Gallez [112], and others [100, 105, 113, 114]. However, due to the changes

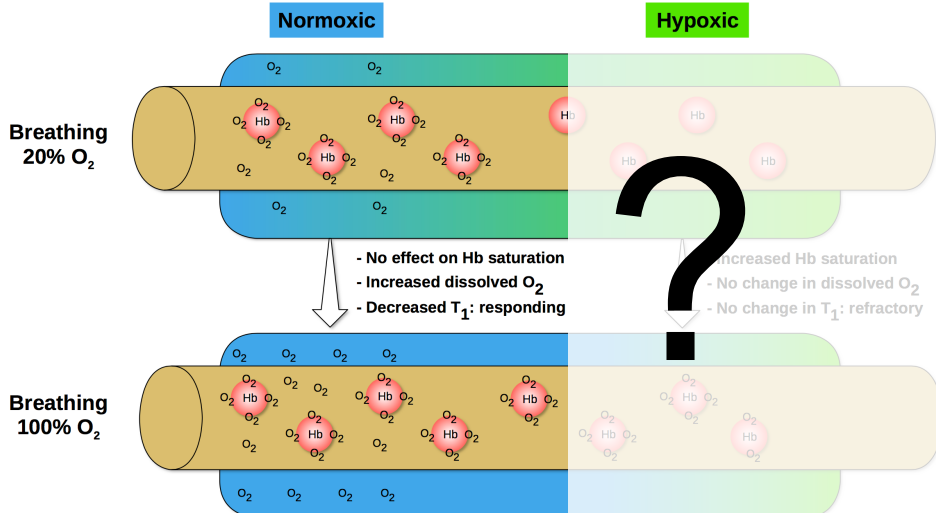


**Figure 5.3:** A schematic representation of our current understanding of the origin of the OEMRI effect. In normoxic tissue, Hb is almost fully saturated and any excess breathed O<sub>2</sub> cannot bind to the Hb molecule. Consequently, O<sub>2</sub> dissolves in the blood plasma and as the excess oxygen diffuses out into the tissue, it also dissolves in the interstitial tissue fluid resulting in a net T<sub>1</sub> decrease. It is hypothesized that in the hypoxic tissue, Hb is not fully saturated with oxygen due to increased tissue demands and/or a poorly organized vascular network. The excess breathed oxygen in this case binds to the Hb molecule and does **not** dissolve in the plasma leading to no change in T<sub>1</sub>.

in T<sub>1</sub> that arise as oxygen dissolves in the plasma and interstitial fluid being quite small, T<sub>1</sub> maps have poor sensitivity and application of OE-MRI techniques in cancer has yielded mixed success. OE-MRI continues to suffer from low SNR and it has not found routine clinical use largely because isolating small signal changes due to dissolved O<sub>2</sub> is a challenge [99, 109].

Typical imaging times for existing OE-MRI methods range from 20-45 minutes often making it impractical for easy inclusion in experimental protocols. An MRI technique measuring tumour oxygenation that is sensitive, fast, flexible, repeatable, and non-invasive has the potential to significantly impact the clinical fields of radiation biology and hypoxia drug targeting. In this study, we present a new dy-

namic OE-MRI (dOE-MRI) method that allows extraction of very small dynamic signal changes in T<sub>1</sub>W images by inducing step changes in the inspired oxygen through a repeated, cycling gas challenge. To isolate the signal component that matches cycling gas, a blind source separation approach called independent component analysis (ICA) is used to analyze MR images as first proposed by McKeown et al [115]. ICA is a form of blind source separation algorithm that separates the additive signals on the basis of the statistical independence of individual components [116]. With the application of a cycling oxygen challenge and processing the data using ICA, our dOE-MRI approach represents a significant improvement in the sensitivity and application of MRI for measuring tumour oxygenation, making it more practical for wide application.

## 5.4 Methods

This section of the thesis introduces and describes the dOE-MRI technique and discusses technical details of the technique. Its characteristics are described in sections 5.5.1, 5.5.3, 5.5.7. An analysis of robustness is done in section 5.5.5, repeatability in section 5.5.8, and variability in section 5.5.4. Ninety-one ICA extractions were done in a total of eighty-one (N=81; some mice had two distinct tumours) mice that were scanned in a variety of experimental conditions. Multiple tumour lines are explored in Chapter 6 and a tumour treatment study is discussed in Chapter 7. Below methods for the dOE-MRI technique are discussed, and subsequent chapters will refer to these details and provide amendments as needed.

### 5.4.1 Mice and tumours

Female NRG (NOD rag gamma) mice were implanted with murine squamous cell carcinoma (SCCVII; 5x10<sup>5</sup> cells in 50 µl serum-free media; cells provided by Dr. J. Evans) in the dorsal subcutaneous region. These mice and tumours are shown in all figures in this chapter except figure 5.10, which contains the aggregate data across all dOE-MRI experiments). Mice were anaesthetized with isoflurane for the duration of imaging sessions until euthanasia, and were positioned supine on the custom surface coil apparatus. Throughout the imaging session, a small animal monitoring system (SA Instruments Inc., Stony Brook, NY, USA) was used to

monitor respiration rate, varying between 80-100 breaths per minute, and body temperature, maintained at  $36.8 \pm 0.5^\circ\text{C}$  using a continuous airflow heater. All animals were injected with 60 mg/kg pimonidazole hydrochloride (HypoxiProbe) 30 min prior to imaging to label hypoxic cells and were euthanized within 15 min of imaging completion. Tumours were embedded and frozen in optimum cutting temperature medium (OCT; Tissue-TEK).

#### 5.4.2 MRI data acquisition

All MRI experiments were performed at the UBC MRI Research Centre on a 7T Bruker BioSpec 70/30 scanner at room temperature with a volume transmit coil and custom surface receive coil. Each imaging session began with pilot axial and coronal  $T_2$ -W scans for tumour localization and slice prescription. Eight contiguous axial slices (1 mm thickness) were acquired with an in-plane field of view of  $3.84 \text{ cm} \times 1.92 \text{ cm}$  and a matrix size of  $128 \times 64$ . Dynamic oxygen-enhanced MRI (dOE-MRI) scans were acquired with a 2D multi-slice FLASH-based sequence with  $T_E/T_R = 2.67/66.7$ ,  $\alpha = 40^\circ$ , temporal resolution of 4.3 s with 198 repetitions for a total scan time of about 14 min. The spatial resolution and geometry for all scans in the imaging session were matched and an experienced operator outlined the tumour on each slice of the anatomy MR images to construct the region of interest (ROI) for each animal.

**Gas challenge during MRI:** tumour-bearing mice began the dOE-MRI gas challenge breathing medical air and were switched between 100% oxygen and medical air in two-minute intervals. This paradigm continued for three cycles over a total of fourteen minutes; gases were switched manually and each switch took about five seconds to complete.

#### 5.4.3 MRI data analysis

**dOE-MRI maps:** A suite of in-house software was developed based on the technique described by Hyvarinen [116]. Specifically the python machine learning library scikit-learn, `sklearn.decomposition.FastICA`, was used [117]. The FastICA algorithm is applied to serially acquired  $T_1$ W images and the output is a paired set of components and weighting factors for each voxel in the dataset. Ex-

tracted independent components are not ordered and while the component selection can be automated, in this study an observer was assigned to select the appropriate component (Figure 5.4). The number of independent components for each imaging session was chosen by the operator and ranged from 4-9 to ensure the cyclic behaviour of the T<sub>1</sub>W signal intensity corresponding to the gas challenge appeared in only one component. The dOE-MRI maps were obtained by dividing the ICA weighting-factor maps by the mean signal-intensity maps to obtain a spatial map for the strength of a particular voxel's contribution to the component of interest ( $c_4$  in Figure 5.4). In these dOE-MRI maps, voxels are coloured to indicate the amount by which a given pixel intensity timecourse is modulated by the oxygen-related component. The green-white-purple colour spectrum depicts the degree to which voxels respond to the cycled gas challenge. Purple indicates O<sub>2</sub>-positive voxels whose timecourse exhibits a higher and more positive contribution from the corresponding ICA component, representing an increase in T<sub>1</sub>W signal intensity in response to the supplied 100 % oxygen. O<sub>2</sub>-negative voxels that show a decrease in T<sub>1</sub>W signal intensity with a negative contribution from the corresponding ICA component under 100 % oxygen breathing are depicted as green. Regions whose T<sub>1</sub>W signal intensity timecourses responds only weakly or not at all to the gas challenge are shown in white hues. Fraction of voxels that are negative on dOE-MRI maps were correlated with the histological hypoxic fraction using Pearson's r.

**OE-MRI without ICA:** To assess whether or not ICA was necessary to create oxygenation maps, the MR signal intensity data was correlated with three modelled paradigms: 1) a square wave which corresponds to the concentration of delivered oxygen; 2) a synthetic hemodynamic response function (HDRF) created by convolving a square wave with an exponential ( $\tau = 0.32\text{ms}$ ); 3) Fourier filtered response curve (details below). The value of  $\tau$  for the HDRF was determined by manually fitting a portion of the ICA-extracted oxygen-enhancing component to the HDRF with a range of  $\tau$  values. Correlations were calculated voxel by voxel using:

$$r = \frac{\sum_{i=1}^n (x_i - \bar{x})(y_i - \bar{y})}{\sqrt{\sum_{i=1}^n (x_i - \bar{x})^2 \sum_{i=1}^n (y_i - \bar{y})^2}} \quad (5.1)$$

where  $x$  is the model paradigm and  $y$  is the T<sub>1</sub>W signal intensity timecourse. The

resulting correlation maps are estimates of the strength of the input paradigms with the acquired signal intensity.

**Fourier filtered response curve:** Frequency-based filtering was applied to the extracted ICA component to isolate the periodicity in the signal intensity response. Fourier filtering was applied by first Fourier transforming the extracted ICA component for an animal. Next, all but the highest frequency response was filtered out and the magnitude of the signal was plotted against the frequency. Finally, an inverse Fourier transform was applied to the filtered data and this was considered to be the periodic response curve for the animal. This extracted response curve was then correlated with the mean-normalized signal intensity voxel by voxel as described in the preceding paragraph to produce the “Fourier transform” correlation map.

**Extracting the periodic signal using Fourier transforms only:** A standard signal processing method was deployed voxel-by-voxel to extract the periodicity in the signal intensity data. First, the MR signal intensity data was normalized to the mean intensity in each voxel. Then, this normalized data was Fourier transformed and the intensity at the frequency of interest (selected by Fourier transforming the ICA-extracted component) was visualized voxel-by-voxel.

#### 5.4.4 Quality Scores

A coarse qualitative scoring system was developed to evaluate the quality of the ICA component from all 91 extractions. The scored extractions are shown in figure 5.10. This is similar to the Gleason score that radiologists use to predict the aggressiveness of prostate cancer by looking at tissue biopsies. The levels of the scoring system and the associated explanations were:

- Unusable: These extractions were removed from consideration as they do not correspond to the cycling paradigm in a meaningful way.
- Poor: In these cases, the extracted component corresponds to the cycling paradigm, but either due to imaging noise, motion, or notably different physiological response, the extracted component is noisy.
- Satisfactory: A distinct pattern matching the cycling gas paradigm is present

and recognizable.

- Good: These extractions contain trends other than the cycling paradigm, and there is some variability in the “humps”
- Ideal/perfect: These extractions are ideal and show the presence of a strong cycling component with very little noise, and approximately equal “humps”

## 5.5 Results

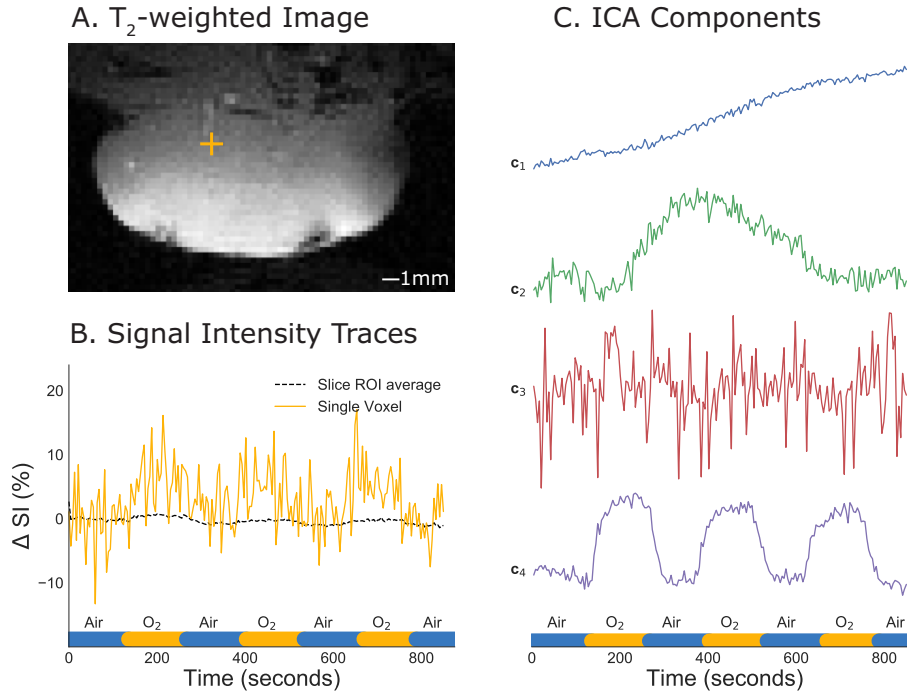
### 5.5.1 ICA isolates small changes in T<sub>1</sub>W signal intensity

An example signal intensity vs. time curve is shown for a whole slice ROI compared with a single voxel (Figure 5.4B). A mean signal intensity increase is seen for both the whole slice and the individual voxel during each of the oxygen periods of the cycle, however the magnitude of  $\Delta SI$  for the individual voxel is about 10% and the noise is of the same order of magnitude. The slice-averaged time-course has much less noise compared to the individual voxel, but the size of the effect is significantly reduced, the contrast to noise is similarly poor, and all spatial heterogeneity in the response is lost in the averaging process.

To retain spatial information and improve the sensitivity of the technique, ICA was applied to the same dataset and in this example, four independent components were extracted (Figure 5.4C). Each individual independent component is scaled such that its norm is one ( $\|c_i\| = 1, \forall i$ ). Only one extracted component follows the step function of the oxygen challenge and positively identifies an effect of oxygen breathing ( $c_4$ ). Speculations for the source of the other components is provided in Figure 5.12.

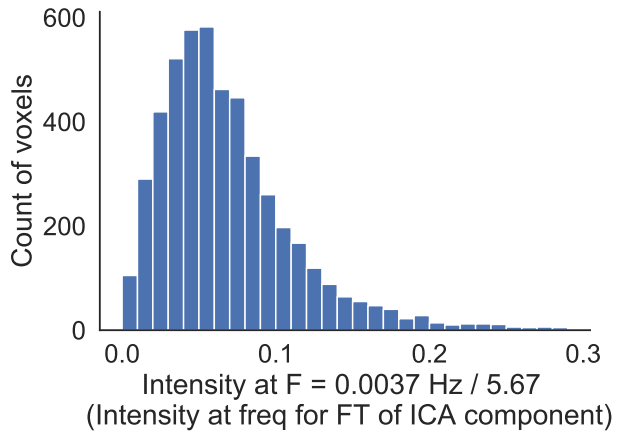
### 5.5.2 Extracting periodicity of the signal intensity change using a Fourier transform based approach is less sensitive than using ICA

Figure 5.5 shows the normalized intensities of the frequency of interest in the tumour. The normalized mean across all the voxels was 0.07, nearly eighty times



**Figure 5.4:** (A)  $T_2$ W MRI of a tumour xenograft at 7T and (B) the corresponding  $T_1$ W signal-time traces of a single voxel (solid yellow) and whole-tumour slice ROI (dotted black) during gas cycling at two-minute intervals of air (x axis; blue) and O<sub>2</sub> (x axis; yellow). (C) Plot of the four extracted ICA components from the entire tumour ROI, component  $c_4$  (purple) exhibits the same temporal features as the oxygen cycling time course shown along the bottom. All components are normalized, no vertical scale is shown. Figure reused with permission from Wiley and Sons.

lower than the value at the frequency of interest extracted from the ICA component (5.67). This indicates the SNR at the voxel level is not high enough to use the Fourier filtering method to extract the periodicity of the signal intensity signal. Figure 5.6 shows the spatial patterns of the intensities. Comparing Figure 5.6 and 5.8 shows that the regions of high intensity at the frequency of interest are correspond strongly to the highly O<sub>2</sub>-positive (purple) regions.



**Figure 5.5:** Histogram of all the normalized intensities at the frequency of interest in all the tumour voxels. The intensities were normalized to the value at the frequency of interest extracted from the ICA component (5.67), plotted on the x-axis.

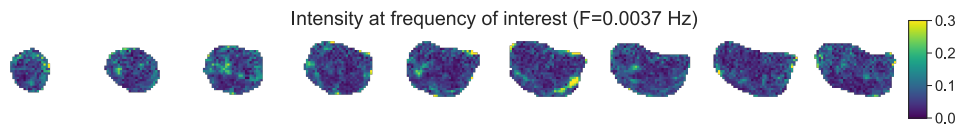


**Figure 5.6:** The normalized intensities at the frequency of interest as a spatial map. Higher values in the spatial map are represented as green and low intensity values are dark.

### 5.5.3 dOE-MRI with ICA does not require assumption of a response function

To determine whether dOE-MRI maps obtained with a model-free ICA approach (Figure 5.7A) are comparable to maps assuming mathematical models of the response, alternative oxygenation status correlation maps were constructed (Figure 5.7B and C). In Figure 5.7B and C, two example mathematical models - a square wave and the estimated hemodynamic response function (HDRF) - are correlated to the voxel-by-voxel raw time signal. Regions most correlated with the input paradigm remained purple in both alternative maps generated from modelled response functions. Figure 5.8 shows the result of the Fourier filtering process as well as the resulting correlation map for individual slices of a tumour. The

values of the correlation map from the Fourier-filtered response curve were correlated with the dOE-MRI map with Pearson's  $r = 0.72$ . Particularly when using the HDRF, the alternative oxygenation map showed very similar patterns in the regions demarcated as  $O_2$ -positive and  $O_2$ -negative. However, the map generated from correlating a square wave led to consistent underestimation of oxygenation relative to the model-free dOE-MRI map.

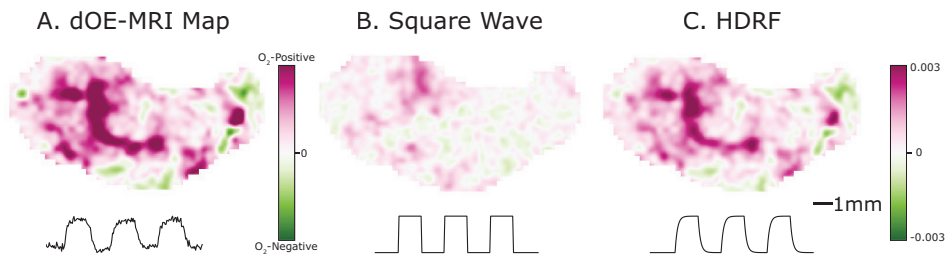


**Figure 5.7:** (A) dOE-MRI map of an SCCVII tumour where purple voxels contribute strongly to the extracted component using ICA in the  $T_1W$  signal timecourses. Green voxels in the dOE-MRI map have a strong contribution of the inverse extracted component. Pearson's  $r$ -maps are shown correlating the raw time-signal voxel by voxel with a square wave (B), and an exponential convoluted with a square wave called the hemodynamic response function (HDRF) (C). Panels B and C are correlation maps whereas A is the dOE-MRI map from ICA. Note the low correlation coefficients (on the order of  $10^{-3}$ ) are characteristic of the extremely low amplitude of the oxygen cycling compared to other competing effects. Figure reused with permission from Wiley and Sons.

#### 5.5.4 Variability of response in individual oxygen cycles

A full dOE-MRI sequence involved three cycles of oxygen but to assess the potential for shortening the sequence we also separately applied ICA to each of the three oxygen cycles independently. Separate dOE-MRI maps, as well as voxel-wise correlation plots of a representative SCCVII tumour, are shown in Figure 5.9 with Pearson's  $r_{all-1}=0.74, r_{all-2}=0.86, r_{all-3}=0.84$ . Pearson's  $r$  ranged from 0.79 to 0.87 for a similar analysis in a representative HCT-116 tumour.

The stability of the independent component extraction was assessed by undersampling the full timecourse threefold prior to application of ICA, and a high

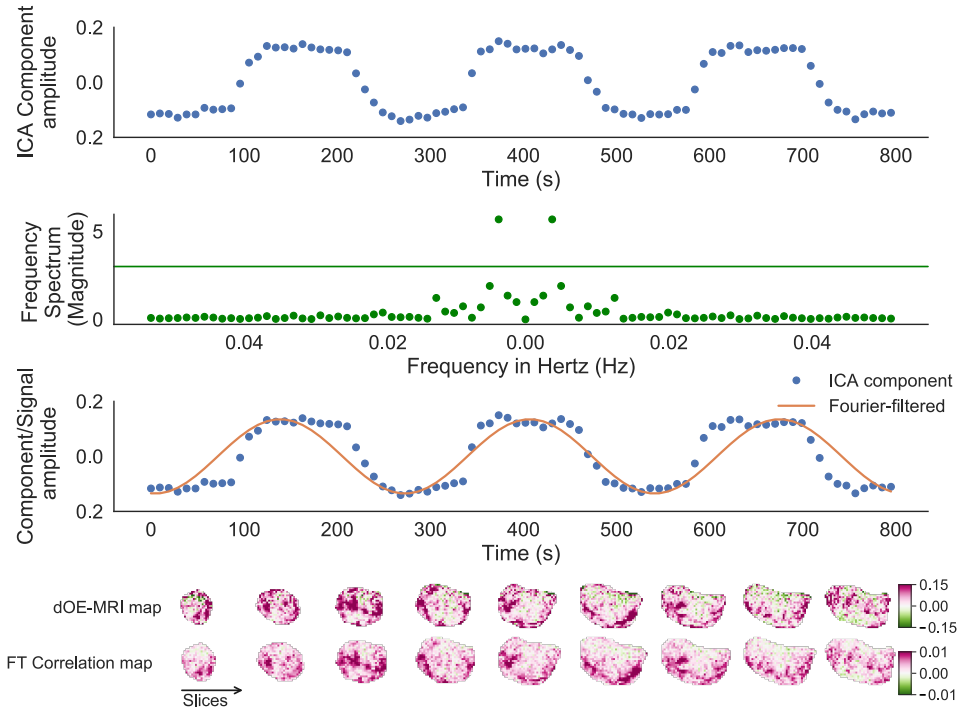


**Figure 5.8:** The first row shows the extracted ICA component of a whole tumour. The second row shows the magnitude of the Fourier-transformed signal plotted against frequency in Hz. The highest frequency is kept and all other values are set to 0. This filtered data is inverse Fourier transformed to produce the Fourier-filtered response curve. This response curve is plotted in the third plot. A correlation map (colour bar ranging from -0.01 to +0.01) of the Fourier-filtered response curve with the mean-normalized signal intensity is shown alongside the dOE-MRI map (colour bar ranging from -0.15 to +0.15) for comparison.

correlation between the dOE-MRI maps from full and three-fold undersampled timecourses is observed (Figure 5.9E; Pearson's  $r = 0.84$ ). In Section 5.5.6, further undersampling up to a factor of six is shown with minor differences in the dOE-MRI map.

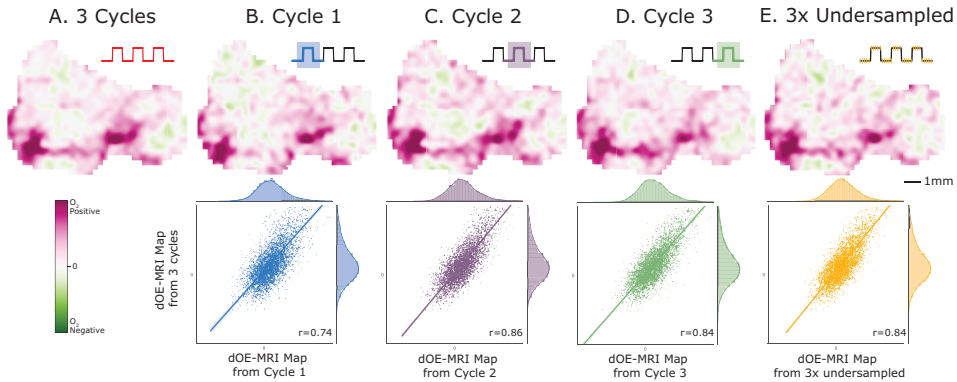


**Figure 5.9:** The dOE-MRI map including the full dataset of all three cycles (A) is compared to each of the three gas cycles separately (B,C,D), and to a map that temporally undersamples by selecting every third datapoint from the full dataset (E). Voxel-wise plots of each map are correlated to the full dataset and a linear regression with Pearson’s  $r$  is shown. Figure reused with permission from Wiley and Sons.

### 5.5.5 Quality of extracted component

Across 91 extractions, figure 5.10 shows the quality of the extraction process for each dataset. A quality score of 1 was given only five times, and a score of 2 was given sixteen times (out of 91). Only data with a quality score of 1 was discarded from analysis, and in the studies presented in this thesis, no data was discarded. A quality score of five, four, and three was awarded thirty-three, twenty-two, and fifteen times, respectively.

### 5.5.6 dOE-MRI can be extended by interleaving other scans between each repetition

To investigate the subsampling limit of ICA, Figure 5.11 shows the dOE-MRI maps for progressively more severe undersampling.  $O_2$ -positive and  $O_2$ -negative regions are repeatable for all maps (plot in Figure 5.11) until subsample 5, where only 40 of the 200 available data points were used. The original data was acquired at a temporal resolution of 4.3 s but at subsample 5, the effective temporal resolution goes to 21.3 s. In other words, temporal resolution could be sacrificed for SNR simply by averaging. More usefully, the additional time can be repurposed to interleave

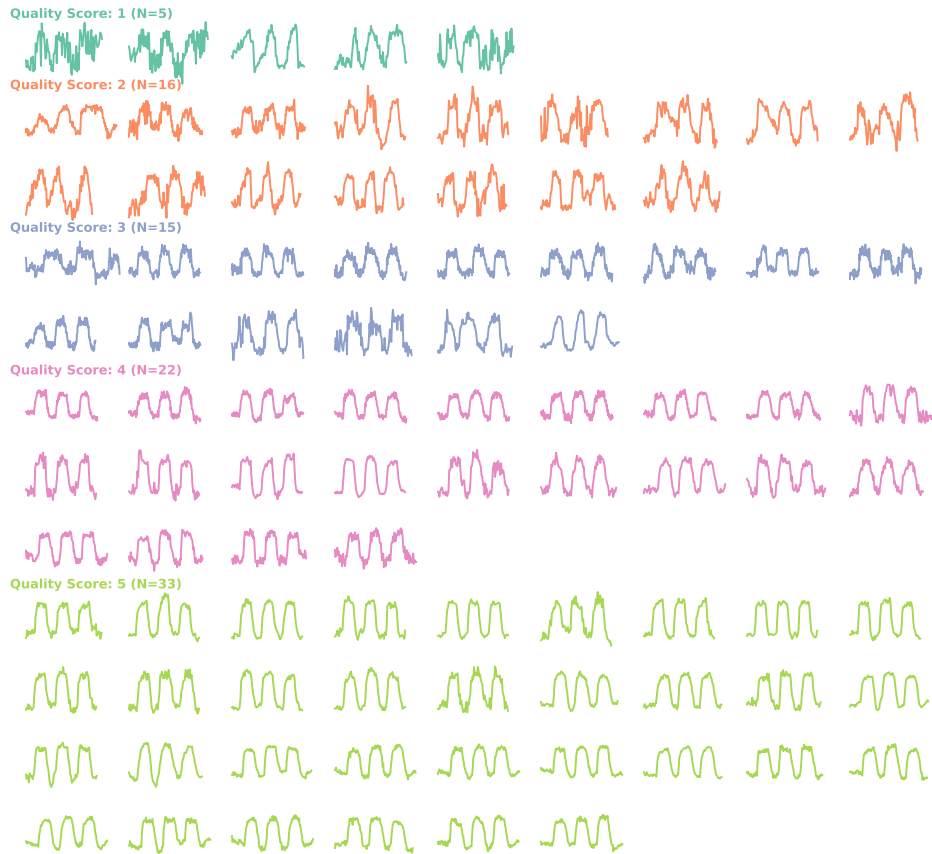


**Figure 5.10:** All ninety-one dOE-MRI extractions shown with the quality scores (1=unusable to 5=ideal) and the number of tumours shown in parentheses. Colours represent the different scores with 1 in dark green, 2 in orange 3 in blue, 4 in purple, and 5 in lime green.

other scans for multi-parametric imaging within an dOE-MRI scan. Details of this are discussed in section 8.6.

### 5.5.7 Exploring other independent components extracted using ICA

Figure 5.12 shows the extracted independent components and their corresponding weighting factor maps for an application of ICA on a OE-MRI scan. Extracted components typically have a mix of high and low frequency responses and may

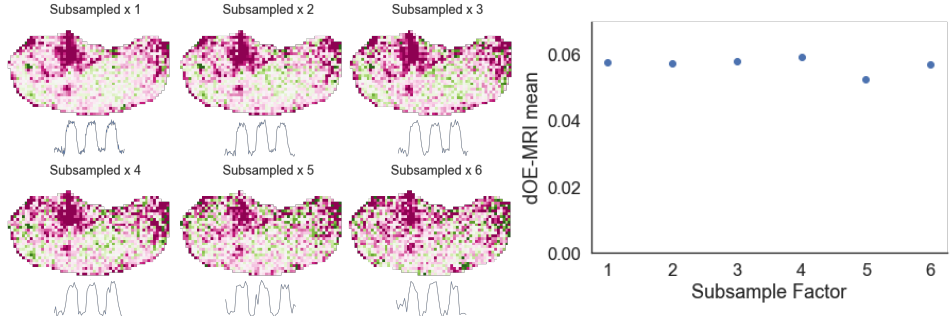


**Figure 5.11:** dOE-MRI maps and associated component traces of differently sampled data. To achieve different levels of subsampling, the raw data was spliced and then ICA was applied. The oxygenation maps look very similar between different subsample factors. Temporal resolution and number of points were 4.3 s and 200 points (subsample 1), 8.5 s and 100 points (subsample 2), 12.8 s and 67 points (subsample 3), 17.1 s and 50 points (subsample 4), 21.3 s and 40 points (subsample 5), and 25.12 s and 34 points (subsample 6).

include temperature drifts, breathing artefacts and other motion. For instance,  $c_4$  is clearly the component of interest here as the cycling pattern is not present in any other component. We speculate that  $c_1$  corresponds to a temperature drift over the course of the scan and  $c_3$  is likely related to a breathing motion artefact. Component 2 is a relatively weak spurious signal fairly low in magnitude with no obvious spatial or temporal pattern. Additional physiological monitoring data is needed for a more thorough analysis of the other independent components and whether they can aid our understanding of the mechanism of action.

### 5.5.8 Comparing oxygen responsiveness with dOE-MRI across experiments

It is necessary to characterize entire tumours in a compound fashion for comparison between groups or studies. Existing quantification methods have involved computing fractions of positively responding and negatively responding voxels as a surrogate for oxygen responsiveness in tumours with dOE-MRI. However, this semi-quantitative metric relies on a binary classification of voxels as either  $O_2$  positive or  $O_2$ -negative. Calculating fractions is sufficient to broadly categorize

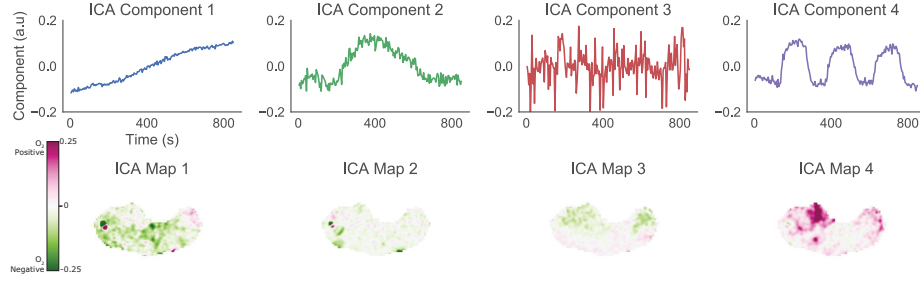


**Figure 5.12:** Plots of the four components extracted from ICA are shown ( $(||c_i|| = 1, \forall i)$ ) along with the corresponding weighting factor maps (normalized to mean voxel wise mean signal intensity). Corrupting influences such as temperature drifts are often present and produce slowly increasing or decreasing trends (for e.g.,  $c_1$ ) and breathing artefacts corresponding to short-lived spikes ( $c_3$ ). No explanation could be found for  $c_2$ . Figure reused with permission from Wiley and Sons.

tumours as oxygenated or not but consequently, rich information about the level of response is lost. Here we present an improved quantification method of dOE-MRI data that captures the level of response and furthermore, allows direct comparison of data acquired at varying temporal resolutions.

Since each extracted ICA component is scaled such that its norm is one ( $(||c_i|| = 1, \forall i)$ ), weighting factor maps are only directly comparable between scans if dOE-MRI images are acquired at the same sampling frequency over the duration of the cycling oxygen (14 minutes). However, holding the sampling frequency fixed over different experiments is not practical as imaging tumours of different sizes require modification of the field of view and consequently, temporal and spatial resolutions. A scaling  $s$  factor must be applied to scale component map values so they can be compared between scans of different temporal resolutions,

$$s = \frac{\sqrt{N_{ref}}}{\sqrt{N}}. \quad (5.2)$$

A reference sampling frequency should be chosen and in this study, it was chosen to be  $0.24\text{s}^{-1}$  (corresponding to  $N=198$  images over the cycling oxygen).

Gas delivered to mice switches between room air and 100% oxygen in two

minute cycles, for a total of 14 minutes. ICA extracts the tissue response to the delivered oxygen, and four periods of room air interspersed with three periods of oxygen can be modelled mathematically using a general Heaviside function:

$$y(t) = \begin{cases} +b & \text{if } t \geq \frac{4T}{7} \\ -b & \text{if } t < \frac{4T}{7} \end{cases}, \quad (5.3)$$

where  $T$  is the total imaging time and  $T/7$  is the time for a single segment of the gas challenge. The Fast ICA algorithm places a condition on the norm of the extracted component  $y(t)$ ,

$$\sqrt{\sum_{i=1}^N |y(t_i)|^2} = 1. \quad (5.4)$$

Simplifying the expression above for our  $y(t)$  (the Heaviside function), we have:

$$\begin{aligned} 1 &= \sqrt{b^2 \sum_{i=1}^N 1^2} \\ b &= N^{-\frac{1}{2}} \end{aligned} \quad (5.5)$$

With this, we can compute the scaling factor directly using  $b_{ref} = 198$  repetitions as the reference:

$$\begin{aligned} s &= \frac{b_N}{b_{ref}} \\ s &= \frac{\sqrt{198}}{\sqrt{N}} \end{aligned} \quad (5.6)$$

This scaling factor was applied to all dOE-MRI maps used in this study to retain information about the level of response to the supplied oxygen across scans with different sampling frequencies.

## 5.6 Discussion

In this study, we presented an improved method for OE-MRI that employs two synergistic techniques to achieve higher speed and greater sensitivity. First, a repeated gas challenge was used to probe tissue response by introducing an independent signal modulation unrelated to spurious contributions such as temperature drifts and motion. A repeating gas challenge improved the detection sensitivity of small amplitude signal changes that are typical of oxygen-enhanced MRI. Second, a repeating signal modulation enabled further improved sensitivity through the use of ICA, a signal processing technique to isolate source signals -  $T_1W$  changes due solely to the cycling oxygen - without knowledge of the tissue response (Figure 5.4). While it is possible to generate correlation maps of the oxygen cycling paradigm with  $T_1W$  signal changes that appear very similar to dOE-MRI maps, an *a-priori* assumption of a response function is required for this approach (Figures 5.7 and 5.8). In theory, Fourier-filtering may be useful in isolating the periodicity of the oxygen response on a voxel-by-voxel manner. The overall mouse response may then be obtained by averaging the frequency response across the entire tumour. However, the individual voxel time courses are quite noisy and the Fourier filtering process is prone to fail, particularly in regions where no oxygen dissolves in the plasma to reduce  $T_1$ . Similarly, Fourier transforming the signal intensity data voxel-by-voxel and visualizing the spatial map of the intensity at the frequency of interest (Figure 5.6) suggests the SNR in individual voxels is too low to apply this technique. Admittedly, the Fourier-filtered response curve extracted **after** performing ICA is a somewhat contrived exercise. However, this analysis very clearly shows that even in the best-case scenario - applying a Fourier Transform on the extracted ICA curve - it is not appropriate to model the oxygen response with a sinusoid. Furthermore, presupposing a particular oxygen response function biases the identification of responding  $O_2$ -positive voxels (Figures 5.7 and 5.8) underscores the need for a model-free approach to extract the oxygen-responding component.

A robustness analysis of all ninety-one extractions is shown in figure 5.10. Though component selection is currently a manual process, Figure 8.3 (appearing in the last chapter of this thesis) clearly shows that the number of components selected has almost no bearing on the dOE-MRI maps produced. The technique

appears quite robust as over 75% of the tumours imaged had a quality score of “satisfactory” or higher. Only five datasets were excluded from subsequent analysis (quality score of 1). Typical reasons for a score of 1 (unusable or no extracted component) were excessive motion or poor SNR but in some cases it was difficult to explain poor extraction. Further work is needed to explore whether the poor extraction is due to an actual physiological response (or lack thereof), histologically distinct tumour microenvironment, excessive motion, or MR signal/noise considerations. Indeed, it may be interesting to further investigate the tumours/animals that do not appear to respond to the oxygen stimulus in a consistent and expected way.

However, the unambiguous match of the identified components for a vast majority of the extracted components with the periods of the gas cycles increases the confidence that the small  $T_1$ W signal changes result from increased oxygen dissolved in the plasma and interstitial tissue fluids. Maps from other extracted components (Figure 5.12) exhibit spatial patterns that could provide clues to the signal sources but associating meaning to them is challenging and would require additional data. For example, even moderate shifts in temperature could drive a measurable change in  $T_1$ W signal during the timecourse, and a physiological monitoring system that is temporally synchronized to the MR acquisition could illuminate this confounding variable. Nevertheless, we have established reliability of the technique by comparing maps from each cycle of the gas challenge to the map incorporating data from all three oxygen-cycles and have found no significant differences. In fact, the strong correlations between dOE-MRI maps from each of the individual cycles of the gas challenge (Figure 5.9) show that it is technically feasible to assess tissue oxygenation within 6 minutes. Performing this analysis again with three-fold (Figure 5.9) and six-fold (Section 5.5.6) temporally under-sampled data suggests that there is sufficient SNR to successfully extract the oxygen responsive component with even a subset of the data. Though we have shown that there is sufficient SNR to undersample and/or interleave, this is only applicable to the coil we are using, at a particular field strength and in a particular tumour model. It would be prudent for investigators to explore the limitations of undersampling in other situations by initially acquiring the full dataset in a pilot experiment and subsequently analyzing subsets of it to evaluate whether there is sufficient SNR.

dOE-MRI offers a versatile technique where the duration of the cycles and gas challenge, temporal resolution and desired signal-to-noise can be modified based on the imaging objectives, which could include investigating intermittent perfusion or intervention-mediated changes in the tumour microenvironment. Of note, supplying excess oxygen to hypoxic tumour cells over time has the potential for increasing the baseline oxygen concentration, effectively reducing the hypoxic fraction and altering the tumour microenvironment [100]. This would result in voxels becoming more oxygen responsive over progressive oxygen cycles and would depend on the tumour characteristics as well as the duration of the oxygen challenge. This was not observed on the time scales in our study when using ICA to extract changes in T<sub>1</sub>W signal intensity just due to the gas challenge. Should it arise in other contexts it could possibly be mitigated by extending the air-breathing part of the cycle, or by extracting that as a separate component using ICA. The potential for creating a hyperoxia steady state by modulating oxygen duration is discussed further by Losert et al. [118].

Depending on the application of dOE-MRI, quantitative O<sub>2</sub>-positive and O<sub>2</sub>-negative fractions can be obtained from dOE-MRI maps as shown in this study, by deploying group ICA techniques [119], or setting significance thresholds using a t-test [120] and computing z-scores [121]. In a promising study, White et al. has shown that OE-MRI may be very relevant in developing prognostic factors to predict tumour response to hypofractionation by stratifying tumours that may benefit from oxygen breathing during irradiation [110]. Featherstone et al. have recently explored pre-clinical datasets using feature-extraction and clustering analysis and this may prove fruitful in understanding the behavior of subregions within a tumour microenvironment [122]. Future work to evaluate the utility of dOE-MRI will ultimately depend on its context-dependent validation as a relevant measure of tumour hypoxia to dynamically characterize the clinically relevant oxygen status of tumours, relating this information to treatment sensitivities and outcomes.

## 5.7 Conclusions

In this study we extend existing oxygen-enhanced MRI techniques by adding a cycling element to the respiratory challenge and using a blind-source separation

signal processing technique (ICA) to extract the oxygen responsive component and responding voxels. In the following chapters, we advance development and application of the technique and further refine it. In chapter 6 we attempt to validate dOE-MRI measurements *in vivo* using pimonidazole, a histological tumour hypoxia marker. To further explore the oxygen dynamics in tumours we also characterized the oxygen replenishment curve as originally proposed by Losert et al. in the brain [118]. In chapter 7 we deploy the technique to assess tumour oxygenation changes following treatment with bevacizumab, an antiangiogenic agent.

# Chapter 6

## Validation of oxygen-enhanced MRI in animals

### 6.1 Introduction

Recently our group has proposed a new technique,dOE-MRI to assess tumour oxygenation in vivo using MRI [3]. In this chapter we first extend the technique to characterize the extracted oxygen enhancing component used in DCE-US experiments. This model is then fit to the extracted ICA components to assess the feasibility of using the fit parameters as biomarkers of oxygen response. Finally compare dOE-MRI maps of tumour xenografts to slice-matched histological sections.

#### 6.1.1 Theory: Modelling oxygen response

A vascular network is a collection of multiple vessels including large arteries feeding smaller arterioles that ultimately deliver oxygen and nutrients to tissue via capillaries. This complex vascular tree is modelled by assuming a fractal branching geometry with the distribution of vessel sizes and flow rates given by a lognormal velocity distribution [123]:

$$P(v) = \frac{1}{\sigma_f \sqrt{2\pi}} \cdot \frac{1}{v} \cdot \exp\left(-\frac{1}{2} \left(\frac{\ln(v) - u_f}{\sigma_f}\right)^2\right) \quad (6.1)$$

Where  $P(v)$  is the probability density function of the velocity  $v$ ,  $\mu_f$  and  $\sigma_f$  are the mean and standard deviation of the distribution for the normally distributed random variable  $\ln(v)$ . The mean and standard deviation of a lognormal distribution are known quantities,

$$\text{Mean}(v) = \exp\left(\mu_f + \frac{\sigma_f^2}{2}\right) \quad (6.2)$$

$$\text{Var}(v) = \exp(2\mu_f + \sigma_f^2) \cdot (\exp(\sigma_f^2) - 1) \quad (6.3)$$

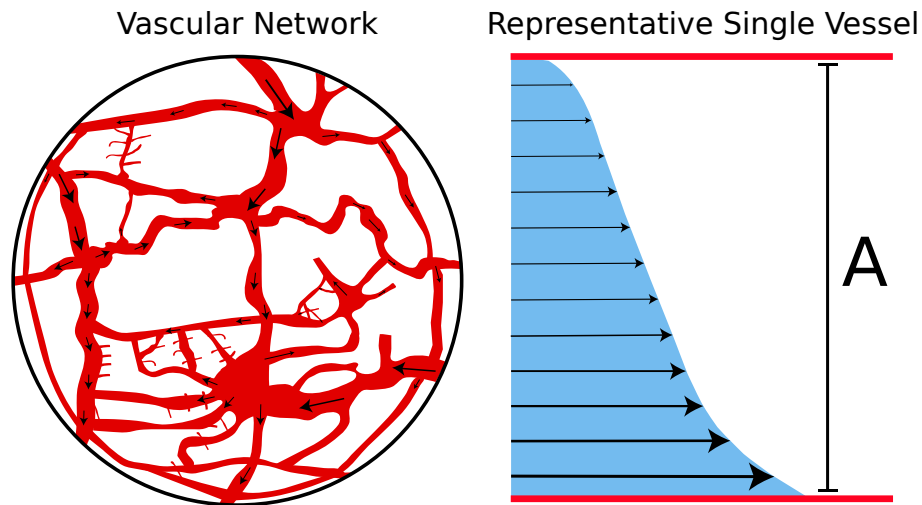


**Figure 6.1:** Schematic representation of the complex vascular network (left) with multiple velocity profiles (arrows) and its equivalent representation as a single vessel with a distribution of flow profiles (right). The distribution of velocity profiles of the representative single vessel is the lognormal distribution. Schematic representation re-created from Hud-  
son et al. [9].

Figure 6.1 shows a schematic of the vascular network modelled as a representative single vessel with a lognormal distribution of velocity profiles. Therefore the flow function for a vascular network is given by,

$$F(z,t) = \frac{A}{2} \cdot \text{erfc} \left( \frac{\ln(z/t) - \mu_f}{\sigma_f \sqrt{2}} \right) \quad (6.4)$$

Where A is defined as the total vascular area, z represents the spatial displacement of oxygen through the blood stream,  $\mu_f$  is the mean velocity and  $\sigma_f$  is the standard deviation of the velocity distributions. The velocity  $v$  was transformed for convenience to  $z/t$  to facilitate integration over the slice thickness  $z$ .

This lognormal flow profile model has been used to describe the replenishment of microbubbles injected into the blood stream in DCE-US [9]. The generalized representation of the replenishment time-intensity signal requires two components: an ultrasound beam-specific profile that is weighted in the z-direction due to a non-uniform slice profile and the flow profile. The expression is,

$$S(t) = \int_V B(x,y,z) \cdot F(x,y,z,t) \cdot dV \quad (6.5)$$

where  $B(x,y,z) = 1$  in MRI because of relatively uniform slice profiles. Integrating over the imaging plane ( $x,y$ ) and assuming a slice thickness of 1mm ( $z$ ), the final model for fitting dOE-MRI data becomes,

$$S(t) = \left[ \frac{A}{2} \left( z \text{erfc} \left( \frac{\ln(z/t) - \mu_f}{\sqrt{2}\sigma_f} \right) - te^{\sigma_f^2/2 + \mu_f} \text{erf} \left( \frac{\sigma_f^2 + \mu_f - \log(z/t)}{\sqrt{2}\sigma_f} \right) \right) \right]_{z=0}^{z=1mm} \quad (6.6)$$

Where A is defined as the total vascular area,  $\mu_f$  is the mean velocity and  $\sigma_f$  is the standard deviation of the velocity distributions. Since this is a generalized model that relies solely on the lognormal flow profiles of blood vessels, it is also applicable for dOE-MRI data. Excess inhaled oxygen that dissolves in the plasma acts as a contrast agent that enters the imaging plane. The model makes no assumption about the type of contrast agent, mechanism of enhancement, nor kinetics of the agent in describing the “replenishment” of signal so it was applied to a portion of the ICA-extracted oxygen-enhancing component.

## 6.2 Methods

### 6.2.1 Animals

Female NRG (NOD rag gamma) mice were implanted with murine squamous cell carcinoma SCCVII tumours ( $5 \times 10^5$  cells in 50  $\mu\text{l}$  serum-free media; cells provided by Dr. J Evans) or with human colorectal carcinoma HCT-116, human ovarian carcinoma SKOV3 or human breast carcinoma BT-474 tumours (each as  $10 \times 10^6$  cells in 50  $\mu\text{l}$  serum-free media; cell lines obtained from the American Type Culture Collection) and were imaged when the largest tumour diameters reached approximately 8-10 mm. All mice were injected with 60 mg/kg pimonidazole hydrochloride (HypoxyProbe) 30-min prior to imaging to label hypoxic cells and were euthanized within 15-min of imaging completion. Mice were anaesthetized with isoflurane using 1.5-2.0% isoflurane for the duration of MR imaging sessions until euthanasia, and were positioned supine on the custom surface coil apparatus. Throughout the imaging session, a small animal monitoring system (SA Instruments Inc., Stony Brook, NY, USA) was used to monitor respiration rate, varying between 80-100 breaths per minute, and body temperature, maintained at  $36.8 \pm 0.5^\circ\text{C}$  using a continuous airflow heater. Tumours were embedded and frozen in optimum cutting temperature medium (OCT; Tissue-TEK) with their largest diameter 8-10 mm.

### 6.2.2 Immunohistochemistry

Co-planar MRI slices and histological sections were obtained by imaging perpendicular to the longest tumour axis in MRI and serial-step 10  $\mu\text{m}$  cryosections were cut at 0.5-mm intervals in the same plane. Slides were then fixed in acetone-methanol for 10-min and whole sections were immunohistochemically stained [124] for CD31 (visualized using secondaries labeled with Alexa 647nm) to label blood vessels, and for pimonidazole (HypoxyProbe-1; visualized using secondary labeled with Alexa 546nm) to label hypoxic cells. Sections were then stained using Hoechst 33342 (bisbenzimide) to label all cell nuclei. Whole-tumour sections were imaged using a robotic fluorescence microscope (Zeiss Axioimager Z1), a cooled, monochrome CCD camera (Retiga 4000R; QImaging), a motorized

slide loader and x-y stage (Ludl Electronic Products) and customized ImageJ software [60]. Adjacent microscope fields of view were tiled such that images of entire tumour cryosections were captured at a resolution of  $1.5 \mu\text{m}/\text{pixel}$ . Using anatomical landmarks and accumulated thicknesses of serial-step sections as estimates of distances from the edges of whole tumours, sections were chosen to match the MR slices. ImageJ and user-supplied algorithms were used to super impose digital images which were then manually cropped to tumour tissue boundaries with staining artifacts removed. A threshold was applied to images to identify positive pimonidazole staining, and the number of positive pixels was determined as a percentage of the total number of pixels in the tumour image. Overlaid greyscale images were converted to false colour for visualization with pimonidazole as green and CD31 as magenta.

### **6.2.3 MR Imaging**

As previously described in Section 5.4.2.

### **6.2.4 dOE-MRI Analysis**

As previously described in Section 5.4.3.

### **6.2.5 Model Fitting**

Equation 6.6 was fit to the first 100 seconds of the ICA component trace after oxygen was first delivered to the mouse. Model fitting was done with the LMFIT package [125] using the Levenberg-Marquardt method. A free fit parameter was added corresponding to a vertical offset to account for the ICA component starting below 0. For each fit, three parameters describe the shape of the oxygen response:  $A$  (vascular area),  $\mu_f$  (mean velocity) and  $\sigma_f$  (standard deviation) of the velocity distributions. A sample fit using equation 6.6 is shown in Figure 6.2.

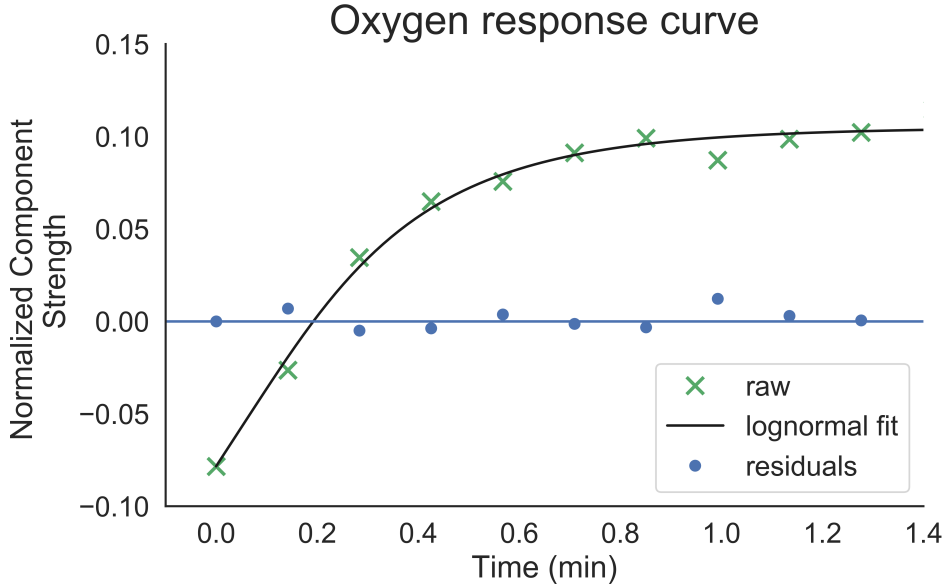


**Figure 6.2:** Fit of equation 6.6 to an oxygen response curve with the residuals plotted along the x-axis for each point. For this fit,  $A = 0.18$ ,  $v_f = 0.66\text{mm/s}$ , and  $\sigma_f = 0.58\text{mm/s}$ .

## 6.3 Results

### 6.3.1 ICA enabled dOE-MRI detects variable oxygenation in a range of tumour models

Tumours of human and murine origin and comprising a variety of tumour microenvironments were imaged, including fast growing, highly vascularized murine squamous cell (SCCVII) and human ovarian carcinomas (SKOV3), slower growing and well vascularized human breast cancer (BT-474), as well as a relatively fast growing but more poorly vascularized human colon colorectal carcinoma (HCT-116). The inter-model heterogeneity of the tumours is reflected in the mean fraction of negative voxels in the dOE-MRI maps, which were  $46 \pm 6\%$  for BT-474,  $36 \pm 3\%$  for HCT-116,  $31 \pm 5\%$  for SCCVII, and  $14 \pm 4\%$  for SKOV3 tumours. Considerable intra-tumour heterogeneity is also observed within some models, particularly the BT474. dOE-MRI maps representing the mean fraction of negative voxels are

shown for each tumour type in Figure 6.3.

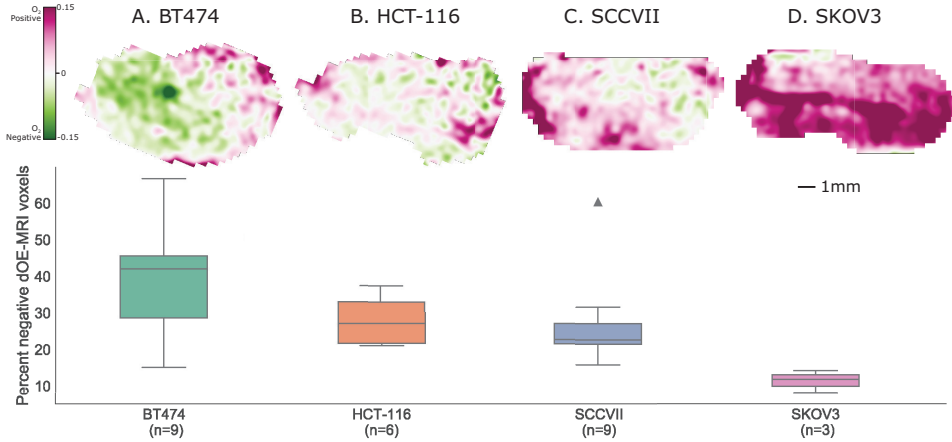


**Figure 6.3:** Top: dOE-MRI maps for four tumour models HCT-116, BT-474, SCCVII, and SKOV3 are shown. Chosen slices are representative of the mean percent negative dOE-MRI fraction for the respective tumour model. Bottom: The box-whisker plot shows the quartiles of percent negative dOE-MRI voxels for all imaged tumours. Figure reused with permission from Wiley and Sons.

### 6.3.2 Vascular area $A$ and mean velocity $v_f$ do not vary across tumour models, but $\sigma_f$ differentiates between tumours

Equation 6.6 was fit to the oxygen response kinetics for three tumour models (SCCVII, HCT-116, and BT474). Figure 6.4 shows the raw data and the fit for each animal. Group averages for each of the three parameters  $A$ ,  $v_f$  and  $\sigma_f$  are shown in box plots. The parameter  $\sigma_f$  discriminated between tumour types in this analysis and  $\sigma_f$  for SCCVII tumours ( $\sigma_f = 0.30 \pm 0.09$  mm/s) was statistically significantly lower than the HCT-116 tumours ( $\sigma_f = 0.52 \pm 0.12$  mm/s;  $p = 0.047$ ) as well as the BT474 tumours ( $\sigma_f = 0.76 \pm 0.19$  mm/s;  $p = 0.044$ ). The effect size for both comparisons was quite small: Hedge's  $g = 0.05$  for SCCVII vs. HCT-116 tumours and  $g = 0.02$  for SCCVII vs. BT474. No significant difference was found when comparing  $\sigma_f$  of HCT-116 and BT474 tumours. High intratumour variability was present in all tumours, but particularly in the BT474 tumour models. The SKOV3 tumours were not considered as part of this analysis due to low sample size ( $N=3$ ).

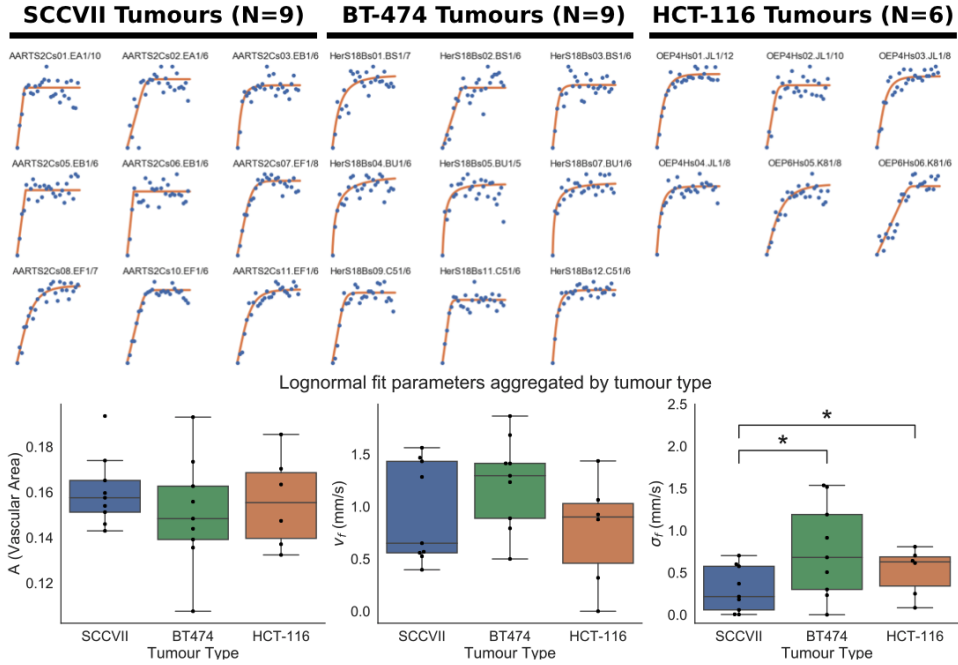


**Figure 6.4:** Top: Individual fits to the oxygen response curve for each animal and tumour type. Bottom: Box plots showing the median value and quartiles for  $A$ ,  $v_f$ , and  $\sigma_f$  across the three tumour models.

### 6.3.3 dOE-MRI maps correspond to matched histology sections

Tumour tissue cryosections obtained to match MR imaging slices were stained for vasculature (CD31) and regions of pimonidazole-labeled hypoxia and are compared side-by-side; Figures 6.6 and 6.7 provide five examples for each of SCCVII and HCT-116 tumour models for detailed review. Generally, in corresponding dOE-MRI maps for both tumour models O<sub>2</sub>-positive voxels align with the most oxygenated regions of histology sections, where pimonidazole labeling is absent, however many areas of mismatch are also observed. More consistent is that O<sub>2</sub>-positive voxels do not typically correspond to tissues identified as hypoxic in the histology sections (i.e. labeled with pimonidazole). In general, the more necrotic HCT-116 tumours have fewer O<sub>2</sub>-positive regions and significantly more O<sub>2</sub>-negative regions in the dOE-MRI maps, compared to the SCCVII tumours that have no necrosis. Pimonidazole labeling is heterogeneously dispersed within re-

gions of viable tissue containing tumour blood vessels for both SCCVII tumours, Figure 6.6, and HCT-116 tumours, which typically have greater amounts of necrosis, Figure 6.7. Figure 6.5 shows the fraction of negative dOE-MRI voxels correlated with the histological hypoxic fraction. For SCCVII tumours ( $n=9$ ) there was good correlation (Pearson's  $r = 0.76$ ) when using all tumours but it is important to note that one particular tumour had a much higher histological hypoxic and negative dOE-MRI voxel fraction. Excluding this tumour and its three slices, the correlation dropped to  $r = 0.14$ . The correlation in the HCT-116 tumours ( $n=6$ ) was similarly poor, with  $r = 0.037$ .

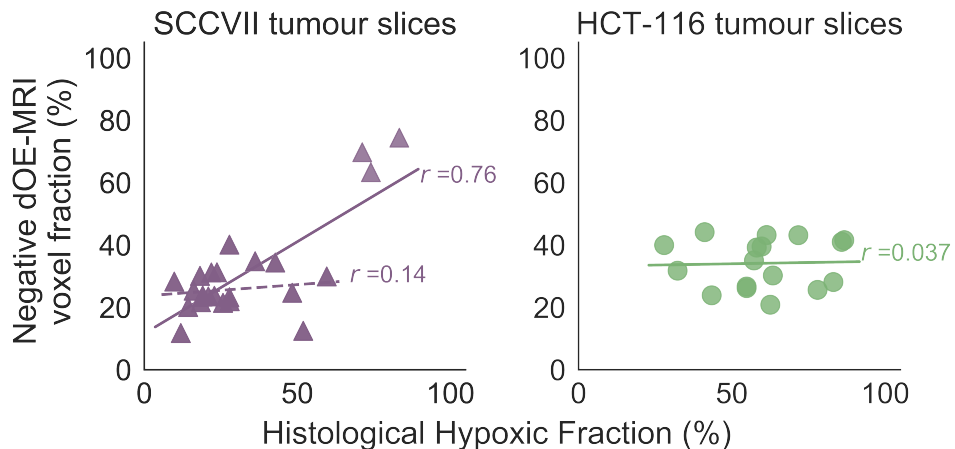


**Figure 6.5:** The proportion of negative dynamic oxygen-enhanced MRI (dOE-MRI) voxels is plotted against the histological hypoxic fractions with Pearson's  $r = 0.76$  for SCCVII tumours ( $r = 0.14$  after excluding tumour with high hypoxic fraction) and  $r = 0.037$  for HCT-116 tumours. Each point is a slice average. Figure reused with permission from Wiley and Sons.

## 6.4 Discussion

Using the dOE-MRI technique, we found that an oxygen-enhancing component was extracted successfully in all imaged animals across a range of tumour models and environments (Figure 6.3). In this study we also modelled the oxygen response curves in the tumour vasculature by deploying models developed in DCE-US and

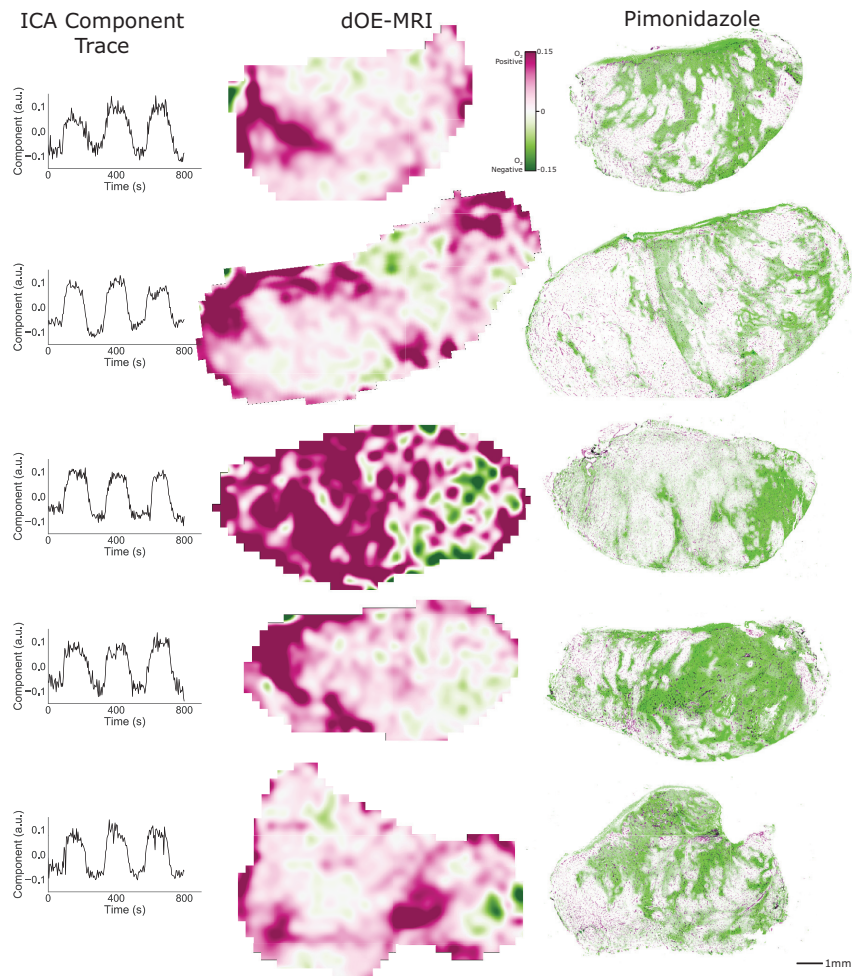


**Figure 6.6:** SCCVII murine tumours with slice-matched histological images depicting pimonidazole-labeled hypoxia (green) and CD31-stained vasculature (purple) are shown next to the dOE-MRI parameter maps similarly colored with O<sub>2</sub>-positive (purple) and O<sub>2</sub>-negative (green) areas. Corresponding ICA extracted components are also shown. Figure reused with permission from Wiley and Sons.

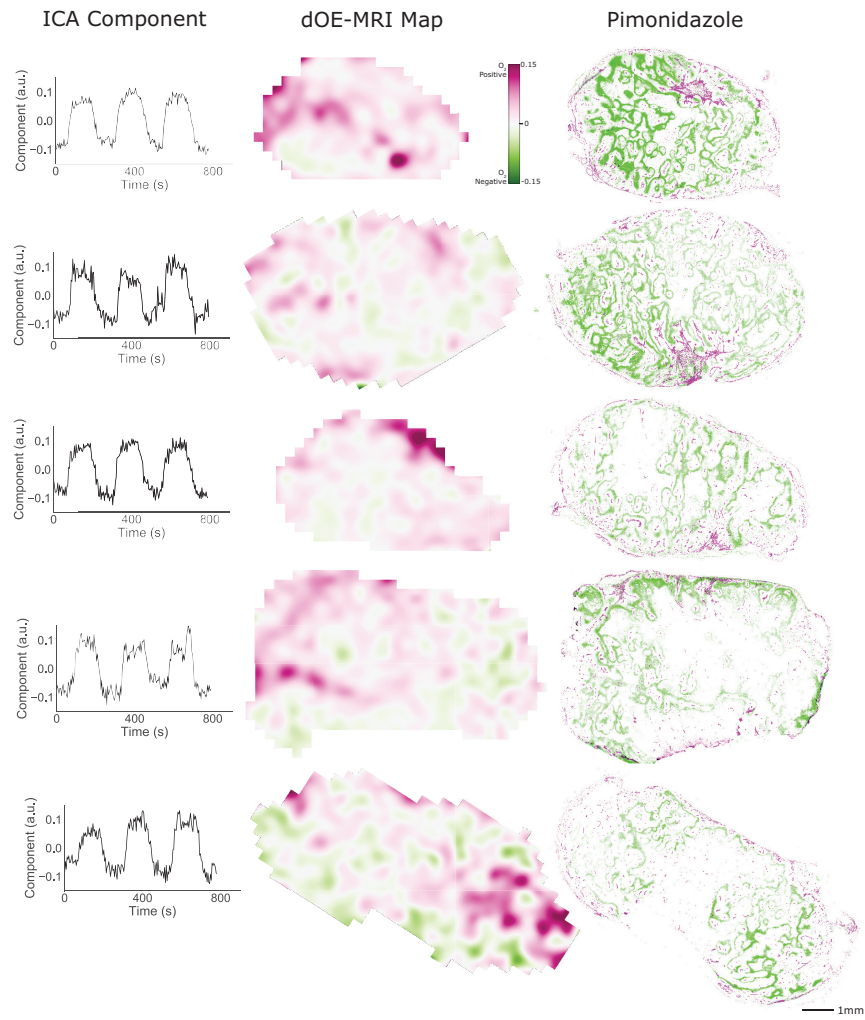


**Figure 6.7:** HCT-116 human colorectal xenografts with slice-matched histological images depicting pimonidazole-labeled hypoxia (green) and CD31-stained vasculature (purple) are shown next to the dOE-MRI parameter maps similarly colored with  $O_2$ -positive (purple) and  $O_2$ -negative (green) areas. Corresponding ICA extracted components are also shown. Figure reused with permission from Wiley and Sons.

adapting them for dOE-MRI. Fitting equation 6.6 to the oxygen response curves results in three physiologically relevant parameters though their applicability with oxygen as a contrast agent has not yet been established. Additional work is needed to explore how interpretation of these parameters may change when the contrast agent is intravascular. Nevertheless, a phenomenological fit of this model to our data provides interesting insights and use of the model over a standard exponential function is supported by the Akaike information criterion (data not shown). Unsurprisingly, the vascular area  $A$  and the mean velocity  $v_f$  do not appear to vary between the three tumour models studied(Figure 6.4). The third parameter  $\sigma_f$  is the standard deviation of the velocity distribution and is related to the structural organization and morphology of the vascular network [9]. Thus, we hypothesized that the oxygen response curves and in particular,  $\sigma_f$  may capture information about the vascular organization in different tumour models. The SCCVII tumour is a very aggressive and fast growing tumour [126], which implies a chaotic vascular network with a low degree of fractality (propensity to branch in a fractal pattern with large arteries branching to smaller arterioles, leading to extremely small capillaries). This behaviour would result in a narrow range of vessel sizes and velocity profiles in our lognormal velocity profile, and manifests in a low  $\sigma_f$  value for SC-CVII tumours relative to the other tumour lines. While only  $\sigma_f$  appears to be useful in delineating tumour models,  $v_f$  and  $A$  may be useful metrics to quantify the oxygen response curves of tumours after drug interventions.

A limitation of OE-MRI is the difficulty in interpreting areas that do not show a reduction in  $T_1$  as they may be either dead tissues that are *unperfused and not oxygenated* or living, viable tissues that are *perfused but not oxygenated* due to poor oxygen content of the supplying vessels. The latter population are of greater interest to the oncology community as it is these hypoxic but viable cells that have significant influence on treatment outcomes [127]. Though the dOE-MRI technique presented here did not successfully correlate with histological hypoxic fractions, there is promise in the technique to map oxygenation in tumours in the absence of necrosis (Figure 6.5). Additionally, it is challenging to compare to *in vivo* measures of oxygenation with pimonidazole staining intensity. Further work is needed to refine the techniques so that dOE-MRI measures better correlate with histological indices of hypoxia. A quantitative comparison in the HCT-116 tumour line

showed poorer association with dOE-MRI oxygenation status likely attributable to the much higher amounts of necrosis typical of the HCT-116 model relative to SCCVII (Figs. 6.6 and 6.7). Mitigations to this limitation have been explored elsewhere and generally require a perfusion mask or  $T_2^*$  - either technique can be added to the method proposed here to exclude necrosis and further improve sensitivity of the technique.

Application of existing OE-MRI techniques across a range of tumour models with varying perfusion characteristics has yielded mixed success without masking for perfused tissue. For instance, O'Connor reported that in the highly perfused 786-0-R tumour lines, 85-96% of all imaged tumour voxels were deemed to be oxygen-enhancing [99]. In those tumours, there was a good correlation between histological hypoxic fraction and oxygen refractory voxels. However, in the more weakly perfused SW620 tumours where only 76% of the voxels are oxygen-enhancing, there were no significant correlations with the histological hypoxic fraction. These issues were resolved by combining OE-MRI with DCE-MRI as a perfusion mask to select only perfused voxels for oxygenation assessment, thereby distinguishing between the viable hypoxic environment and necrotic dead tissues and improving the specificity and sensitivity of OE-MRI data. Using an IAUGC<sub>60</sub> map from DCE-MRI as a mask to obtain Oxy-R fractions O'Connor et al. showed good correlation with the histological hypoxic fraction [99]. In more recent work, Little et al. showed oxygen enhancement in tumours with a histological hypoxic fraction as high as 43% [108] and this translated very well to a study of six renal cell carcinoma patients. Linnik et al. reported excellent correlation between percentage of “negative AUC<sub>OE</sub>” ( $O_2$ -negative) voxels and percentage of hypoxic areas in the highly vascular preclinical U87MG tumour xenografts [100]. A second approach for differentiating between viable but hypoxic regions and unperfused dead tissues, is to combine OE-MRI with  $T_2^*W$  acquisition and the BOLD effect to classify regions [108–110, 128, 129] that show both effects. Excess oxygen in the blood will induce changes in Hb saturation, which alter the T2\* resulting in a robust measure of areas with functioning vasculature. Conceivably, the saved acquisition time achieved with under-sampling T<sub>1</sub>W dOE-MRI suggests that  $T_2^*W$  images could also be acquired to concurrently assess the blood oxygen level dependent (BOLD) response.

Within the relatively short 14-minute imaging time, both the HCT-116 and SC-CVII tumours show only minor changes in the oxygenation maps between cycles (Figure 5.7). In longer imaging sessions, or during administration of an intervention, these same tumours may exhibit varying oxygenation patterns between cycles. Periods of oxygen-starvation and re-oxygenation in tumours have been termed intermittent hypoxia and can arise due to temporary vessel occlusions [92, 94]. Recent work on measuring intermittent hypoxia in patients using  $R_2^*$  [130] shows that interest in this phenomenon continues but the importance of intermittent hypoxia in tumours is unclear largely due to poor availability of techniques to measure it in the clinic [93]. The relatively short imaging time for dOE-MRI makes assessing temporal oxygenation changes possible within a timescale on the order of minutes by comparing correlation maps generated from sequential cycles.

Typically, histological validation of MR data is done by collapsing rich histology data into a single metric, such as a hypoxic fraction, with whole-tumour or single-slice average comparisons. While this is sometimes a useful validation approach, it may not reflect the highly heterogeneous patterns of hypoxia that are known to vary spatially and temporally, even within the same tumour, as well as between tumour types as highlighted in Figures 6.5-6.7. Further complications are encountered with respect to validation of tools to assess hypoxia considering that hypoxia is not simply a binary metric. Instead, tumour oxygenation exists as a spectrum beginning with some tissues that may be normoxic, at levels similar to neighbouring normal tissues of origin, and can continue decreasing through levels of hypoxia to near anoxia where cells are still viable but are no longer able to proliferate. Eventually cells die in the absence of oxygen, and when this occurs in large numbers there can be significant regions of necrosis in solid tumours. A range of oxygenation levels are likely to be present in the highly heterogeneous microenvironments of all solid tumours, but what is of interest to the oncology community is *clinically relevant* hypoxia [96]. This refers to measurable tumour oxygenation levels that are biomarkers of physiologically meaningful phenomena, including patient prognosis or tumour sensitivity to treatments, such as immunotherapy or radiotherapy. The relevant oxygenation status for any biomarker of interest may include levels spanning from moderate to severely hypoxic. Pimonidazole has been demonstrated as a clinically relevant marker of hypoxia, but poor or inconsistent

correlation with pimonidazole, as we have seen in our imaged tumours, does not exclude other measures of tumour oxygenation from potential utility.

Measurable pimonidazole-adduct formation occurs when the O<sub>2</sub> tension in the vicinity drops below 10 mmHg [131] but in dOE-MRI, O<sub>2</sub>-positive voxels are extracted as excess oxygen dissolves in the plasma and interstitial tissue fluid to decrease T<sub>1</sub>. Voxels where T<sub>1</sub> has significantly increased has previously been correlated to poorly perfused regions and likely corresponds to hypoxic regions where the excess oxygen is picked up by deoxyhemoglobin molecules [100, 128, 132]. The exact mechanism for a T<sub>1</sub> increase as a result of oxygen inhalation has not yet been confirmed [100, 109], however, based on careful work of Silvennonin et al., characterizing behavior of T<sub>1</sub> in fresh bovine blood [133], we speculate the corresponding T<sub>1</sub>W signal decrease may arise due to the conversion of deoxyhemoglobin to hemoglobin in the perfused vessels of hypoxic regions . O<sub>2</sub>-positive regions in dOE-MRI maps are generally in good agreement with well perfused areas of histology images for both HCT-116 and SCCVII tumours, as shown in Figures 6.6 and 6.7. Voxels exhibiting signal reduction with the O<sub>2</sub> stimulus in dOE-MRI maps (O<sub>2</sub>-negative, green) typically correspond with histology (pimonidazole, green) but not all pimonidazole-labeled regions appear as O<sub>2</sub>-negative voxels. Similarly, CD31-stained tumour regions are not exclusively O<sub>2</sub>-positive in the dOE-MRI maps because not all tumour vessels are perfused. In fact many perfused blood vessels are only intermittently perfused and consequently, the measurement of hypoxia is time-sensitive. Mismatches between dOE-MRI and histology may be attributed in part to the different sensitivities and detection thresholds for measuring hypoxia and oxygenation in the dOE-MRI and histology-based modalities, as well as potential mismatch between the timing of pimonidazole-labeling and dOE-MRI data acquisition. A current limitation of validating dOE-MRI maps is that visual matching of purple regions in dOE-MRI maps and “non-green” regions in histology sections requires some mental gymnastics and a trained eye. Collapsing the rich spatial information to a tumour or slice mean is not an option so future work is needed to fully validate this relationship in a rigorous manner. A proposed experiment and analysis pipeline would require robust matching of MRI and histological sections followed by deformable image registration to map MRI regions onto histology sections with image re-sampling as needed. This would

permit microregional analyses and quantitative validation of dOE-MRI oxygenation maps accounting for spatial heterogeneity.

## 6.5 Conclusions

In this chapter, we compared dOE-MRI oxygenation with pimonidazole stained histology images and showed that O<sub>2</sub>-positive regions in dOE-MRI maps generally correspond to pimo-negative regions in histological sections. The versatility of the technique was apparent due to its applicability in multiple tumour models; though, the presence of large necrotic areas in tumours poses some challenges when comparing oxygenation status with pimonidazole staining. We also applied the lognormal velocity profile model from DCE-US to oxygen response curves obtained from ICA and dOE-MRI and the parameter  $\sigma_f$  is useful in quantifying the vascular morphology of tumours. dOE-MRI assesses tumour oxygenation fairly reliably *in vivo* and the next application is to see whether the technique is sensitive to oxygenation changes brought on by chemotherapies.

# **Chapter 7**

## **Applications of oxygen-enhanced MRI**

### **7.1 Preface**

A new term has been introduced in this chapter to compare what has previously been referred to as “dOE-MRI values”. The normalized component weighting factor value is now shortened to be NCWF.

### **7.2 Introduction**

Dynamic oxygen-enhanced MRI (dOE-MRI) has recently been proposed by our group to assess tumour oxygenation *in vivo* using MRI [3]. This technique measures T<sub>1</sub>-weighted changes in tissues in response to a cycling oxygen challenge, with the responsive signals detected using Independent Component Analysis (ICA). Briefly, oxygenation can be assessed *in vivo* by administering a simple gas challenge (switching between two-minute periods of medical air and 100% O<sub>2</sub>) during the dOE-MRI scan and then using ICA to extract the tissue response. ICA is a blind-source separation algorithm that separates multiple signal sources by maximizing statistical independence of individual components [116]. Various flavours of oxygen-enhanced MRI (OE-MRI) have been proposed but all essentially leverage the paramagnetic properties of inhaled oxygen. White et al. have

shown that OE-MRI may be very relevant in developing prognostic factors to predict tumour response to hypofractionation by stratifying tumours that may benefit from oxygen breathing during irradiation [110]. In this study, we apply dOE-MRI to mice bearing tumour xenografts to assess the effect of a common antiangiogenic agent. We hypothesized that dOE-MRI with group-ICA can detect Vascular endothelial growth factor (VEGF) ablation-induced changes to oxygenation of SC-CVII tumours 48 hours following treatment.

### 7.2.1 VEGF inhibition and bevacizumab

VEGF is a key regulator of angiogenesis as the VEGF molecule is rate-limiting in normal and pathological growth of blood vessels. Bevacizumab is a monoclonal antibody that binds VEGF and inhibits growth of blood vessels [134] and inhibits tumour growth. It is marketed for clinical use for tumours under the name Avastin<sup>©</sup> (Genentech Inc., California, USA) and its effects and outcomes have been widely reported [135–138]. Tumour xenografts receiving monoclonal antibodies to VEGF have consistently shown reductions in quantitative perfusion parameters from a variety of non-invasive imaging modalities including DCE-US [139], DCE-MRI [140], and micro PET [141]. For dynamic contrast-enhanced ultrasound (DCE-US), Wang et al. reported a significant reduction in peak enhancement, area under the curve, relative blood volume, and relative blood flow just 24 hours after a treatment of 10 mg/kg of bevacizumab [139]. Several dynamic contrast-enhanced MRI (DCE-MRI) animal and human studies have shown reductions in  $K^{trans}$ ,  $v_p$ , and  $v_e$  after administration of antiangiogenic agents, including bevacizumab [142]. Tumour growth delay data also clearly indicates that growth is slowed after treatment with bevacizumab [142] and other similar VEGF-inhibitors [30].

It is well established that after treatment with antiangiogenic agents, the normalized vasculature is characterized by a reduction in vessel permeability, tortuosity, greater coverage by pericytes and a more normal basement membrane [29]. These morphological changes often result in functional changes as well including decreased interstitial fluid pressure, increased tumour oxygenation, and improved delivery of nutrients (and drugs) [29]. Bevacizumab is an expensive drug with

many adverse effects [135] so selective targeting of patients that are most likely to benefit from it should reduce unnecessary toxicity of ineffective therapies and improve its overall cost-effectiveness [137]. In this study, we present an application of dOE-MRI to assess tumour oxygenation before and after treatment with bevacizumab.

## 7.3 Methods

### 7.3.1 Animals

Female NRG (non-obese diabetic rag gamma) mice were implanted with murine squamous cell carcinoma (SCCVII;  $5 \times 10^5$  cells in  $50 \mu\text{l}$  serum-free media; cells provided by Dr. J. Evans) in the dorsal subcutaneous region. Tumours were imaged when their largest diameters reached approximately 8-10 mm. All mice were injected with 60 mg/kg pimonidazole hydrochloride (HypoxiProbe) 30 min prior to imaging to label hypoxic cells and were euthanized within 15 min of imaging completion. Mice were anaesthetized with isoflurane using 1.5-2.0% isoflurane for the duration of MR imaging sessions until euthanasia, and were positioned supine on the custom surface coil apparatus. Throughout the imaging session, a small animal monitoring system (SA Instruments Inc., Stony Brook, NY, USA) was used to monitor respiration rate, varying between 80-100 breaths per minute, and body temperature, maintained at  $36.8 \pm 0.5^\circ\text{C}$  using a continuous airflow heater. Tumours were embedded and frozen in optimum cutting temperature medium (OCT; Tissue-TEK).

### 7.3.2 Immunohistochemistry

As previously described in Section 6.2.2.

### 7.3.3 MR Imaging

As previously described in Section 5.4.2. All scans were acquired with the same spatial resolution and geometry and an experienced operator outlined the tumour on each slice of the RARE image to construct the region of interest (ROI) for each animal and then transferred to all other scans. Tumour volumes were measured by

multiplying individual voxel volume ( $0.3 \times 0.3 \times 0.1 \text{ mm}^3$ ) and the count of total number of voxels included within the manually drawn ROI.

#### 7.3.4 dOE-MRI analysis

As previously described in Section 5.4.3. Briefly, in these dOE-MRI maps, voxels are coloured to indicate the amount by which a given pixel intensity time course is modulated by the oxygen-related component. To compare dOE-MRI maps between mice with different temporal resolutions, a scaling factor was applied as discussed previously (see section 5.5.8). Final normalized dOE-MRI maps were obtained by dividing each pixel of the component map for each animal with the mean signal-intensity over time of the corresponding pixel in the dOE-MRI scan. Mean normalized component weighting factor (NCWF) are reported as a marker for tumour oxygenation with high values indicating increased oxygenation while negative values suggest decreased oxygenation or increased levels of hypoxia. Mann-Whitney U non-parametric tests are used to assess the difference between experimental groups and Hedge's  $g$  was calculated to determine effect size when  $p < 0.05$ .

#### 7.3.5 Experiment Summaries

General methods common to both experiments have been described above, below are implementation details for each of the two separate experiments presented in this study.

##### **Experiment 1: Evaluating the utility of dOE-MRI to assess oxygenation improvements after anti-VEGF ablation therapy**

**Animals:** Seventeen (17) mice were implanted for this experiment with eight left untreated and nine mice treated with 5mg/kg mouse anti-VEGF antibody (B20-4.1.1, Genentech) 48 hours prior to imaging.

**MRI:** Axial dOE-MRI scans were acquired with 90 repetitions using a 2D FLASH based sequence with  $T_E/T_R=2.67/133$  ms, flip angle  $\alpha=40^\circ$ , 16 slices each 1mm thick, FOV of 3.84cm x 2.16 cm, encoding matrix of 128x72, and a temporal resolution of 9.6s for a total scan time of about 14 minutes.

## **Experiment 2: Assessing oxygenation changes in intramuscular and subcutaneous tumours Anti-VEGF ablation therapy in IM vs. SC tumours**

**Animals:** Thirteen (13) mice were used in this experiment. 3 mice were implanted with SCCVII in the dorsal subcutaneous (SC) region. 10 mice were implanted in both the dorsal subcutaneous (SC) as well as in the hind limb intramuscular (IM) region. To account for the accelerated rate of growth for tumours implanted intramuscularly, one-fifth of the cells were implanted IM ( $1 \times 10^5$  cells in  $50\mu\text{l}$  serum-free media). Separate ROIs were drawn on the  $T_2\text{W}$  images to outline both the SC and IM tumours. 5 mice were treated with 5mg/kg B20 24 hours prior to imaging and 8 were untreated controls.

**MRI:** Coronal images were acquired to enable simultaneous imaging of both tumours in the same field of view. All dOE-MRI scans were acquired using a 2D FLASH based sequence with  $\text{TE} = 2.67$  ms, spatial resolution  $0.3 \times 0.3 \times 1 \text{ mm}^3$  and flip angle  $\alpha = 40^\circ$ . To accommodate additional slices and image both tumours in the same scan while maintaining spatial resolution, not all imaging parameters in the dOE-MRI scan could be fixed. Table 7.1 summarizes the key differences in the acquisition parameters for all dOE-MRI sequences used in experiment 2.

Experiment	Mice	TR/ms	Slices	Repetitions	Temporal resolution (ms)
1	17	133	16	90	9.6
2	5	133	16	110	8.5
2	8	83	10	140	6.7

**Table 7.1:** Summary of scan parameters for the experiments used in this study.

## **7.4 Results**

### **7.4.1 Subcutaneously implanted SCCVII tumours treated with B20 are more responsive to oxygen than controls**

Visual inspection of dOE-MRI parameter maps in Figure 7.1 show that treatment of SCCVII tumours with the anti-angiogenic agent B20 resulted in an increased oxygenation compared to untreated controls. Tumours in this experiment were

treated 48 hours prior to imaging. Group differences are shown in Figure 7.2 as a standard box plot; Eight control tumours had a mean NCWF value of  $0.037 \pm 0.011$  and nine treated tumours had a mean of  $0.094 \pm 0.037$ . This difference was statistically significant (Mann-Whitney  $U = 11, p = 0.0092$ ) and the effect size was large with Hedge's  $g = 1.08$ . Considerable heterogeneity was observed between mice and within a single slice (Figure 7.1). A histogram of voxels within tumour ROIs for all mice is shown in Figure 7.2B.

#### **7.4.2 IM tumours have a higher baseline oxygenation level than SC tumours from the same cell line**

Tumours implanted in the hind limb (IM) received only 20% of the cells compared to the subcutaneous tumours to account for faster growth of IM tumours. Figure 7.3 shows no statistically significant difference in tumour volumes for any of the groups, control or treated, IM or SC. Across 10 animals and 23 tumours in total, the mean across all groups was  $V = 424 \pm 41mm^3$  (mean  $\pm$  standard error of the mean). dOE-MRI was applied to mice bearing both SC and IM tumours to evaluate whether tumour implant site affects baseline oxygenation. As shown in Figure 7.4, baseline NCWF values in IM tumours were significantly higher for IM tumours compared to SC tumours (Mann-Whitney  $U = 1.0, p = 0.003$ ). The effect size was large with Hedge's  $g = 1.38$ .

#### **7.4.3 Effects of B20 are dependent on the tumour microenvironment and baseline oxygenation**

To investigate whether the effects of antiangiogenic agents are dependent on different tumour microenvironments, mice were implanted with both IM and SC tumours. Tumours in this experiment were treated 24 hours prior to imaging. To ensure the SC tumours from mice with a double implant were similar to mice with only a single implant, three mice were implanted only with subcutaneous tumours. No differences were found (data not shown), so the SC tumours from this experiment were pooled together.

When comparing between SC baseline and treated groups, there was a statistically significant difference (Mann-Whitney  $U = 3.0, p = 0.007$ ) observed in mean

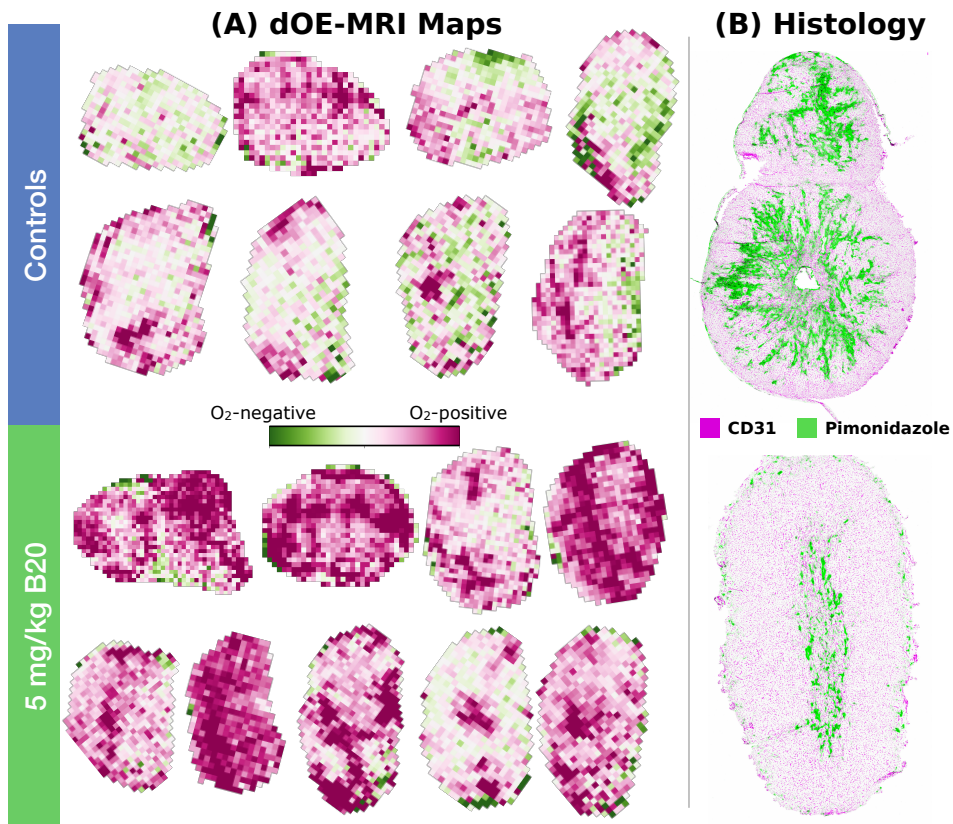


**Figure 7.1:** A) NCWF maps obtained from ICA (dOE-MRI maps) are shown for control tumours as well as those treated with 5mg/kg B20 and imaged 48 hours later. Of the 10-16 slices for each animal, a representative slice was chosen. As indicated by the distribution of purple voxels, control tumours show considerably less response to oxygen than the treated tumours. Additionally, regions marked in green are considered to be hypoxic; these regions were not prevalent in the treated tumours. B) A representative histology slice from a control and a treated tumour is shown stained with pimonidazole (green) and CD31 (purple).

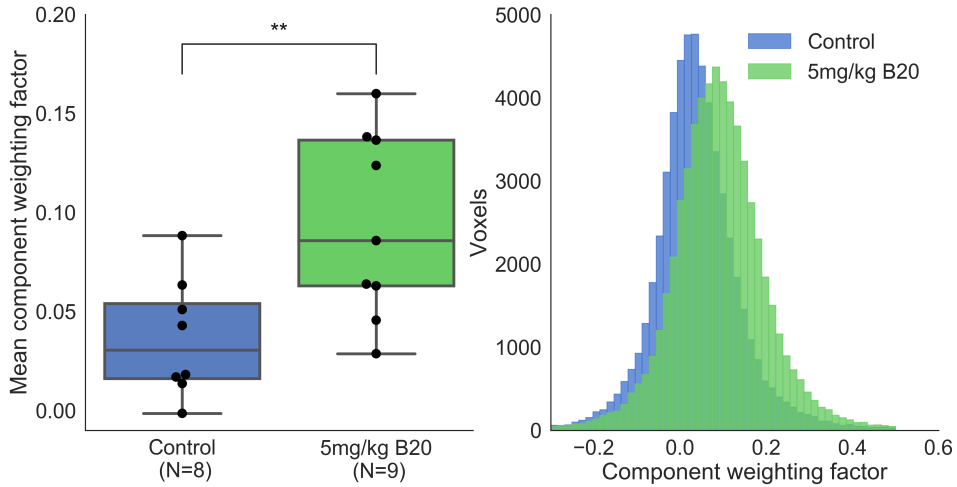


**Figure 7.2:** A) Group differences of the normalized mean NCWF are shown in a boxplot. Each dot represents the mean value of a mouse with the controls in blue and treated in green. The differences are statistically significant ( $p=0.0092$ ) with a large effect size (Hedge's  $g = 1.08$ ). B) Density distributions of all voxels shows treated tumours shifting towards increased responsiveness to delivered oxygen (higher NCWF).

NCWF values for control ( $0.073 \pm 0.009$ ) vs. B20-treated tumours ( $0.119 \pm 0.013$ ) with a large effect size: Hedge's  $g = 1.77$  (Figure 7.4). However, no measurable difference in oxygenation was observed for the IM tumours after B20 treatment (Mann-Whitney  $U = 11.0, p = 0.42$ ). Mean NCWF from B20-treated IM tumours was  $0.137 \pm 0.018$ , and control IM tumours was  $0.146 \pm 0.017$ . Histological images (Figure 7.5) also suggests that control IM tumours have significantly less pimonidazole staining compared to SC controls. Furthermore, reduction in pimonidazole staining between control and treated IM tumours is much lower compared to SC tumours. This provides clear evidence that the effects of B20 are dependent on the tumour microenvironment, and dOE-MRI is sensitive to these differences.

## 7.5 Discussion

Hypoxic tumour cells may arise due to proliferation of cancer cells outpacing the growth of new vasculature, increasing the separation between blood vessels and

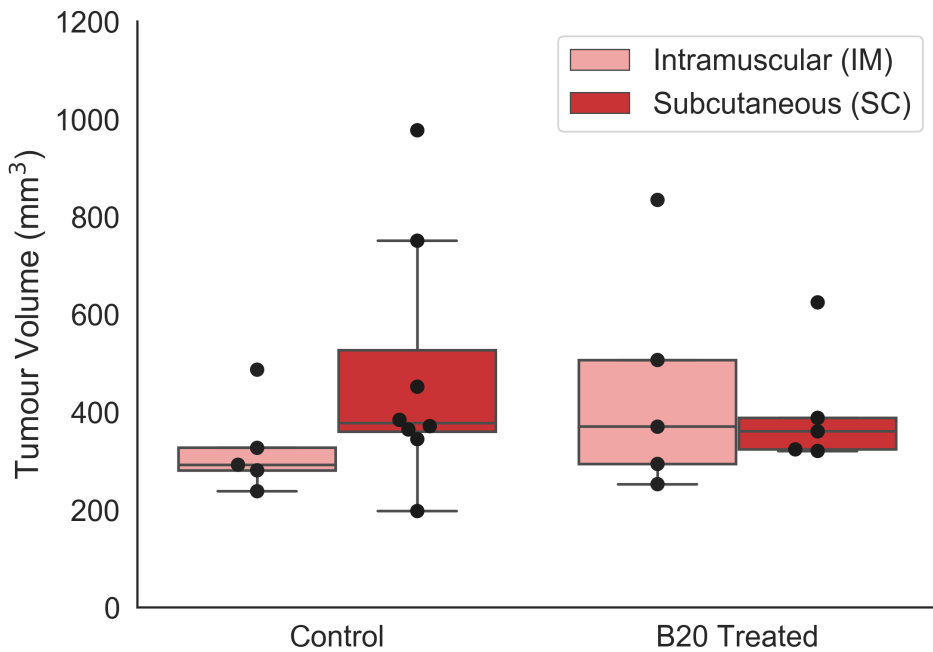


**Figure 7.3:** Calculated tumour volumes from each of the four groups is shown. There were no statistically significant differences in tumour volumes amongst any of the groups.

forcing cells beyond the diffusion distance of oxygen from the blood supply. An alternative route to hypoxia is the consequence of poor flow, which can result in hypoxic tumour tissue due to depleted oxygen supply in the flowing blood or due to intermittent flow of poorly formed vessels. Tumour microenvironments are dynamic and highly heterogeneous, with variable vascular function and patterns of hypoxia. However, the importance of hypoxia in tumours is well validated and undisputed; a meta-analysis of tumours from multiple origins found a consistent relationship between greater hypoxia in tumours and poorer outcomes with radiotherapy [96]. While many techniques exist for measuring hypoxia in tumours, none have become clinical routine mainly owing to their expense, poor sensitivity and specificity, limited availability or their invasive nature [143, 144]. For example, Eppendorf electrodes are sensitive and specific, and are a gold standard of measuring tissue hypoxia, but they are highly invasive, limited by sampling, and are not

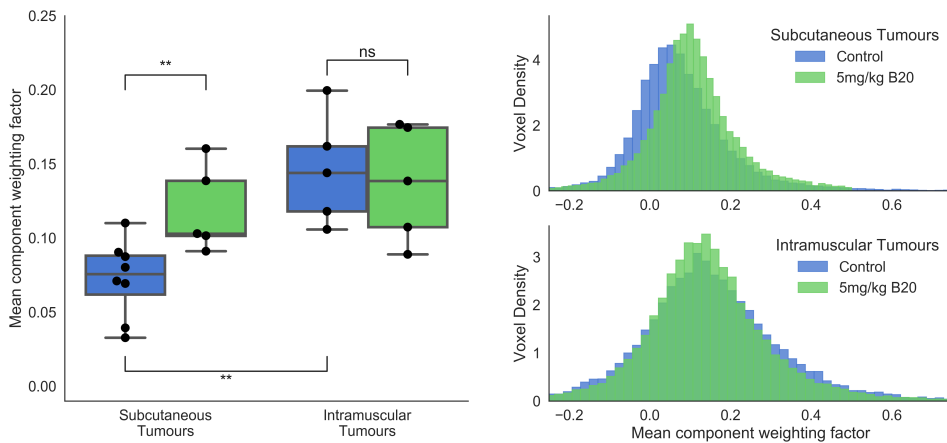


**Figure 7.4:** **A)** Boxplot with four groups, 5mg/kg B20 treated and control mice with both SC and IM tumours. Differences between control SC and IM tumours, as well as control SC and treated SC tumours are statistically significant (Mann-Whitney U test;  $p < 0.005$ , marked as \*\*). There was no significantly difference in treated and control IM tumours. **B)** Voxel density distributions of NCWF for SC (top) and IM (bottom) treated and control tumours. Density distribution (i.e. normalized histograms) are shown rather than voxel counts due to uneven group size. Note the shift of the IM control tumours towards a higher NCWF value.

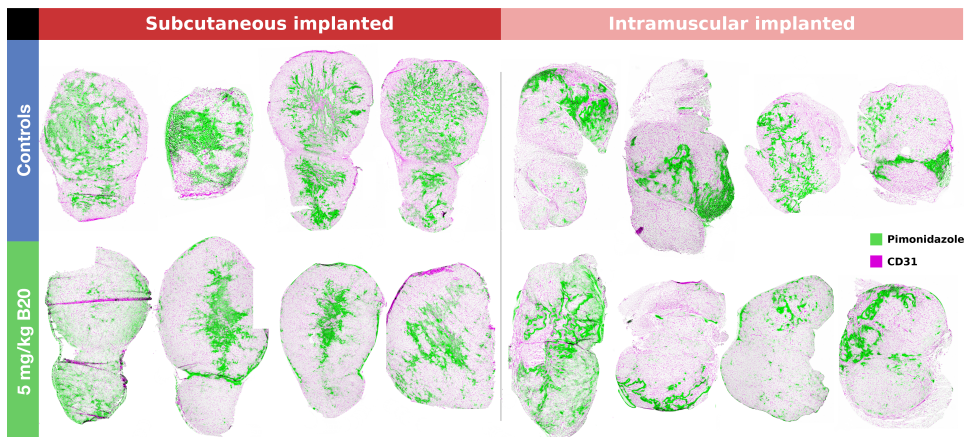


**Figure 7.5:** Representative histological sections from 16 total tumours of all four groups: 5mg/kg B20 treated and control mice with SC and IM tumours. Hypoxia marker pimonidazole staining is shown in green, and purple indicates the presence of blood vessels stained by CD31.

widely available. Patients in the ARCON (accelerated radiotherapy, carbogen and nicotinamide) trial with hypoxic tumours (assessed retroactively using pimonidazole labeling of biopsy samples) demonstrated a treatment benefit [145]. However, immunohistochemical analyses of markers of hypoxia such as pimonidazole are invasive and do not sample the entire tumour. A more widely applicable hypoxia-measuring tool that overcomes the availability, expense, invasiveness, sensitivity and specificity hurdles would be of high value for stratifying patients in hypoxia-targeted trials, prognostic imaging as well as for monitoring response to treatment.

In this study we have demonstrated the utility of dOE-MRI to assess tumour oxygenation changes after administration of B20. Though this is not the first report of tumour oxygenation improvements after antiangiogenic drug treatment using MRI methods, we provide clear evidence this change is measurable using only the switching of inhaled gas and no injectable contrast agents. Using electron paramagnetic resonance and an injectable paramagnetic tracer (triaryl methyl radical derivatives), Matsumoto et al. mapped increases in the partial pressure of oxygen in tumours after administration of the VEGF inhibiting antiangiogenic agent called sunitinib. Two to four days following antiangiogenic treatment with sunitinib, they reported a transient improvement in oxygenation [146]. Lemasson et al. obtained estimates of blood oxygen saturation using an ultrasmall super-paramagnetic iron oxide (USPIO) contrast agent in a rat gliosarcoma model. They reported that after sustained administration ( $>9$  consecutive days) of the maximum dose of sorafenib, oxygen saturation in treated tumours reduced compared to untreated control tumours [147]. In this case, the dose and treatment schedule resulted in excessive pruning of the tumour vasculature to the point where drug and nutrient delivery became limited and tumour oxygenation actually reduced [148]. In our experiments, with the dose (5 mg/kg) and treatment schedule (single administration 24 or 48 h prior to imaging), we expected a vascular normalization effect corresponding to an increase in oxygenation [148–150]. Despite heterogeneity in amount and levels of oxygen response in the SC tumours, we observed an overall increase in oxygenation after administering B20 (figures 7.1, 7.2, and 7.4).

In this study we provided evidence that the location of tumour cell implants has a large impact on the microenvironment of the resulting solid tumour. Tumour kinetics and responses to chemotherapies differ depending on the implant

site and the effect of tumour implantation site is often not considered when assessing drug effect using *in vivo* animal studies [151]. Hubbard et al. compared the tumours derived from the VX2 rabbit carcinoma line implanted intramuscularly and intra-abdominally and discovered animals with IM tumours had significantly higher levels of calcium compared to animals with intra-abdominal tumours [152]. This result was attributed to the differences in venous drainage of the two sites. In another example, Malave et al. studied the Lewis-lung carcinoma model and reported a lower implant success rate for tumours implanted in the flank compared to the foot pad, and a higher rate of metastatic nodules for tumours in the flank (indicating a reduced tumour-host immune response) [153]. Tumour implant site also alters growth kinetics and dramatically different tumour doubling times (in days) has been reported for implants in mouse tail (1.7), foot (1.6), chest (1.2), and leg (0.6) [154]. For the same amount of cells implanted, our experience is that IM tumours typically grow much faster, have a more stable vascular architecture, less hypoxia (pimo staining), and increased vessel density (CD31 %). We attempted to control for this growth rate by injecting fewer cells for the IM tumours. Our tumour volume measurements indicate there was no significant difference between the control IM and SC tumours despite the SC tumours implanted with 5 times the amount of cells implanted. We also showed that dOE-MRI can assess increased baseline oxygenation in control tumours when the tumour site is changed from the dorsal subcutaneous region to the hind limb: IM tumours have less pimonidazole staining compared to SC tumours (Figure 7.5). Ultimately we showed that following treatment of IM tumours with B20, no change in oxygenation was observed, likely because IM tumours were already well-oxygenated. It is important to note that our technique is not able to distinguish between increased oxygen concentration in the plasma (or interstitial tissue fluid) and increased blood volume. Both these effects will result in an increase of dissolved oxygen in the plasma and will look similar in dOE-MRI maps. To decouple these two effects, an alternative contrast mechanism (such as  $T_2^*$  or an exogenous contrast agent) is required.

To fully establish the utility of dOE-MRI to assess tumour oxygenation non-invasively using inhaled oxygen or air, several subsequent experiments should be conducted. Some ambiguities remain with a  $T_1$ -based dOE-MRI method as its reflection of dissolved  $O_2$  concentrations is complicated by complex, non-linear

relationships with hemoglobin saturation and its effects on  $T_2^*$ , and with vascular perfusion and blood flow that may confound interpretation of existing dOE-MRI signal. These are further complicated by the array of physiological possibilities that may be visualized by a change in  $T_1$ . In future development of this method, the impact of  $T_1$ -weighting should be explored to ensure effects of interventions are not manifesting due to changes in tumour microenvironment that alter  $T_1$ . A decrease in  $T_1$  suggests an oxygen-responsive area, while non-responding and negative-responding regions may represent a variety of physiologies. These areas may be completely unperfused and even necrotic, or they may be poorly perfused but viable, hypoxic tissues. Conversion of deoxygenated hemoglobin (present in hypoxic regions) to hemoglobin in the presence of oxygen results in a reduction of  $T_2$  and  $T_2^*$  but the  $T_1$  remains largely unchanged. Further exploration of intermediate regions (i.e. not hypoxic or well-oxygenated) using dOE-MRI and coupling it with BOLD-MRI is warranted to fully classify all areas of the tumour. An unexplored application of dOE-MRI is its potential to monitor treatment efficacy longitudinally as the contrast mechanism used is completely reversible. This opens up the possibility to do treatment interventions within a single imaging session with perfectly co-registered tumour volumes to allow for assessing oxygenation changes at the level of a single voxel. Nevertheless, dOE-MRI has tremendous potential for assessing tumour oxygenation as a non-invasive imaging method that is urgently needed in the clinic.

## 7.6 Conclusions

Through this work we have shown that subcutaneously implanted SCCVII tumours treated with B20 and imaged 48h later are more oxygenated than control tumours. Additionally, we have established dOE-MRI as a tool to assess baseline oxygenation level and demonstrated that IM tumours are significantly more oxygenated than SC tumours implanted in the same mice. Finally we provided evidence that location of the tumour implant site has a large effect on therapy outcome as the more oxygenated IM tumours did not respond to treatment with B20. It is our expectation that after further refinement and expansion, this technique will become accessible and available in the clinic to screen cancer patients prior to chemo- or ra-

diotherapy prescription, and be useful for developing new hypoxia-targeting drugs.

# **Chapter 8**

## **Future Work**

### **8.1 Introduction**

The work presented in this chapter provides a blueprint to continue the dOE-MRI project and explore several avenues of research. The level of maturity of each section varies and all attempts have been made to motivate and guide the reader through the methods, results, and their implications.

### **8.2 Group ICA**

One of the principal limitations of ICA is that it “does not naturally generalize to a method suitable for drawing inferences about groups of subjects” [119]. In this thesis, we developed a quantification method to mitigate this issue by comparing component weighting factor strength after normalization (Section 5.5.8). Calhoun et al., has reviewed several methods for analyzing multiple subjects within a cohort using ICA have been proposed [119]. The approach that is most relevant for the data collected for the experiments presented in this thesis (section 7.3.5) is spatial concatenation [155]. Briefly, cohort data for Group ICA was constructed by concatenating all 16 slices from the 17 subjects together in the z-dimension. Figure 8.1 compares Group ICA to the standard ICA technique described in Chapter 5. The same deflation-based FastICA (python package `scikit.learn v0.17.1`) was used to analyze the data. To ensure the cyclic behaviour of the  $T_1$  weighted

signal intensity corresponding to the gas challenge appeared in only one component, the number of independent components was set to 9. Application of ICA to the spatially concatenated data produced a single oxygen-enhancing component that matched the temporal pattern of the gas cycling paradigm in all 17 animals (Figure 8.2). This component appears to be smoother than typical extracted oxygen enhancing components because it represents the group response rather than the individual features that exist in each mouse that responds somewhat differently.

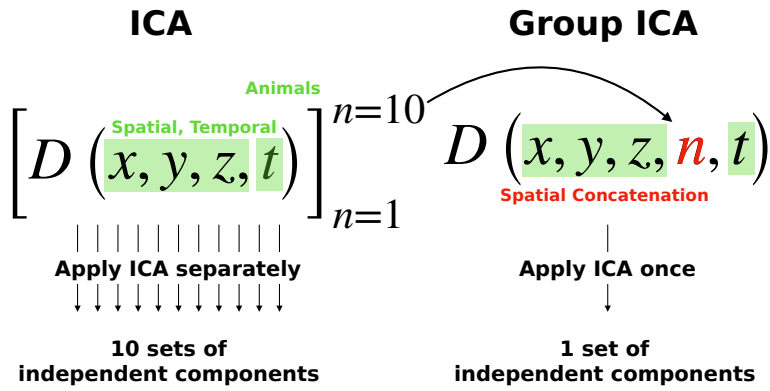


**Figure 8.1:** Comparison of the standard ICA technique and Group ICA. The main difference is in the pre-processing of the MRI data comprising spatial coordinates ( $x, y, z$ ) and temporal information ( $t$ ). Group ICA datasets are prepared by spatially concatenating all animals together ( $n$ ). The output of the ICA techniques also differs: in standard ICA each application produces a set of independent components whereas in Group ICA only a single set of independent components is produced.

Upon selection of the single oxygen enhancing component, reshaping the resultant weighting-factor maps to the original matrix size provided inter-subject comparable data. Final normalized dOE-MRI maps were obtained by dividing each pixel of the component map for each animal with the mean signal-intensity over time of the corresponding pixel in the dOE-MRI scan. Corresponding dOE-MRI are comparable to the methods presented in Chapter 7 and conclusions of the B20 effect still hold with this analysis method. One major disadvantage of applying ICA only once to multiple animals is that the extracted component averages out any individual features.

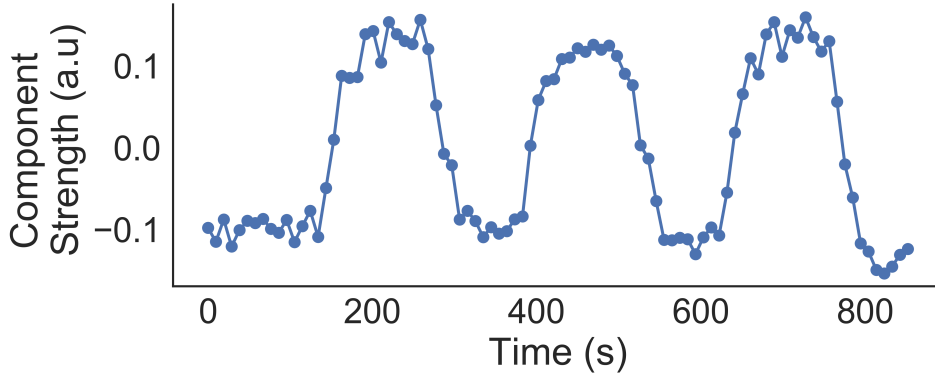


**Figure 8.2:** Extracted oxygen enhancing component from ICA applied to the spatially concatenated cohort data.

### 8.3 Further investigation of the characteristic oxygen response curve

In this thesis a limited number of tumours models were studied (SCCVII, BT-474, and HCT-116) so it was difficult to generalize whether modelling of the oxygen response curve is characteristic of the tumour environment or model. In section 6.3.2 we observed that  $\sigma_f$  in the SCCVII tumours discriminated between the rapidly growing SCCVII tumours and the other two models. Further work should include characterizing additional tumour models with varying tumour microenvironments, and also comparison of the oxygen signal decay curves (i.e. when the gas is switched back to room air) as well as the enhancement curves.

Another interesting feature of the ICA extraction process is that for our application, the number of components prescribed rarely matters in separating out the oxygen-responsive component. dOE-MRI maps from ICA applied serially after varying the number of components ( $m$ ) from 3 to 12 are shown in Figure 8.3. The component of the signal that corresponds to the T<sub>1</sub>W signal intensity increase due to the cycling oxygen is quite prominent and independent of the number of components selected. This analysis is presented to ensure that the number of components selected had no bearing on the extracted ICA component. Two examples are shown in Figure 8.3 that were selected to exhibit the variability (low on the left of Figure 8.3 and high on the right) in extracted components in a single experiment.

In both cases, the corresponding dOE-MRI maps show the same O<sub>2</sub>-positive and O<sub>2</sub>-negative regions. Interestingly, in the high variability case, when  $m = 10$ , the ICA algorithm was not able to extract the oxygen-enhancing component. Exploring how the presence or absence of noise affects the extraction process would be useful in further development of the technique. There may be implications worth exploring in how the variability in the extracted component actually provides information about the underlying tumour microenvironment.

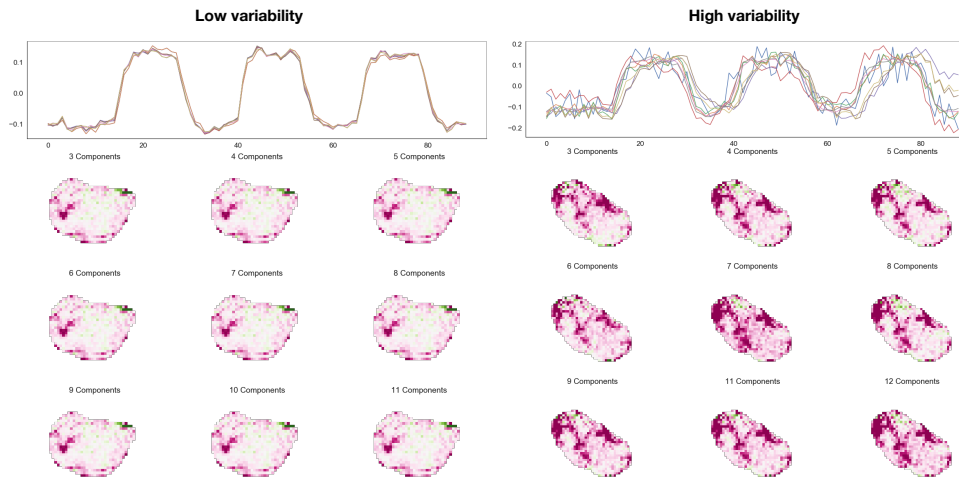


**Figure 8.3:** Two animals were selected to explore the effect of the number of components ( $m$ ) on the dOE-MRI maps. The two animals presented here were selected to exhibit the full range of variability in extracted components. The low variability example shows no discernible difference in the extracted component anywhere from  $m = 3$  to  $m = 12$ . The high variability example shows considerably more noise in the extracted component, but the same overall trend. The corresponding dOE-MRI maps for both the low variability and high variability examples show almost no difference in the oxygenation maps.

## 8.4 dOE-MRI maps of 10 consecutive air/O<sub>2</sub> switches are stable

The presence of hypoxia in tumours is known to exhibit microregional and temporal heterogeneity. The process of cells going through periods of oxygen-

starvation and then subsequently being re-oxygenated has been termed cyclic hypoxia [92, 94, 156]. A leading cause of cycling hypoxia is the variable flux of red blood cells through the abnormal tumour vasculature on time scales of minutes to hours. There is some evidence of cycling hypoxia in our data as there are clear mismatches between pimonidazole staining and perfusion markers (Figure 8.5). The SCCVII tumour model has specifically been shown to be afflicted by cycling hypoxia as early as 1986 [157]. It is therefore not surprising that dOE-MRI is sensitive to these changes in this tumour model, and provides the first non-invasive data suggesting cycling hypoxia on the relatively short timeline of less than 15 minutes. The clinical importance of intermittent hypoxia is unclear largely due to poor availability of techniques to measure it in humans [93]. Recent work on measuring cycling hypoxia in patients using  $R_2^*$  [130] shows that interest in this phenomenon continues.

Despite the presence of cycling hypoxia in many regions of the SCCVII tumours,  $O_2$ -enhancing regions in dOE-MRI maps are generally in agreement with well perfused areas of histology images. In particular, concentrated oxygen-responsive regions within a dOE-MRI map correspond to highly vascular, perfused regions in matching histology images. Voxels anti-correlated with the  $O_2$  stimulus ( $O_2$  refractory, green) typically correspond with pimonidazole staining but there are instances of mismatch (Figures 6.6, 6.7, and 8.5). In addition to cycling hypoxia, there may be possible mismatch between the sensitivities of pimonidazole and dOE-MRI and other oxygen sensing modalities (described in [96]). Success of dOE-MRI will ultimately depend on its validation as a clinically useful measure of tumour hypoxia.

To assess this phenomenon, a pilot study was carried out to determine whether this cycling hypoxia can be measured with dOE-MRI. In a small pilot cohort of SCCVII xenografts mice ( $n = 2$ ), rather than the standard protocol of three cycles of air-oxygen switches, ten consecutive air-oxygen switches were used. ICA was applied to each cycle of the sequences separately (as described in section 5.9). Figure 8.4 shows the results from a tumour including a dOE-MRI map (8.4A), a standard deviation map (8.4B), and a coefficient of variation map (8.4C). The standard deviation and coefficient of variation maps are surrogate measures of cycling hypoxia as they highlight regions of the tumour that show the highest degree of

deviation or variation over the ten cycles. It is expected that if cycling hypoxia exists, these measures would show regions where it is apparent. If cycling hypoxia is not present, then the two parameter maps would be largely feature-less. In this case, there appears to be little evidence for cycling hypoxia as the dOE-MRI maps are fairly consistent from cycle to cycle. Unfortunately, these results remain un-validated because we were not able to assess cycling hypoxia using histology. One way to assess cycling hypoxia using histology is to use two separate hypoxia stains (such as EF5 and pimonidazole) and inject them intravenously 30-60 minutes apart. Imaging the two stains and mapping the differences could confirm the presence or absence of cycling hypoxia. A subsequent experiment where the dOE-MRI analysis is repeated in more animals alongside the dual hypoxia histological markers would help confirm this finding. As suggested by Dr. Jeff Dunn in private communications, another way of exploring cycling hypoxia within a single imaging session is to reduce blood pressure to the tumour. Since the malformed vessel architecture of the tumour are unlikely to have substantial flow regulation, this should reduce blood flow to the tumour and result in an increase of hypoxic regions. Measuring the oxygenation before and after temporary blood pressure reduction should provide us with an acute change in hypoxia that our technique could measure.

## 8.5 Exploring the link between perfusion and oxygenation

One SCCVII and one HCT-116 tumour-bearing mouse were catheterized and injected with 30-mM solution of Gd-DTPA for DCE-MRI at a rate of 1 mL/min using a power injector at a dose of 5  $\mu$ L/g.

Signal intensity timecourse from the DCE-MRI data was first normalized to the mean signal intensity pre-injection. A numerical integration technique that relies on quadratic polynomials to approximate functions (Simpson's Rule, `scipy.integrate.simps`) was used to calculate the area under the first 60 seconds ( $AUC_{60}$ ) of the normalized signal intensity enhancement curve. A binary ground-truth perfusion map was constructed by classifying all voxels with  $AUC_{60} > 0$  as perfused and everything else as unperfused.

Where dOE-MRI and DCE-MRI scans were acquired in the same SCCVII

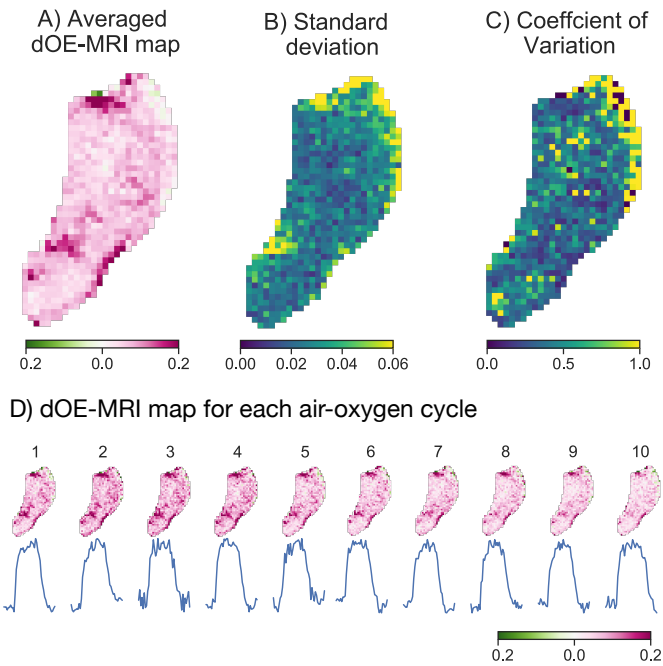


**Figure 8.4:** Results of a dOE-MRI-based analysis to sequentially analyze ten consecutive air-oxygen switches (D). The averaged dOE-MRI map (A) across all 10 cycles reveals some hyperintense regions corresponding to oxygen-responsive areas. The voxel-wise standard deviation (B) and coefficient of variation (C) of the ten dOE-MRI maps shows some variability at the top of the tumour as well as on the mid-right of the tumour.

and HCT-116 tumour-bearing mice, maps of oxygenation status were compared to  $AUC_{60}$  perfusion maps, as shown in Figure 8.5. Mean  $AUC_{60}$  for the well-perfused SCCVII tumour was  $22 \pm 16 \% \cdot s$  and for the comparatively poorly perfused HCT-116 tumour was  $7 \pm 7 \% \cdot s$ . Well-oxygenated  $O_2$ -positive regions generally correspond to perfused, high  $AUC_{60}$  areas in both SCCVII and HCT-116 tumours. A large patch of necrosis, as identified in histological section, in the HCT-116 tumour was also extremely poorly perfused; such large patches of necrosis were not present in the SCCVII tumour.

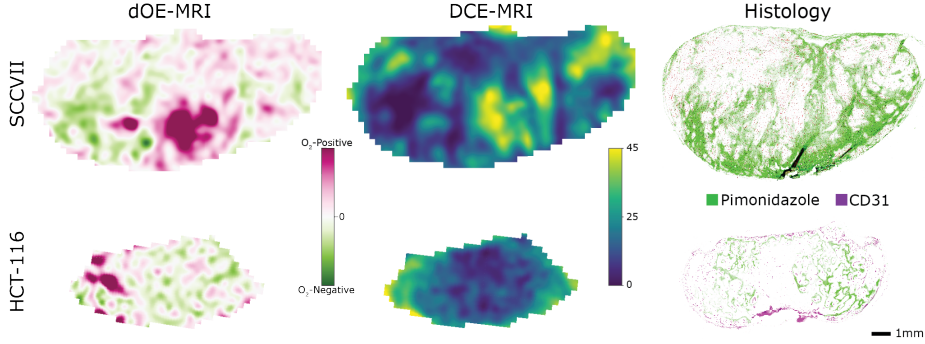


**Figure 8.5:** dOE-MRI maps and DCE-MRI AUC<sub>60</sub>maps and slice-matched histology sections of SCCVII and HCT-116 tumours. Large regions marked as purple in the dOE-MRI maps are O<sub>2</sub>-positive and also correspond to regions that have high AUC<sub>60</sub> values (yellow). Green or O<sub>2</sub>-negative regions from the dOE-MRI map are often consistent with unperfused regions in the AUC<sub>60</sub> (black), but there are regions of mismatch. Histology images stained with pimonidazole (green) and CD31 (purple) are shown for corresponding sections.

## 8.6 Expanding dOE-MRI to include T<sub>2</sub><sup>\*</sup>

For a variety of reasons, the past 5-10 years have seen a gradual resurgence of oxygen-enhanced MRI and renewed interest to refine and better understand the mechanism of action. One important strategy to elucidate the mechanism of oxygen as a contrast agent is to rely on the BOLD effect. In 2002, Dunn et al. modified the inhaled gas in rats with intracranial tumours and used BOLD imaging to assess changes in tumour oxygenation [? ]. More recently, Little et al. have shown that simultaneous acquisition of T<sub>1</sub> and T<sub>2</sub><sup>\*</sup> images improves the specificity of oxygen-enhanced MRI [108]. Here we outline how our technique using ICA can be expanded to include T<sub>2</sub><sup>\*</sup> imaging, and what the additional information will be used for.

T<sub>2</sub><sup>\*</sup> imaging would utilize the Blood Oxygen Level Dependent (BOLD) effect, which can measure shifts in hemoglobin saturation through changes in T<sub>2</sub><sup>\*</sup> and therefore assess tumour perfusion without the need for injectable contrast agents. Applying an oxygen challenge also shifts the haemoglobin saturation and, thus, the T<sub>2</sub><sup>\*</sup> signal. The expected behaviour of a joint change in T<sub>1</sub> and T<sub>2</sub><sup>\*</sup> in response to

a gas challenge, and how this can be interpreted to reflect tumour oxygenation is based on data from recent work by Little [108] and Waterton et al. [158].

The altered  $T_2^*$  provides a robust measure of areas with functioning vasculature. Subsequently, dOE-MRI maps can be masked using the  $\Delta T_2^*$  maps to exclude unperfused regions resulting in a completely endogenous technique to assess tumour oxygenation. OE-MRI  $T_1$ -weighted signal more directly reflects oxygen amounts in plasma and tissues and is more applicable for measuring tumour oxygenation as it relates to radiotherapy. Without sacrificing the information obtained from  $T_1$ -weighted signal intensity in our current work, we propose to extract both  $T_1$ -weighted signal intensity and  $T_2^*$  simultaneously using a dynamic, multi-gradient echo in place of a dynamic FLASH sequence. The cycling gas challenge in combination with ICA improvement to  $T_1$ -weighted oxygen-enhanced imaging will also be applicable to  $T_2^*$ .

A multi-gradient echo (MGE) sequence is ideal to extend our current  $T_1$  based dOE-MRI technique to also acquire dynamic  $T_2^*$  weighted data. This is because initial echoes from an MGE sequence are  $T_1$  weighted and as the echo time increases, the images become more  $T_2^*$  weighted. The  $T_1w$  dOE-MRI map can be calculated from the signal intensity of the first gradient echo image (minimal echo time  $TE \approx 2.25$  ms). The  $T_2^*$  dOE-MRI map can be created by applying ICA to the mono-exponentially fitted multi-gradient echo data at each repetition. Figure 8.6 outlines our approach to obtain  $T_1$ - and  $T_2^*$ -based dOE-MRI maps from a single multi-gradient echo sequence. While the temporal resolution of the multi-gradient echo technique is lower, the data quality of the  $T_1w$  dOE-MRI map is not compromised until subsampling exceeds six times the original temporal resolution when compared to that obtained with a FLASH sequence (see Figure 5.5.6).

### 8.6.1 Independent vector analysis

ICA can be extended if the data being analyzed is multi-dimensional beyond temporal and spatial coordinates, for instance,  $T_1$  and  $T_2^*$  weighted images. Independent vector analysis (IVA) is the technique that permits the increased statistical power of two independent parameters acquired simultaneously. It is a vector-based blind-source estimation first used in fMRI applications [159]. The problem solved

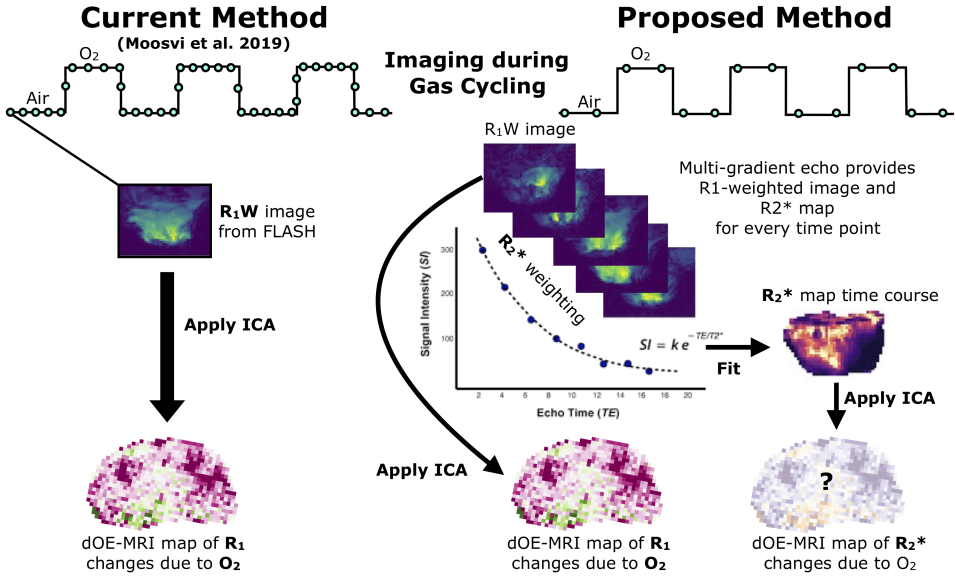


**Figure 8.6:** Schematic of the current and proposed acquisition and analysis for dOE-MRI with combined  $R_1$  and  $R_2^*$  imaging.

by IVA is that observations that are vector quantities (i.e. data consisting of one  $T_1$ -weighted signal and one  $T_2^*$  value derived from the exponential fit) are explained by a mixture of source vectors [159]:

$$x_i = \sum_j^L a_{ij} \circ s_j \quad (8.1)$$

where  $\circ$  indicates an element-wise product. An algorithm suggested by Rafique et al. in 2016 solves the implementation problem and makes it available as FastIVA [160]. It would be worthwhile to explore IVA as an extension to ICA once the  $T_1$  and  $T_2^*$  weighted data is acquired.

## 8.7 Conclusions

In this thesis we have presented two non-invasive imaging-based techniques to probe the tumour microenvironment. In Chapter 2, HPG-GdF, a novel contrast agent was described and its contrast kinetics quantified using two parameters: aPS and fPV. Chapters 3 and 4 discuss applications of the technique we described in

two drugs: trastuzumab and bevacizumab. Though the same contrast agent was used in both applications, the research questions were entirely different and we first tried to determine whether vascular function could explain the limited distribution of trastuzumab in tumours. With bevacizumab, we sought to measure the permeability change of tumour vessels to assess whether treatment normalizes the tumour vasculature. Overall, the utility of HPG-GdF in evaluating the effects of cancer drugs is promising but further work needs to be done to assess its applicability in multiple tumour models.

Motivated by histological data showing a reduction in hypoxia after treatment with bevacizumab, in Chapter 5 we presented the dOE-MRI method which provides significant improvements to the speed, and applicability of existing OE-MRI techniques. Traditional quantitative  $T_1$ -mapping techniques have longer imaging times and are impractical for OE-MRI due to SNR and time constraints. dOE-MRI with ICA is clinically translatable as the sequence acquisition is relatively short and most centres already have access to dynamic  $T_1W$  MRI acquisitions that many patients already routinely receive.

In Chapters 5 and 6, we showed that small changes in  $T_1W$  signal intensity arising from cycling respiratory challenges can be separated robustly using ICA. In Chapter 7 dOE-MRI was used to show that treatment with bevacizumab improved tumour oxygenation, and that the location of tumour implants has a bearing on the vascular network that forms. dOE-MRI is an exciting, non-invasive and widely available technique for assessing tumour oxygenation that could provide a crucial tool in the field of radiation oncology and in the development of treatments targeting the tumour microenvironment. We look forward to the opening of exciting avenues by dOE-MRI in the areas of drug development, patient stratification, and treatment monitoring.

# Bibliography

- [1] Baker JHE, McPhee KC, Moosvi F, Saatchi K, Häfeli UO, Minchinton AI, et al. Multi-modal magnetic resonance imaging and histology of vascular function in xenografts using macromolecular contrast agent hyperbranched polyglycerol (HPG-GdF). *Contrast Media & Molecular Imaging*. 2015 Aug;11(1):77–88. → pages vi, 24, 42, 45, 61, 63
- [2] Baker JHE, Kyle AH, Reinsberg SA, Moosvi F, Patrick HM, Cran J, et al. Heterogeneous distribution of trastuzumab in HER2-positive xenografts and metastases: role of the tumor microenvironment. *Clinical & Experimental Metastasis*. 2018 Sep;19(48):1–15. → pages viii, 48
- [3] Moosvi F, Baker JHE, Yung A, Kozlowski P, Minchinton AI, Reinsberg SA. Fast and sensitive dynamic oxygen-enhanced MRI with a cycling gas challenge and independent component analysis. *Magnetic Resonance in Medicine*. 2018 Oct;. → pages ix, x, 89, 105
- [4] Hanahan D, Weinberg RA. Hallmarks of Cancer: The Next Generation. *Cell*. 2011 Mar;144(5):646–674. → pages xix, 2
- [5] Hanson LG. Is quantum mechanics necessary for understanding magnetic resonance? *Concepts in Magnetic Resonance: Part A*. 2008 Jul;p. 329–340. → pages xix, 8
- [6] Saatchi K, Soema P, Gelder N, Misri R, McPhee K, Baker JHE, et al. Hyperbranched Polyglycerols as Trimodal Imaging Agents: Design, Biocompatibility, and Tumor Uptake. *Bioconjugate Chemistry*. 2012 Feb;23(3):372–381. → pages xx, 18, 20, 21, 26, 43, 53
- [7] Gómez-Cambronero J. The Oxygen Dissociation Curve of Hemoglobin: Bridging the Gap between Biochemistry and Physiology. *Journal of Chemical Education*. 2001 Jun;78(6):757. → pages xxiv, 66, 67

- [8] OpenStax, Gas Exchange across Respiratory Surfaces. OpenStax CNX; 2016. → pages xxv, 68
- [9] Hudson JM, Karshafian R, Burns PN. Quantification of flow using ultrasound and microbubbles: a disruption replenishment model based on physical principles. *Ultrasound in medicine & biology*. 2009 Dec;35(12):2007–2020. → pages xxviii, 90, 91, 100
- [10] Canadian Cancer Statistics 2018; 2018. Available from: <https://cancer.ca/Canadian-Cancer-Statistics-2018-EN>. → page 1
- [11] Biomarkers Definitions Working Group . Biomarkers and surrogate endpoints: preferred definitions and conceptual framework. *Clinical Pharmacology & Therapeutics*. 2001 Mar;69(3):89–95. → page 1
- [12] van der Meel R, Gallagher WM, Oliveira S, O'Connor AE, Schiffelers RM, Byrne AT. Recent advances in molecular imaging biomarkers in cancer: application of bench to bedside technologies. *Drug discovery today*. 2010 Feb;15(3-4):102–114. → page 1
- [13] Hanahan D, Weinberg RA. The hallmarks of cancer. *Cell*. 2000 Jan;100(1):57–70. → page 2
- [14] Folkman J. What is the evidence that tumors are angiogenesis dependent? *Journal of the National Cancer Institute*. 1990 Jan;82(1):4–6. → page 2
- [15] Laking GR, West C, Buckley DL, Matthews J, Price PM. Imaging vascular physiology to monitor cancer treatment. *Critical reviews in oncology/hematology*. 2006 May;58(2):95–113. → pages 3, 5, 6
- [16] McDonald DM, Baluk P. Significance of blood vessel leakiness in cancer. In: *Cancer research*. Comprehensive Cancer Center, Cardiovascular Research Institute, University of California-San Francisco, 513 Parnassus Avenue, San Francisco, CA 94143, USA. dmcd@itsa.ucsf.edu; 2002. p. 5381–5385. → pages 3, 16, 17, 51, 69
- [17] Miles KA, Charnsangavej C, Lee FT, Fishman EK, Horton K, Lee TY. Application of CT in the investigation of angiogenesis in oncology. *Academic radiology*. 2000 Oct;7(10):840–850. → page 4
- [18] Kather JN, Marx A, Reyes-Aldasoro CC, Schad LR, Zöllner FG, Weis CA. Continuous representation of tumor microvessel density and detection of angiogenic hotspots in histological whole-slide images. *Oncotarget*. 2015 Aug;6(22):19163–19176. → page 4

- [19] McDonald DM, Choyke PL. Imaging of angiogenesis: from microscope to clinic. *Nature Medicine*. 2003 Jun;9(6):713–725. → page 5
- [20] Cuenod CA, Fournier L, Balvay D, Guinebretière JM. Tumor angiogenesis: pathophysiology and implications for contrast-enhanced MRI and CT assessment. *Abdominal imaging*. 2006 Mar;31(2):188–193. → page 6
- [21] Hasebroock KM, Serkova NJ. Toxicity of MRI and CT contrast agents. *Expert opinion on drug metabolism & toxicology*. 2009 Apr;5(4):403–416. → page 6
- [22] Levitt MH. Spin Dynamics. *Basics of Nuclear Magnetic Resonance*. John Wiley & Sons; 2001. → pages 6, 7
- [23] O'Connor JPB, Naish JH, Jackson A, Waterton JC, Watson Y, Cheung S, et al. Comparison of normal tissue  $R_1$  and  $R_2^*$  modulation by oxygen and carbogen. *Magnetic Resonance in Medicine*. 2009 Jan;61(1):75–83. → pages 9, 69
- [24] De León-Rodríguez LM, Martins AF, Pinho MC, Rofsky NM, Sherry AD. Basic MR relaxation mechanisms and contrast agent design. *Journal of Magnetic Resonance Imaging*. 2015 Sep;42(3):545–565. → page 12
- [25] Walker-Samuel S, Leach MO, Collins DJ. Evaluation of response to treatment using DCE-MRI: the relationship between initial area under the gadolinium curve (IAUGC) and quantitative pharmacokinetic analysis. *Physics in Medicine and Biology*. 2006 Jul;51(14):3593–3602. → page 13
- [26] Sourbron SP, Buckley DL. On the scope and interpretation of the Tofts models for DCE-MRI. *Magnetic Resonance in Medicine*. 2011 Mar;66(3):735–745. → pages 13, 24, 34
- [27] Sourbron SP, Buckley DL. Classic models for dynamic contrast-enhanced MRI. *NMR in Biomedicine*. 2013 Aug;26(8):1004–1027. → page 13
- [28] Moroz J, Wong CL, Yung AC, Kozlowski P, Reinsberg SA. Rapid measurement of arterial input function in mouse tail from projection phases. *Magnetic Resonance in Medicine*. 2013 Feb;71(1):238–245. → pages 13, 24
- [29] Jain RK. Normalization of tumor vasculature: an emerging concept in antiangiogenic therapy. *Science (New York, NY)*. 2005 Jan;307(5706):58–62. → pages 15, 51, 52, 106

- [30] O'Connor JPB, Jackson A, Parker GJM, Roberts C, Jayson GC. Dynamic contrast-enhanced MRI in clinical trials of antivascular therapies. *Nature Reviews Clinical Oncology*. 2012 Feb;9(3):167–177. → pages 16, 17, 39, 53, 106
- [31] Barrett T, Kobayashi H, Brechbiel M, Choyke PL. Macromolecular MRI contrast agents for imaging tumor angiogenesis. *European Journal of Radiology*. 2006 Dec;60(3):353–366. → pages 17, 61
- [32] Leach MO, Brindle KM, Evelhoch JL, Griffiths JR, Horsman MR, Jackson A, et al. Assessment of antiangiogenic and antivascular therapeutics using MRI: recommendations for appropriate methodology for clinical trials. *The British Journal of Radiology*. 2003;76 Spec No 1:S87–91. → page 16
- [33] De Bruyne S, Van Damme N, Smeets P, Ferdinand L, Ceelen W, Mertens J, et al. Value of DCE-MRI and FDG-PET/CT in the prediction of response to preoperative chemotherapy with bevacizumab for colorectal liver metastases. *British Journal of Cancer*. 2012 May;106(12):1926–1933. → page 17
- [34] Kelly RJ, Rajan A, Force J, Lopez-Chavez A, Keen C, Cao L, et al. Evaluation of KRAS Mutations, Angiogenic Biomarkers, and DCE-MRI in Patients with Advanced Non-Small-Cell Lung Cancer Receiving Sorafenib. *Clinical Cancer Research*. 2011 Mar;17(5):1190–1199.
- [35] Bains LJ, Baker JHE, Kyle AH, Minchinton AI, Reinsberg SA. Detecting Vascular-Targeting Effects of the Hypoxic Cytotoxin Tirapazamine in Tumor Xenografts Using Magnetic Resonance Imaging. *International Journal of Radiation Oncology\*Biology\*Physics*. 2009 Jul;74(3):957–965. → pages 17, 19, 43, 54
- [36] O'Connor JPB, Rose CJ, Jackson A, Watson Y, Cheung S, Maders F, et al. DCE-MRI biomarkers of tumour heterogeneity predict CRC liver metastasis shrinkage following bevacizumab and FOLFOX-6. *British Journal of Cancer*. 2011 Jun;105(1):139–145. → page 17
- [37] Alic L, van Vliet M, van Dijke CF, Eggemont AMM, Veenland JF, Niessen WJ. Heterogeneity in DCE-MRI parametric maps: a biomarker for treatment response? *Physics in Medicine and Biology*. 2011 Mar;56(6):1601–1616. → page 17
- [38] Minchinton AI, Tannock IF. Drug penetration in solid tumours. *Nature Reviews Cancer*. 2006 Aug;6(8):583–592. → pages 17, 35, 40

- [39] Jain RK. Delivery of molecular and cellular medicine to solid tumors. *Advanced Drug Delivery Reviews*. 2001 Mar;46(1-3):149–168. → pages 17, 52
- [40] Iyer AK, Khaled G, Fang J, Maeda H. Exploiting the enhanced permeability and retention effect for tumor targeting. *Drug discovery today*. 2006 Sep;11(17-18):812–818.
- [41] Chauhan VP, Stylianopoulos T, Boucher Y, Jain RK. Delivery of molecular and nanoscale medicine to tumors: transport barriers and strategies. *Annual review of chemical and biomolecular engineering*. 2011;2:281–298. → pages 17, 41, 48, 49
- [42] Weinmann HJ, Brasch RC, Press WR, Wesbey GE. Characteristics of gadolinium-DTPA complex: a potential NMR contrast agent. *AJR American journal of roentgenology*. 1984 Mar;142(3):619–624. → page 17
- [43] Hashizume H, Baluk P, Morikawa S, McLean JW, Thurston G, Roberge S, et al. Openings between defective endothelial cells explain tumor vessel leakiness. *The American journal of pathology*. 2000 Apr;156(4):1363–1380. → page 17
- [44] Tang J, Sheng Y, Hu H, Shen Y. Macromolecular MRI contrast agents: Structures, properties and applications. *Progress in Polymer Science*. 2013 Mar;38(3-4):462–502. → pages 17, 34
- [45] Kobayashi H, Brechbiel MW. Dendrimer-based nanosized MRI contrast agents. *Current pharmaceutical biotechnology*. 2004 Dec;5(6):539–549. → page 17
- [46] Sato N, Kobayashi H, Hiraga A, Saga T, Togashi K, Konishi J, et al. Pharmacokinetics and enhancement patterns of macromolecular MR contrast agents with various sizes of polyamidoamine dendrimer cores. *Magnetic Resonance in Medicine*. 2001 Dec;46(6):1169–1173. → page 17
- [47] Ogan MD, Schmiedl U, Moseley ME, Grodd W, Paajanen H, Brasch RC. Albumin labeled with Gd-DTPA. An intravascular contrast-enhancing agent for magnetic resonance blood pool imaging: preparation and characterization. *Investigative radiology*. 1987 Aug;22(8):665–671. → pages 18, 35
- [48] Turetschek K, Preda A, Novikov V, Brasch RC, Weinmann HJ, Wunderbaldinger P, et al. Tumor microvascular changes in antiangiogenic

- treatment: Assessment by magnetic resonance contrast media of different molecular weights. *Journal of Magnetic Resonance Imaging*. 2004;20(1):138–144. → pages 18, 35, 58
- [49] Kainthan RK, Muliawan EB, Hatzikiriakos SG, Brooks DE. Synthesis, Characterization, and Viscoelastic Properties of High Molecular Weight Hyperbranched Polyglycerols. *Macromolecules*. 2006 Oct;39(22):7708–7717. → pages 18, 20, 43
- [50] Saatchi K, Gelder N, Gershkovich P, Sivak O, Wasan KM, Kainthan RK, et al. Long-circulating non-toxic blood pool imaging agent based on hyperbranched polyglycerols. *International Journal of Pharmaceutics*. 2012 Jan;422(1-2):418–427. → pages 18, 53
- [51] Kainthan RK, Janzen J, Kizhakkedathu JN, Devine DV, Brooks DE. Hydrophobically derivatized hyperbranched polyglycerol as a human serum albumin substitute. *Biomaterials*. 2008 Apr;29(11):1693–1704. → page 18
- [52] Shenoi RA, Lai BFL, Imran ul haq M, Brooks DE, Kizhakkedathu JN. Biodegradable polyglycerols with randomly distributed ketal groups as multi-functional drug delivery systems. *Biomaterials*. 2013 Aug;34(25):6068–6081. → pages 18, 35
- [53] Imran ul haq M, Lai BFL, Chapanian R, Kizhakkedathu JN. Influence of architecture of high molecular weight linear and branched polyglycerols on their biocompatibility and biodistribution. *Biomaterials*. 2012 Dec;33(35):9135–9147. → page 18
- [54] Parker GJ, Barker GJ, Tofts PS. Accurate multislice gradient echo T(1) measurement in the presence of non-ideal RF pulse shape and RF field nonuniformity. *Magnetic Resonance in Medicine*. 2001 May;45(5):838–845. → page 22
- [55] Shewhart WA. *Economic Control of Quality of Manufactured Product*. ASQ Quality Press; 1931. → page 24
- [56] Pathak AP, Artemov D, Ward BD, Jackson DG, Neeman M, Bhujwalla ZM. Characterizing extravascular fluid transport of macromolecules in the tumor interstitium by magnetic resonance imaging. *Cancer Research*. 2005 Feb;65(4):1425–1432. → pages 24, 36
- [57] Daldrup-Link HE, Okuhata Y, Wolfe A, Srivastav S, Øie S, Ferrara N, et al. Decrease in tumor apparent permeability-surface area product to a MRI

macromolecular contrast medium following angiogenesis inhibition with correlations to cytotoxic drug accumulation. *Microcirculation* (New York, NY : 1994). 2004 Jul;11(5):387–396. → pages 25, 58

- [58] Dafni H, Landsman L, Schechter B, Kohen F, Neeman M. MRI and fluorescence microscopy of the acute vascular response to VEGF165: vasodilation, hyper-permeability and lymphatic uptake, followed by rapid inactivation of the growth factor. *NMR in Biomedicine*. 2002;15(2):120–131. → page 25
- [59] Kyle AH, Huxham LA, Yeoman DM, Minchinton AI. Limited tissue penetration of taxanes: a mechanism for resistance in solid tumors. *Clinical Cancer Research*. 2007 May;13(9):2804–2810. → pages 25, 34, 41, 43, 54
- [60] Collins TJ. ImageJ for microscopy. *BioTechniques*. 2007 Jul;43(1 Suppl):25–30. → pages 25, 43, 54, 93
- [61] Baranyai Z, Brücher E, Iványi T, chimica RKH, 2005. Complexation Properties of N, N', N'', N'''-[1, 4, 7, 10-Tetraazacyclododecane-1, 4, 7, 10-tetrayltetrakis (1-oxoethane-2, 1-diyl)] tetrakis [glycine](H4dotagl) .... *Concepts in Magnetic Resonance: Part A*. 2005;: → page 35
- [62] Kawai F. Microbial degradation of polyethers. *Applied Microbiology and Biotechnology*. 2002 Jan;58(1):30–38. → page 35
- [63] Li KL, Wilmes LJ, Henry RG, Pallavicini MG, Park JW, Hu-Lowe DD, et al. Heterogeneity in the angiogenic response of a BT474 human breast cancer to a novel vascular endothelial growth factor-receptor tyrosine kinase inhibitor: Assessment by voxel analysis of dynamic contrast-enhanced MRI. *Journal of Magnetic Resonance Imaging*. 2005 Oct;22(4):511–519. → page 36
- [64] Erickson K, Braun RD, Yu D, Lanzen J, Wilson D, Brizel DM, et al. Effect of longitudinal oxygen gradients on effectiveness of manipulation of tumor oxygenation. *Cancer Research*. 2003 Aug;63(15):4705–4712. → page 38
- [65] Dewhirst MW, Ong ET, Braun RD, Smith B, Klitzman B, Evans SM, et al. Quantification of longitudinal tissue pO<sub>2</sub> gradients in window chamber tumours: impact on tumour hypoxia. *British Journal of Cancer*. 1999 Apr;79(11-12):1717–1722. → page 38
- [66] Seal MD, Speers CH, O'Reilly S, Gelmon KA, Ellard SL, Chia SK. Outcomes of women with early-stage breast cancer receiving adjuvant trastuzumab. *Current Oncology*. 2012 Aug;19(4). → page 40

- [67] Bria E, Cuppone F, Fornier M, Nisticò C, Carlini P, Milella M, et al. Cardiotoxicity and incidence of brain metastases after adjuvant trastuzumab for early breast cancer: the dark side of the moon? A meta-analysis of the randomized trials. *Breast Cancer Research and Treatment*. 2007 Jul;109(2):231–239. → page 40
- [68] Kaplan MA, Ertugrul H, Firat U, Kucukoner M, İnal A, Urakci Z, et al. Brain metastases in HER2-positive metastatic breast cancer patients who received chemotherapy with or without trastuzumab. *Breast Cancer*. 2014 Jan;22(5):503–509. → page 40
- [69] Lai R, Dang CT, Malkin MG, Abrey LE. The risk of central nervous system metastases after trastuzumab therapy in patients with breast carcinoma. *Cancer*. 2004;101(4):810–816. → page 40
- [70] Murrell DH, Hamilton AM, Mallett CL, van Gorkum R, Chambers AF, Foster PJ. Understanding Heterogeneity and Permeability of Brain Metastases in Murine Models of HER2-Positive Breast Cancer Through Magnetic Resonance Imaging: Implications for Detection and Therapy. *Translational Oncology*. 2015 Jun;8(3):176–184. → page 40
- [71] Stemmler HJ, Kahlert S, Siekiera W, Untch M, Heinrich B, Heinemann V. Characteristics of patients with brain metastases receiving trastuzumab for HER2 overexpressing metastatic breast cancer. *Breast (Edinburgh, Scotland)*. 2006 Apr;15(2):219–225. → page 40
- [72] Kyle AH, Baker JHE, Gandolfo MJ, Reinsberg SA, Minchinton AI. Tissue Penetration and Activity of Camptothecins in Solid Tumor Xenografts. *Molecular Cancer Therapeutics*. 2014 Nov;13(11):2727–2737. → page 41
- [73] Huxham LA, Kyle AH, Baker JHE, Nykilchuk LK, Minchinton AI. Microregional effects of gemcitabine in HCT-116 xenografts. *Cancer Research*. 2004 Sep;64(18):6537–6541.
- [74] Kyle AH, Huxham LA, Chiam ASJ, Sim DH, Minchinton AI. Direct assessment of drug penetration into tissue using a novel application of three-dimensional cell culture. *Cancer Research*. 2004 Sep;64(17):6304–6309.
- [75] Kyle AH, Minchinton AI. Measurement of delivery and metabolism of tirapazamine to tumour tissue using the multilayered cell culture model. *Cancer chemotherapy and pharmacology*. 1999;43(3):213–220. → page 41

- [76] Jain RK, Stylianopoulos T. Delivering nanomedicine to solid tumors. *Nature Reviews Clinical Oncology*. 2010 Sep;7(11):653–664. → pages 41, 48, 49
- [77] Juweid M, Neumann R, Paik C, Perez-Bacete MJ, Sato J, van Osdol W, et al. Micropharmacology of monoclonal antibodies in solid tumors: direct experimental evidence for a binding site barrier. *Cancer Research*. 1992 Oct;52(19):5144–5153. → pages 41, 48
- [78] Baker JHE, Lindquist KE, Huxham LA, Kyle AH, Sy JT, Minchinton AI. Direct Visualization of Heterogeneous Extravascular Distribution of Trastuzumab in Human Epidermal Growth Factor Receptor Type 2 Overexpressing Xenografts. *Clinical Cancer Research*. 2008 Apr;14(7):2171–2179. → pages 41, 43, 44, 48
- [79] Lee CM, Tannock IF. The distribution of the therapeutic monoclonal antibodies cetuximab and trastuzumab within solid tumors. *BMC cancer*. 2010 Jun;10(1):255. → pages 41, 48
- [80] Trotter MJ, Chaplin DJ, Olive PL. Use of a carbocyanine dye as a marker of functional vasculature in murine tumours. *British Journal of Cancer*. 1989 May;59(5):706–709. → pages 19, 42
- [81] Thurber GM, Dane Wittrup K. A mechanistic compartmental model for total antibody uptake in tumors. *Journal of theoretical biology*. 2012 Dec;314:57–68. → page 48
- [82] Goel S, Duda DG, Xu L, Munn LL, Boucher Y, Fukumura D, et al. Normalization of the Vasculature for Treatment of Cancer and Other Diseases. *Physiological Reviews*. 2011 Jul;91(3):1071–1121. → page 48
- [83] Viallard C, Larrivée B. Tumor angiogenesis and vascular normalization: alternative therapeutic targets. *Angiogenesis*. 2017 Nov;20(4):409–426. → page 52
- [84] Martin JD, Seano G, Jain RK. Normalizing Function of Tumor Vessels: Progress, Opportunities, and Challenges. *Annual review of physiology*. 2019 Feb;81:505–534. → page 52
- [85] Genentech RG. Avastin (Bevacizumab) [package insert]; 2019. → page 52
- [86] Turetschek K, Floyd E, Shames DM, Roberts TP, Preda A, Novikov V, et al. Assessment of a rapid clearance blood pool MR contrast medium

(P792) for assays of microvascular characteristics in experimental breast tumors with correlations to histopathology. Magnetic Resonance in Medicine. 2001 May;45(5):880–886. → page 58

- [87] de Lussanet QG, Langereis S, Beets-Tan RGH, van Genderen MHP, Griffioen AW, van Engelshoven JMA, et al. Dynamic contrast-enhanced MR imaging kinetic parameters and molecular weight of dendritic contrast agents in tumor angiogenesis in mice. Radiology. 2005 Apr;235(1):65–72. → pages 58, 61
- [88] Padhani AR. Dynamic contrast-enhanced MRI in clinical oncology: current status and future directions. Journal of Magnetic Resonance Imaging. 2002 Oct;16(4):407–422. → page 61
- [89] Gerstner ER, Sorensen AG, Jain RK, Batchelor TT. Advances in neuroimaging techniques for the evaluation of tumor growth, vascular permeability, and angiogenesis in gliomas. Current opinion in neurology. 2008 Dec;21(6):728–735. → page 61
- [90] Tofts PS, Brix G, Buckley DL, Evelhoch JL, Henderson E, Knopp MV, et al. Estimating kinetic parameters from dynamic contrast-enhanced T(1)-weighted MRI of a diffusible tracer: standardized quantities and symbols. Journal of Magnetic Resonance Imaging. 1999 Sep;10(3):223–232. → page 61
- [91] Mak IW, Evaniew N, Ghert M. Lost in translation: animal models and clinical trials in cancer treatment. American journal of translational research. 2014;6(2):114–118. → page 62
- [92] Dewhirst MW. Relationships between cycling hypoxia, HIF-1, angiogenesis and oxidative stress. Radiation Research. 2009 Dec;172(6):653–665. → pages 62, 102, 123
- [93] Michiels C, Tellier C, Feron O. Cycling hypoxia: A key feature of the tumor microenvironment. Biochimica et Biophysica Acta (BBA) - Reviews on Cancer. 2016 Aug;1866(1):76–86. → pages 62, 102, 123
- [94] Bayer C, Shi K, Astner ST, Maftei CA, Vaupel P. Acute Versus Chronic Hypoxia: Why a Simplified Classification is Simply Not Enough. International Journal of Radiation Oncology\*Biology\*Physics. 2011 Jul;80(4):965–968. → pages 62, 102, 123

- [95] Heilmann M, Kiessling F, Enderlin M, Schad LR. Determination of pharmacokinetic parameters in DCE MRI: Consequence of nonlinearity between contrast agent concentration and signal intensity. *Investigative radiology*. 2006 Jun;41(6):536–543. → page 63
- [96] Horsman MR, Mortensen LS, Petersen JB, Busk M, Overgaard J. Imaging hypoxia to improve radiotherapy outcome. *Nature Reviews Clinical Oncology*. 2012 Nov;9(12):674–687. → pages 63, 65, 102, 113, 123
- [97] Wilson WR, Hay MP. Targeting hypoxia in cancer therapy. *Nature Reviews Cancer*. 2011 Jun;11(6):393–410. → page 65
- [98] Rischin D, Hicks RJ, Fisher R, Binns D, Corry J, Porceddu S, et al. Prognostic significance of [18F]-misonidazole positron emission tomography-detected tumor hypoxia in patients with advanced head and neck cancer randomly assigned to chemoradiation with or without tirapazamine: a substudy of Trans-Tasman Radiation Oncology Group Study 98.02. *Journal of Clinical Oncology*. 2006 May;24(13):2098–2104. → page 65
- [99] O'Connor JPB, Boult JKR, Jamin Y, Babur M, Finegan KG, Williams KJ, et al. Oxygen-Enhanced MRI Accurately Identifies, Quantifies, and Maps Tumor Hypoxia in Preclinical Cancer Models. *Cancer Research*. 2016 Feb;76(4):787–795. → pages 67, 68, 69, 70, 101
- [100] Linnik IV, Scott MLJ, Holliday KF, Woodhouse N, Waterton JC, O'Connor JPB, et al. Noninvasive tumor hypoxia measurement using magnetic resonance imaging in murine U87 glioma xenografts and in patients with glioblastoma. *Magnetic Resonance in Medicine*. 2013 Jun;71(5):1854–1862. → pages 67, 69, 87, 101, 103
- [101] Sorg BS, Hardee ME, Agarwal N, Moeller BJ, Dewhirst MW. Spectral imaging facilitates visualization and measurements of unstable and abnormal microvascular oxygen transport in tumors. *Journal of Biomedical Optics*. 2008;13(1):014026. → page 69
- [102] Chiarotti G, Cristiani G, Giulotto L. Proton relaxation in pure liquids and in liquids containing paramagnetic gases in solution. *Il Nuovo Cimento*. 1955 May;1(5):863–873. → page 69
- [103] Young IR, Clarke GJ, Bailes DR, Pennock JM, Doyle FH, Bydder GM. Enhancement of relaxation rate with paramagnetic contrast agents in NMR

imaging. *The Journal of Computed Tomography*. 1981 Dec;5(6):543–547.  
→ page 69

- [104] Jones RA, Ries M, Moonen CTW, Grenier N. Imaging the changes in renal T1 induced by the inhalation of pure oxygen: a feasibility study. *Magnetic Resonance in Medicine*. 2002 Apr;47(4):728–735. → page 69
- [105] Tadamura E, Hatabu H, Li W, Prasad PV, Edelman RR. Effect of oxygen inhalation on relaxation times in various tissues. *Journal of Magnetic Resonance Imaging*. 1997 Jan;7(1):220–225. → page 69
- [106] Berkowitz BA, McDonald C, Ito Y, Tofts PS, Latif Z, Gross J. Measuring the human retinal oxygenation response to a hyperoxic challenge using MRI: eliminating blinking artifacts and demonstrating proof of concept. *Magnetic Resonance in Medicine*. 2001 Aug;46(2):412–416. → page 69
- [107] O'Connor JPB, Naish JH, Parker GJM, Waterton JC, Watson Y, Jayson GC, et al. Preliminary Study of Oxygen-Enhanced Longitudinal Relaxation in MRI: A Potential Novel Biomarker of Oxygenation Changes in Solid Tumors. *International Journal of Radiation Oncology\*Biology\*Physics*. 2009 Nov;75(4):1209–1215. → page 69
- [108] Little RA, Jamin Y, Boult JKR, Naish JH, Watson Y, Cheung S, et al. Mapping Hypoxia in Renal Carcinoma with Oxygen-enhanced MRI: Comparison with Intrinsic Susceptibility MRI and Pathology. *Radiology*. 2018 Sep;288(3):739–747. → pages 69, 101, 126, 127
- [109] Zhao D, Pacheco-Torres J, Hallac RR, White D, Peschke P, Cerdán S, et al. Dynamic oxygen challenge evaluated by NMR T<sub>1</sub> and T<sub>2</sub><sup>\*</sup> - insights into tumor oxygenation. *NMR in Biomedicine*. 2015 Jun;28(8):937–947. → pages 69, 70, 103
- [110] White DA, Zhang Z, Li L, Gerberich J, Stojadinovic S, Peschke P, et al. Developing oxygen-enhanced magnetic resonance imaging as a prognostic biomarker of radiation response. *Cancer Letters*. 2016 Sep;380(1):69–77. → pages 87, 101, 106
- [111] Hallac RR, Zhou H, Pidikiti R, Song K, Stojadinovic S, Zhao D, et al. Correlations of noninvasive BOLD and TOLD MRI with pO<sub>2</sub> and relevance to tumor radiation response. *Magnetic Resonance in Medicine*. 2014 May;71(5):1863–1873. → page 69

- [112] Jordan BF, Magat J, Colliez F, Ozel E, Fruytier AC, Marchand V, et al. Mapping of oxygen by imaging lipids relaxation enhancement: A potential sensitive endogenous MRI contrast to map variations in tissue oxygenation. *Magnetic Resonance in Medicine*. 2012 Sep;70(3):732–744. → page 69
- [113] McGrath DM, Naish JH, O'Connor JPB, Hutchinson CE, Waterton JC, Taylor CJ, et al. Oxygen-induced changes in longitudinal relaxation times in skeletal muscle. *Magnetic Resonance Imaging*. 2008 Feb;26(2):221–227. → page 69
- [114] Kershaw LE, Naish JH, McGrath DM, Waterton JC, Parker GJM. Measurement of arterial plasma oxygenation in dynamic oxygen-enhanced MRI. *Magnetic Resonance in Medicine*. 2010 Dec;64(6):1838–1842. → page 69
- [115] McKeown MJ, Makeig S, Brown GG, Jung TP, Kindermann SS, Bell AJ, et al. Analysis of fMRI data by blind separation into independent spatial components. *Human brain mapping*. 1998;6(3):160–188. → page 71
- [116] Hyvärinen A, Oja E. Independent component analysis: algorithms and applications. *Neural Networks*. 2000 May;13(4-5):411–430. → pages 71, 72, 105
- [117] Pedregosa F, Varoquaux G, Gramfort A, Michel V, Thirion B. Scikit-learn: Machine learning in Python. *Journal of Machine Learning Research*. 2011 Oct;12:2825–2830. → page 72
- [118] Losert C, Peller M, Schneider P, Reiser M. Oxygen-enhanced MRI of the brain. *Magnetic Resonance in Medicine*. 2002 Jul;48(2):271–277. → pages 87, 88
- [119] Calhoun VD, Liu J, Adali T. A review of group ICA for fMRI data and ICA for joint inference of imaging, genetic, and ERP data. *NeuroImage*. 2009 Mar;45(1 Suppl):S163–72. → pages 87, 119
- [120] Greicius MD, Srivastava G, Reiss AL, Menon V. Default-mode network activity distinguishes Alzheimer's disease from healthy aging: evidence from functional MRI. *Proceedings of the National Academy of Sciences of the United States of America*. 2004 Mar;101(13):4637–4642. → page 87
- [121] McKeown MJ, Jung TP, Makeig S, Brown G, Kindermann SS, Lee TW, et al. Spatially independent activity patterns in functional MRI data during the stroop color-naming task. *Proceedings of the National Academy of*

Sciences of the United States of America. 1998 Feb;95(3):803–810. → page 87

- [122] Featherstone AK, O'Connor JPB, Little RA, Watson Y, Cheung S, Babur M, et al. Data-driven mapping of hypoxia-related tumor heterogeneity using DCE-MRI and OE-MRI. *Magnetic Resonance in Medicine*. 2018 Apr;79(4):2236–2245. → page 87
- [123] Qian H, Bassingthwaigte JB. A class of flow bifurcation models with lognormal distribution and fractal dispersion. *Journal of theoretical biology*. 2000 Jul;205(2):261–268. → page 89
- [124] Kalra J, Baker J. Multiplex Immunohistochemistry for Mapping the Tumor Microenvironment. *Methods in molecular biology* (Clifton, NJ). 2017;1554(1):237–251. → page 92
- [125] Newville M, Otten R, Nelson A, Ingargiola A, Stensitzki T, Allan D, et al. lm6t/lm6t-py 0.9.13. Zenodo. 2019 Jun;. → page 93
- [126] Khurana D, Martin EA, Kasperbauer JL, O'Malley BW, Salomao DR, Chen L, et al. Characterization of a spontaneously arising murine squamous cell carcinoma (SCC VII) as a prerequisite for head and neck cancer immunotherapy. *Head & neck*. 2001 Oct;23(10):899–906. → page 100
- [127] Horsman MR, Overgaard J. The impact of hypoxia and its modification of the outcome of radiotherapy. *Journal of radiation research*. 2016 Aug;57 Suppl 1:i90–i98. → page 100
- [128] Burrell JS, Walker-Samuel S, Baker LCJ, Boult JKR, Jamin Y, Halliday J, et al. Exploring  $\Delta R_{2*}$  and  $\Delta R_1$  as imaging biomarkers of tumor oxygenation. *Journal of Magnetic Resonance Imaging*. 2013 Jan;38(2):429–434. → pages 101, 103
- [129] Yang DM, Campbell III JW, Gerberich JL, Zhou H, Mason RP. Assessing Tumor Hypoxia Based on Hypoxic Gas Breathing. In: Proceedings of the 26th Annual Meeting of ISMRM. (632), Paris; 2018. p. 1–3. → page 101
- [130] Panek R, Welsh L, Baker LCJ, Schmidt MA, Wong KH, Riddell AM, et al. Noninvasive Imaging of Cycling Hypoxia in Head and Neck Cancer Using Intrinsic Susceptibility MRI. *Clinical Cancer Research*. 2017 Aug;23(15):4233–4241. → pages 102, 123

- [131] Gross MW, Karbach U, Groebe K, Franko AJ, Mueller-Klieser W. Calibration of misonidazole labeling by simultaneous measurement of oxygen tension and labeling density in multicellular spheroids. *International Journal of Cancer*. 1995 May;61(4):567–573. → page 103
- [132] Remmeli S, Sprinkart AM, Müller A, Träber F, von Lehe M, Gieseke J, et al. Dynamic and simultaneous MR measurement of  $R_1$  and  $R_2^*$  changes during respiratory challenges for the assessment of blood and tissue oxygenation. *Magnetic Resonance in Medicine*. 2012 Aug;70(1):136–146. → page 103
- [133] Silvennoinen MJ, Kettunen MI, Kauppinen RA. Effects of hematocrit and oxygen saturation level on blood spin-lattice relaxation. *Magnetic Resonance in Medicine*. 2003 Feb;49(3):568–571. → page 103
- [134] Ferrara N, Hillan KJ, Gerber HP, Novotny W. Discovery and development of bevacizumab, an anti-VEGF antibody for treating cancer. *Nature reviews Drug discovery*. 2004 May;3(5):391–400. → page 106
- [135] Keating GM. Bevacizumab: a review of its use in advanced cancer. *Drugs*. 2014 Oct;74(16):1891–1925. → pages 106, 107
- [136] Pavlidis ET, Pavlidis TE. Role of bevacizumab in colorectal cancer growth and its adverse effects: a review. *World journal of gastroenterology*. 2013 Aug;19(31):5051–5060.
- [137] Barnett JC, Alvarez Secord A, Cohn DE, Leath CA, Myers ER, Havrilesky LJ. Cost effectiveness of alternative strategies for incorporating bevacizumab into the primary treatment of ovarian cancer. *Cancer*. 2013 Oct;119(20):3653–3661. → page 107
- [138] Kümler I, Christiansen OG, Nielsen DL. A systematic review of bevacizumab efficacy in breast cancer. *Cancer treatment reviews*. 2014 Sep;40(8):960–973. → page 106
- [139] Wang H, Hristov D, Qin J, Tian L, Willmann JK. Three-dimensional Dynamic Contrast-enhanced US Imaging for Early Antiangiogenic Treatment Assessment in a Mouse Colon Cancer Model. *Radiology*. 2015 Nov;277(2):424–434. → page 106
- [140] O'Connor JPB, Carano RAD, Clamp AR, Ross J, Ho CCK, Jackson A, et al. Quantifying antivascular effects of monoclonal antibodies to vascular endothelial growth factor: insights from imaging. *Clinical Cancer Research*. 2009 Nov;15(21):6674–6682. → page 106

- [141] Nagengast WB, de Vries EG, Hospers GA, Mulder NH, de Jong JR, Hollema H, et al. In vivo VEGF imaging with radiolabeled bevacizumab in a human ovarian tumor xenograft. *Journal of Nuclear Medicine*. 2007 Aug;48(8):1313–1319. → page 106
- [142] Yang J, Liao C, Liu Y, Yang G, Ke T, Ding Y, et al. MR imaging biomarkers evaluating vascular normalization window after anti-vessel treatment. *Oncotarget*. 2018 Feb;9(15):11964–11976. → page 106
- [143] Colliez F, Gallez B, Jordan BF. Assessing Tumor Oxygenation for Predicting Outcome in Radiation Oncology: A Review of Studies Correlating Tumor Hypoxic Status and Outcome in the Preclinical and Clinical Settings. *Frontiers in Oncology*. 2017 Jan;7(312):638. → page 113
- [144] Baumann M, Krause M, Overgaard J, Debus J, Bentzen SM, Daartz J, et al. Radiation oncology in the era of precision medicine. *Nature Reviews Cancer*. 2016 Mar;16(4):234–249. → page 113
- [145] Kaanders JHAM, Wijffels KIEM, Marres HAM, Ljungkvist ASE, Pop LAM, van den Hoogen FJA, et al. Pimonidazole binding and tumor vascularity predict for treatment outcome in head and neck cancer. *Cancer Research*. 2002 Dec;62(23):7066–7074. → page 115
- [146] Matsumoto S, Batra S, Saito K, Yasui H, Choudhuri R, Gadisetti C, et al. Antiangiogenic agent sunitinib transiently increases tumor oxygenation and suppresses cycling hypoxia. *Cancer Research*. 2011 Oct;71(20):6350–6359. → page 115
- [147] Lemasson B, Christen T, Serduc R, Maisin C, Bouchet A, Le Duc G, et al. Evaluation of the relationship between MR estimates of blood oxygen saturation and hypoxia: effect of an antiangiogenic treatment on a gliosarcoma model. *Radiology*. 2012 Dec;265(3):743–752. → page 115
- [148] Jain RK. Normalizing Tumor Microenvironment to Treat Cancer: Bench to Bedside to Biomarkers. *Journal of Clinical Oncology*. 2013 Jun;31(17):2205–2218. → page 115
- [149] Chauhan VP, Stylianopoulos T, Martin JD, Popović Z, Chen O, Kamoun WS, et al. Normalization of tumour blood vessels improves the delivery of nanomedicines in a size-dependent manner. *Nature Nanotechnology*. 2012 Apr;7(6):383–388.

- [150] Huang Y, Yuan J, Righi E, Kamoun WS, Ancukiewicz M, Nezivar J, et al. Vascular normalizing doses of antiangiogenic treatment reprogram the immunosuppressive tumor microenvironment and enhance immunotherapy. *Proceedings of the National Academy of Sciences of the United States of America*. 2012 Oct;109(43):17561–17566. → page 115
- [151] Arjona AA, Alvarez E. Tumor site implantation and animal model selection in oncology. vol. 835 of *Cancer Drug Discovery and Development*. Totowa, NJ: Humana Press; 2006. → page 116
- [152] Hubbard WC, Hough AJ, Johnson RM, Oates JA. The site of VX2 tumor transplantation affects the development of hypercalcemia in rabbits. *Prostaglandins*. 1980 Jun;19(6). → page 116
- [153] Malavé I, Blanca I, Fuji H. Influence of inoculation site on development of the Lewis lung carcinoma and suppressor cell activity in syngeneic mice. *Journal of the National Cancer Institute*. 1979 Jan;62(1):83–88. → page 116
- [154] Hill SA, Denekamp J. Site dependent response of tumours to combined heat and radiation. *The British Journal of Radiology*. 1982 Dec;55(660):905–912. → page 116
- [155] Calhoun VD, Adali T, Pearson GD, Pekar JJ. A method for making group inferences from functional MRI data using independent component analysis. *Human brain mapping*. 2001 Nov;14(3):140–151. → page 119
- [156] Bayer C, Vaupel P. Acute versus chronic hypoxia in tumors: Controversial data concerning time frames and biological consequences. *Strahlentherapie und Onkologie : Organ der Deutschen Rontgengesellschaft [et al.]*. 2012 Jul;188(7):616–627. → page 123
- [157] Chaplin DJ, Durand RE, Olive PL. Acute hypoxia in tumors: implications for modifiers of radiation effects. *International journal of radiation oncology, biology, physics*. 1986 Aug;12(8):1279–1282. → page 123
- [158] O'Connor JPB, Robinson SP, Waterton JC. Imaging tumour hypoxia with oxygen-enhanced MRI and BOLD MRI. *The British Journal of Radiology*. 2019 Mar;92(1095):20180642. → page 127
- [159] Lee JH, Lee TW, Jolesz FA, Yoo SS. Independent vector analysis (IVA): multivariate approach for fMRI group study. *NeuroImage*. 2008 Mar;40(1):86–109. → pages 127, 128

- [160] Rafique W, Naqvi SM, Chambers JA. Mixed source prior for the fast independent vector analysis algorithm. In: IEEE Sensor Array and Multichannel Signal Processing Workshop SAM. IEEE; 2016. p. 1–5. → page 128